Title
Correlated Topological Materials

Author
Ivanov, Vsevolod

Publication Date
2021

Peer reviewed|Thesis/dissertation

Correlated Topological Materials

By

VSEVOLOD IVANOV

DISSERTATION

Submitted in partial satisfaction of the requirements for the degree of

DOCTOR OF PHILOSOPHY

in

Condensed Matter Physics

in the

OFFICE OF GRADUATE STUDIES

of the

UNIVERSITY OF CALIFORNIA,

DAVIS

Approved:

Professor Sergey Savrasov, Chair

Professor Rajiv R. P. Singh

Professor Richard Scalettar

Committee in Charge

2021

TABLE OF CONTENTS

LIST OF FIGURES

LIST OF TABLES

ACKNOWLEDGMENTS

I would like to thank my advisor Prof. Sergey Savrasov for providing wisdom and guidance throughout my PhD work, and pushing me to be fastidious and independent, which has helped me gain confidence in my research. I am also grateful for the support and collaboration of Prof. Xiangang Wan, Filip Ronning, and Tomoya Asaba, with whom much of the work in this dissertation was done.

Finally, I am thankful for my loving family: my parents and my two brothers, who supported me throughout my graduate studies.

I acknowledge funding support from NSF DMR Grants No. 1411336 and No. 1832728.

WORKS PUBLISHED

Parts of this dissertation are based on the published works listed below.

1. **Ivanov V** and Savrasov SY (2019) *Monopole mining method for high-throughput screening for Weyl semimetals*, Physical Review B, 99, 125124 [arxiv:1810.09402].
2. **Ivanov V**, Wan X, and Savrasov SY (2019) *Topological Insulator-to-Weyl Semimetal Transition in Strongly Correlated Actinide System UNiSn*, Physical Review X, 9, 041055 [arxiv:1809.09543].
3. **Ivanov V**, Wan X, Savrasov SY (2020) *Renormalized quasiparticles, topological monopoles, and superconducting line nodes in heavy-fermion $CeTX_3$ compounds*, Physical Review B Letters 103, L041112 [arxiv:2005.09129].
4. Asaba T, **Ivanov V**, Thomas SM, Savrasov SY, Thompson JD, Bauer ED, Ronning F (2021) *Colossal anomalous Nernst effect in a correlated noncentrosymmetric kagome ferromagnet*, Science Advances 7 [arxiv:2104.09060].
5. Wan X, **Ivanov V**, Resta G, Leonov I, Savrasov SY (2021) *Exchange interactions and sensitivity of the Ni two-hole spin state to Hund's coupling in doped $NdNiO_2$*, Physical Review B 103, 075123 [arxiv:2008.07465].

Some of the results were also presented in talks at the conferences listed below.

1. **APS March Meeting 2019** Correlation Driven Topological Insulator to Weyl Semimetal Transition in Actinide System UNiSn
2. **APS March Meeting 2019** A Monopole Mining Method for High Throughput Screening Weyl Semimetals
3. **APS March Meeting 2020** Correlation-driven renormalization of Weyl nodes in the Ce-113 series
4. **APS March Meeting 2021** Exchange Interactions and Competing S=0 and S=1 States in Doped $NdNiO_2$

Other graduate work not included in this thesis is listed below.

- Najafi E, **Ivanov V**, Zewail A, and Bernardi M (2017) *Super-Diffusion of Excited Carriers in Semiconductors*, Nature Communications, 8, 15177.
- Zhao L, Torchinsky DH, Chu H, **Ivanov V**, Lifshitz R, Flint R, Qi T, Cao G, and Hsieh D (2016) *Evidence of an odd-parity hidden order in a spin–orbit coupled correlated iridate*, Nature Physics, 12, 32 [arxiv:1601.01688].

ABSTRACT

Correlated Topological Materials

By

VSEVOLOD IVANOV

Doctor of Philosophy in Condensed Matter Physics

University of California, Davis, 2021

Professor Sergey Savrasov, Chair

In recent years, the number of materials known to host symmetry–protected topological phases has grown dramatically. Although they were once considered exotic, it is now known that these kinds of sytems are relatively common, and methods have been developed to automatically discover and confirm these phases in non-interacting materials. Nevertheless, the interplay of strong correlations and topology remains largely unexplored, and it is expected that this regime hosts a plethora of exotic phases which are not adiabatically connected to those known for non-interacting systems.

This dissertation focuses on a number of specific examples in this regime exploring the effect of topology in the context of heavy–fermion physics, metal–insulator transitions, and superconductivity. For the class of cerium–based heavy–fermion superconductors, the topological nodal lines in the normal state are used to explain the pairing symmetry of the superconducting state. In UNiSn, an inverted metal–insulator transition is shown to be a Weyl metal–topological insulator transition. The anomalous transport properties that arise in topological semimetals are also discussed in the context of $UCo_{0.8}Ru_{0.2}Al$, in which a collosal Nernst coefficient was recently measured. Finally, calculated exchange interactions for the recently discovered superconductor $Nd_{0.8}Sr_{0.2}NiO_2$ are discussed and compared to the isostructural cuprate superconductors.

Chapter 1

Introduction

The theoretical prediction and subsequent experimental verification of topological insulators, set off a chain of similar predictions and discoveries of numerous other symmetry-protected topological phases, Dirac, Weyl, and nodal line semimetals. These materials possess exotic surface states and quantized transport properties, a peculiarity which allowed them to be naturally characterized and classified based on the topological invariants leading to this quantization. There are various proposed applications for these macroscopic quantum properties, in areas such as spintronics, quantum computing, and thermoelectric devices.

Initially it was thought that such materials were extremely rare, as searches for new topological materials could only be guided by general symmetry principles. Because of this, discoveries of new topological materials were largely serendipitous, and often led to high profile publications. At time of writing, improved numerical methods for identifying topological phases in real materials and concerted efforts involving high-throughput searches of materials databases, have clarified this issue in several ways. Firstly, it has become apparent that topological phases are quite abundant, with over one fourth of known materials displaying some kind of topological phase. Secondly, a large number of high quality topological mate-

rials has been identified; topological insulators with large band gaps as well as semimetals with the minimal number of topological features and no trivial states exactly at the Fermi energy. Such materials make ideal platforms for the experimental verification of predicted phenomena, and designing devices for specific applications. Finally, any new material can be quickly and easily checked for topological features, essentially solving this problem entirely, at least when such a material is well-described by single-electron computational methods.

New symmetry-protected topological phases are still being discovered, involving increasingly more exotic symmetry constraints, or generalizations and combinations of known topological features. However, an important general question remains: what happens to these topological features in the presence of electronic correlations?

This is an incredibly broad problem, and carries with it all of the difficulties that stem from many-body physics. The most elementary interpretation is to consider how introducing strong electronic correlations will impact an existing topological phase. This can be extended further to considerations of correlated topological phases that can emerge when interactions are introduced to a topological system, or an even more exotic scenario, where a topological order can emerge purely as a result of correlations within a many-body system. An alternative way to consider this problem is to examine how the properties of topological features can enhance our understanding of known strongly–correlated effects such as superconductivity, heavy-fermion behavior, and metal-insulator transitions. This dissertation will consider several of these cases, using examples of real materials where both correlations and topological phases compete or coexist.

The dissertation is organized as follows. Chapter 2 will provide a general introduction to symmetry-protected topological phases, focusing specifically on topological insulators and Weyl semimetals. Specific models for these topological phases will be presented, along with a discussion of their requisite symmetries, associated topological invariants, and surface states.

Chapter 3 will introduce some of the numerical methods that are used to identify topological phases in real materials, where there is a critical limitation of finite k–grid size. These methods will then be applied to three specific material examples. Firstly, they will be used to identify Weyl points, triple points, and nodal lines in a class of materials with the inversion–broken ZrNiAl–type structure. Secondly, they will be used to analyze the properties of a class of inversion–broken heavy–fermion superconductors, and the relevance of the topological features to the unconventional superconductivity in these materials will be discussed. Finally, they will be applied to the strongly correlated material UNiSn which displays an inverted metal–insulator transition. Here the computational methods will reveal that this metal–insulator transition is in fact a Weyl metal–topological insulator transition.

In Chapter 4, the unusual transport properties of topological materials will be discussed. Specifically, expressions for the intrinsic anomalous Hall effect and intrinsic anomalous Nernst effect will be derived for a magnetic material hosting Weyl points. A model of tilted Weyl points will be presented to demonstrate how for a certain tilt, the transport properties will be significantly enhanced. This model is used to explain the recent observation of a colossal anomalous Nernst response in $UCo_{0.8}Ru_{0.2}Al$.

Chapter 5 will focus on the magnetic exchange interactions in doped $NdNiO_2$ which was recently shown to superconduct at 15K. This material has a structure and electronic properties similar to those of the cuprate high-temperature superconductors. Numerical simulations will reveal that the physics of this material can be described by a minimal two–band model, which is used to explain the development of magnetic moments upon doping and the underlying Mott insulating state.

Chapter 2

Symmetry-Protected Topological Phases

The Landau theory of symmetry breaking has been a paradigm for understanding phase transitions in condensed matter systems for nearly a century. More recently, a variety of phases have been discovered that cannot be described by local order parameters within the framework of Landau theory, but can instead be associated with some topological invariant. In such systems the topology manifests in the following way: physical observables such as the Hall conductance are inherently quantized, and their values are unaffected by perturbations or disorder, unless these changes to the system are strong enough to induce a quantum phase transition.

This concept of topological order applies to correlated many-electron states, where the topological invariants and associated quantization emerges from a long-range collective behavior of the system. However, similar topological considerations can also be applied to simpler systems which can be adequately described within a single electron band theory. In this case, the states in these systems are called symmetry-protected topological phases

which require certain symmetries to exist, and possess an associated topological invariant. In recent years numerous phases have been discovered, including topological insulators, Weyl semimetals, nodal line semimetals, and triple points.

This chapter will introduce the concepts of symmetry-protected topological states, going into more detail for the specific cases of topological insulators and Weyl semimetals. The specific symmetries required for these phases will be discussed, as well as the topological invariants with which they are associated.

2.1 Topological Insulators

The observation of a quantized integer quantum Hall quickly led to the discovery of unusual insulating states with a gapped electronic structure that could not be continuously deformed into a standard band-insulator without passing through a gapless phase[1]. This way of classifying distinct insulating states was later reformulated within the framework of Chern–Simons theory [2], showing that distinct classes of insulators could be associated with a topological invariant. Furthermore, it was understood that these Chern insulators also possessed distinctive surface states which directly corresponded to their bulk topological property[3, 4]. As the classification expanded to include two [5, 6] and three dimensional [7] topological insulators, the paradigms of topological invariants and bulk-boundary correspondence continued to yield important insights into the physics of these unusual phases.

2.1.1 Chern insulators

When electrons in two dimensions are subject to a magnetic field, their energy levels become quantized Landau levels, with energy $\epsilon = \hbar\omega_C(n_L - 1/2)$, where $\omega_C = eB/m$ is the cyclotron frequency. If an additional electric field is introduced, these Landau levels become

tilted and cause the electrons to drift, resulting in a quantized conductivity $\sigma_{xy} = ne^2/h$, where n is the integer denoting the number of filled Landau levels. In fact, since there is a gap $\hbar\omega_C \propto B$ between each Landau level, in the case of completely filled Landau levels the bulk is completely insulating, so the current is carried entirely by the edge states. These boundary states can be imagined as cyclotron orbits at the edge of the system, where the electrons on the orbit hit the edge and reflect, skipping along the edge of the sample.

Since these edge states propagate in one direction around the sample, they are termed "chiral", and are therefore dissipationless, because there is no opposite state available to scatter into. Hence the quantization of conductivity is just the physical manifestation of this property; the number of chiral edge states that will cross the Fermi energy and connect the valence and conduction bands is exactly the quantization parameter n.

A seminal paper by Thouless, Kohmoto, Nightingale and den Nijs [2], established how this quantization is explicitly connected to topology. They demonstrated a classification scheme for insulators, whereby any gapped Bloch Hamiltonians that could be connected together by smooth deformations without closing the gap would be considered to be in an equivalent class. They defined a Chern invariant in terms of the Berry curvature $\boldsymbol{\Omega}_m(\boldsymbol{k}) = \boldsymbol{\nabla}_{\boldsymbol{k}} \times \langle u_m(\boldsymbol{k})|i\boldsymbol{\nabla}_{\boldsymbol{k}}|u_m(\boldsymbol{k})\rangle$ of the Bloch wavefunctions[8, 9] $|u_m(\boldsymbol{k})\rangle$ of this Hamiltonian

$$n_m = \frac{1}{2\pi}\int d\boldsymbol{k}\Omega_m^z(\boldsymbol{k}) \tag{2.1}$$

which when summed over all occupied bands $n = \sum_m n_m$, was shown to be equivalent to the quantization parameter n.

These two characteristics of Chern insulators can be demonstrated using a two-dimensional lattice model for a Chern insulator $H(\boldsymbol{k}) = \sum_{\boldsymbol{k}} c_{\boldsymbol{k}}^\dagger \tilde{H}(\boldsymbol{k}) c_{\boldsymbol{k}}$[3, 10], where

$$\tilde{H}(\boldsymbol{k}) = \sin(k_x)\sigma_x + \sin(k_y)\sigma_y + (m + \cos(k_x) + \cos(k_y))\,\sigma_z. \tag{2.2}$$

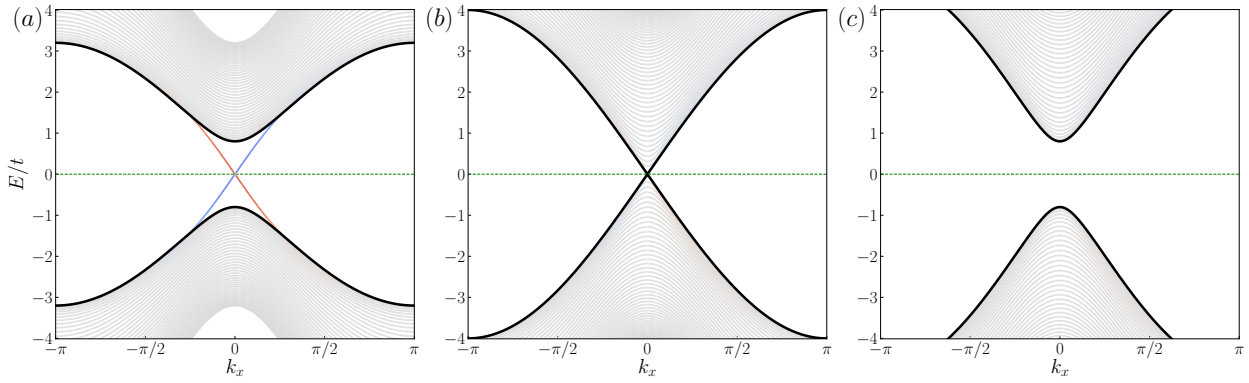

Figure 2.1: Plot of the energy bands along the k_x direction for the model in Eq. 2.2 solved for a slab that is infinite in the x-direction, but finite in the y-direction. The red(blue) state crossing the Fermi energy is chiral edge states on the top(bottom) surface. The three plots correspond to (a) the topological Chern insulator phase, (c) the normal insulator phase, and (b) the semimetalic gapless phase connecting the two.

The mass $m\sigma_z$ controls the breaking of time–reversal symmetry in this model. For $m < -2$, the model yields a trivial insulator. As the mass is increased, the gap closes for $m = -2$, and reopens again in the Chern insulator state $-2 < m < 0$ (Figure 2.1). Thus the trivial and topological phases are separated by a guaranteed gapless phase, which prevents them from being connected through continuous deformation.

Furthermore, the topological property of the Chern insulator can be directly visualized by evaluating this model on a slab geometry which truncates the periodic boundary conditions along the y-direction. This reveals a pair of chiral edge states with linear dispersion $\epsilon \sim \pm\nu_F k_x$, which cross the Fermi energy to connect the valence and conduction bands. Here, the slope ν_F is the Fermi velocity. These chiral states correspond to edge currents in real space, which propagate in opposite directions on top and bottom surface of the slab.

2.1.2 2D and 3D topological insulators

Hall conductivity is odd under time reversal symmetry, and can only exist in a system where time reversal symmetry is broken such as with a magnetic field in the Chern insulator

described above [8, 11]. When spin-orbit coupling is introduced, a different kind of topological phase can emerge. This can be demonstrated using a quantum spin Hall model originally proposed to study HgTe quantum wells [12, 7]

$$H = \sum_{i,\sigma,\alpha} \epsilon_\alpha c^\dagger_{i\alpha\sigma} c_{i\alpha\sigma} - \sum_{ia\sigma\alpha\beta} t_{a\sigma,\alpha\beta} c^\dagger_{i+a\alpha\sigma} c_{i\beta\sigma}, \tag{2.3}$$

where a labels the four nearest–neighbor sites on the square lattice, while $\sigma = \pm$ and $\alpha, \beta = s, p$ are the spin and orbital indices respectively. The orbital indices s, p label the Hg-$6s$ valence and Te-$5p$ conduction orbitals that can invert in the real material under various strain or doping conditions. The hopping matrix in the second term can be written

$$t_{a\sigma} = \begin{pmatrix} t_{ss} & t_{sp} e^{+i\sigma\theta_a} \\ t_{sp} e^{-i\sigma\theta_a} & -t_{pp} \end{pmatrix} \tag{2.4}$$

where θ_a is the angle between the nearest-neighbor bond and the x-axis. Here we take $t = 5t_{sp} = t_{ss} = t_{pp}$ as the energy scale. When $\epsilon_s - \epsilon_p > 4(t_{ss} + t_{pp})$, the system is in a normal insulating state. For $\epsilon_s - \epsilon_p < 4(t_{ss} + t_{pp})$, the opposite parity bands become inverted around $\boldsymbol{k} = 0$, resulting in a two-dimensional topological insulator state[7].

This model can be solved for a strip geometry by constructing a finite supercell in the y-direction and forbidding hoppings between opposite edges. The band structure for this model is plotted in Fig. 2.2, with probability contributions from the edge states indicated with red and blue color. Furthermore, a small term is added to break the Kramers degeneracy and split the spin bands, allowing the individual surface states to be seen. Two pairs of states can be seen crossing the Fermi energy, corresponding to spin currents propagating in opposite directions at the edge of the sample.

Each spin filtered edge state carries one half of the current of the usual quantum Hall edge state. These edge states propagate in opposite directions, so the net Hall conductivity

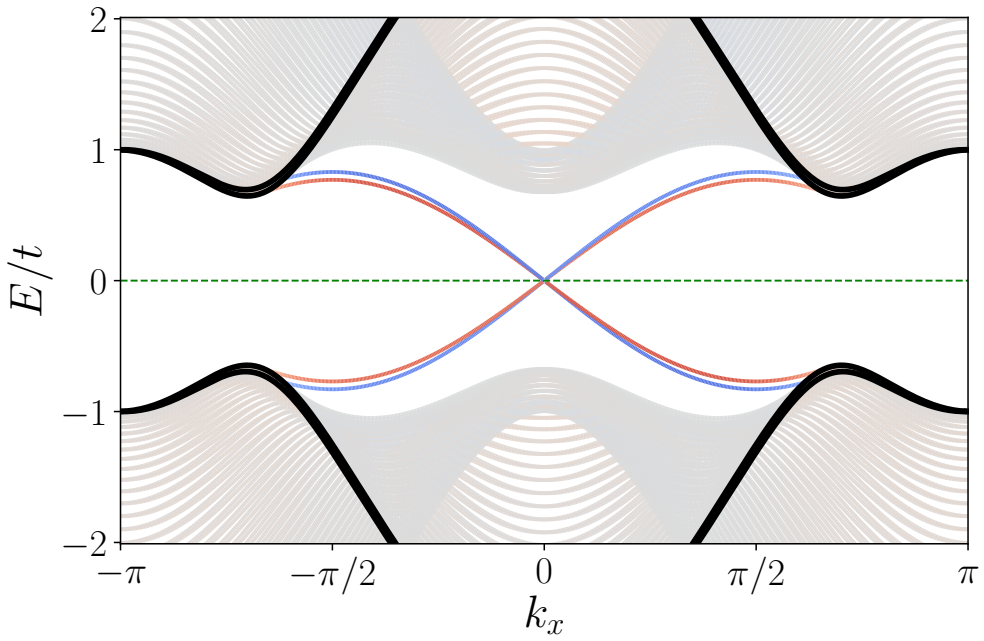

Figure 2.2: The energy bands within the topological phase plotted along the k_x direction. The model in Eq. 2.3 is solved for a slab geometry that is infinite in the x-direction, but finite in the y-direction. Spin filtered edge states cross the Fermi energy, which are separated by adding a small symmetry breaking term. Red (blue) designates states on the upper(lower) surface, with each pair of red/blue bands corresponding to a pair of opposing spin currents propagating in opposite directions on each surface.

vanishes. However, applying an electric field will generate a spin current $J_x^{\uparrow} - J_x^{\downarrow} = \sigma_{xy}^s E_y$ characterized by a quantum spin Hall conductivity $\sigma_{xy}^s = e/2\pi$. In fact, analogously to the Chern insulator, we can define Chern integers $n_{\uparrow}$, $n_{\downarrow}$ for the counter–propagating spin states, which due to $\mathcal{T}$–symmetry must satisfy $n_{\uparrow} + n_{\downarrow} = 0$. Their difference $n_{\sigma} = (n_{\uparrow} - n_{\downarrow})/2$[13] can be used to define a $\mathbb{Z}_2$ topological invariant[5, 6]

$$\nu = n_{\sigma} \text{mod } 2 \tag{2.5}$$

which distinguishes the normal insulator (NI, $\nu = 0$) and topological insulator (TI, $\nu = 1$) states.

It should be noted however, that this definition of the $\mathbb{Z}_2$ topological invariant is only valid in a system which commutes with σ_z. A more general expression can be defined using

the time reversal operator $\Theta = \exp(i\pi\sigma_y/\hbar)K$, where K is the complex conjugation operator and σ_y is the Pauli matrix acting within the spin subspace. One can define a unitary matrix $\omega_{mn}(\boldsymbol{k}) = \langle u_m(\boldsymbol{k})|\Theta|u_n(-\boldsymbol{k})\rangle$ [4]. In the 2D Brillouin zone there are four special time–reversal invariant points $\Gamma_{i=n_1n_2} = (n_1\boldsymbol{b}_1 + n_2\boldsymbol{b}_2)/2, (n_j = 0, 1)$, at which $\boldsymbol{k} = -\boldsymbol{k}$ and $\omega_{mn}(\boldsymbol{k})$ is antisymmetric. The $\mathbb{Z}_2$ topological invariant is defined as a product over these points

$$(-1)^{\nu} = \prod_{i=1}^{4} \delta_i = \prod_{i=1}^{4} \frac{\sqrt{\mathrm{Det}[\omega(\Gamma_i)]}}{\mathrm{Pf}[\omega(\Gamma_i)]} \tag{2.6}$$

where, using the relationship between the Pfaffian and Determinant for an antisymmetric matrix, we can see the possible values of the expression under the product can be $\delta_i = \pm 1$. This formulation can be generalized to three dimensions[7], where there are eight time–reversal invariant points, $\Gamma_{i=n_1n_2n_3} = (n_1\boldsymbol{b}_1 + n_2\boldsymbol{b}_2 + n_3\boldsymbol{b}_3)/2, (n_j = 0, 1)$, and a gauge freedom allows for 16 invariant configurations of δ_i. These can be associated with four $\mathbb{Z}_2$ topological indices $(\nu_0;\nu_1\nu_2\nu_3)$

$$(-1)^{\nu_0} = \prod_{n_j=0,1} \delta_{n_1n_2n_3} \tag{2.7}$$

$$(-1)^{\nu_{i=1,2,3}} = \prod_{n_{j\neq i}=0,1,n_i=1} \delta_{n_1n_2n_3} \tag{2.8}$$

2.1.3 Dirac Phase Connecting Trivial and Topological Insulators

In three-dimensional materials with both time-reversal $\mathcal{T}$ and inversion $\mathcal{P}$ symmetry, the boundary between trivial and topological phases is marked by a Dirac phase with a three-dimensional, four-fold degeneracy with linear dispersion[14, 15]. This transition can be demonstrated using a simple model of a layered heterostructure of normal and strong topological insulators[16, 17, 18]. By varying the thickness and hopping parameters of the different layers, one can continuously simulate the transition between normal and topological

insulating states.

The model is constructed as follows. The most general equation for a Dirac point comes from a coupling of spin $\boldsymbol{\sigma}$ and momentum $\boldsymbol{p} \equiv -i\hbar\boldsymbol{\nabla}$ degrees of freedom: $-i\hbar v_F \boldsymbol{\sigma} \cdot \boldsymbol{\nabla}$. In a strong topological insulator, the Fermi surface encloses an odd number of Dirac points on the surface. If we consider the case of a single point on the surface, the symmetry restricts the spin components to be $\propto \hat{z} \times \boldsymbol{\sigma}$, and the momentum is confined to the plane $\boldsymbol{k}_\perp = (k_x, k_y)$. With the inclusion of hopping terms connecting adjacent layers, the tight-binding Hamiltonian becomes:

$$H(\boldsymbol{k}) = \sum_{\boldsymbol{k}_\perp, i, j} \Big[\, v_F \tau_z (\hat{z} \times \boldsymbol{\sigma}) \cdot \boldsymbol{k}_\perp \delta_{i,j} + \Delta_S \tau_x \delta_{i,j} + \frac{1}{2}\Delta_D \tau_+ \delta_{i,j+1} + \frac{1}{2}\Delta_D \tau_- \delta_{i,j-1} \, \Big] \, c^\dagger_{\boldsymbol{k}_\perp i} c_{\boldsymbol{k}_\perp j} \tag{2.9}$$

where the indices i, j label TI layers, v_F is the Fermi velocity, taken to be the same for each Dirac cone, and the units are taken so that $\hbar = 1$. The Pauli matrices $\boldsymbol{\sigma} = (\sigma_x, \sigma_y, \sigma_z)$ act on the spin degree of freedom, while $\boldsymbol{\tau} = (\tau_x, \tau_y, \tau_z)$ act on top/bottom surface layer degree of freedom, and $\tau_\pm = \tau_x \pm i\tau_y$. The parameter Δ_S controls the hopping between the top and bottom surfaces of the *same* TI layer, while Δ_D controls the hopping between top and bottom surfaces on *different* layers.

The heterostructure is built up in the z direction, with each pair of adjacent TI/NI layers having a total thickness d. Therefore the momentum space Hamiltonian becomes

$$H(\boldsymbol{k}) = \begin{pmatrix} 0 & iv_F k_- & \Delta_S + \Delta_D e^{ik_z d} & 0 \\ -iv_F k_+ & 0 & 0 & \Delta_S + \Delta_D e^{ik_z d} \\ \Delta_S + \Delta_D e^{-ik_z d} & 0 & 0 & -iv_F k_- \\ 0 & \Delta_S + \Delta_D e^{-ik_z d} & iv_F k_+ & 0 \end{pmatrix}, \tag{2.10}$$

where $k_\pm = k_x \pm ik_y$. $H(\boldsymbol{k})$ can be diagonalized to find four bands, which are pairwise

degenerate as guaranteed by Kramer's theorem for this $\mathcal{T}$ symmetric system:

$$\epsilon_{\pm}(\boldsymbol{k}) = \pm\sqrt{v_F^2(k_x^2 + k_y^2) + (\Delta_S^2 + \Delta_D^2 + 2\Delta_S\Delta_D\cos(k_z d))} \tag{2.11}$$

The first term under the root disappears when $k_x = k_y = 0$, and while the second can become zero for particular values of $\cos(k_z d)$ when $\Delta_S = \pm\Delta_D$. In the case of $\Delta_S = -\Delta_D$, the second term can only become zero when $\cos(k_z d) = 1$, resulting in a single four-fold degenerate Dirac node at $|\boldsymbol{k}| = 0$. When $\Delta_S = \Delta_D$ the equation is instead $\cos(k_z d) = -1$, resulting in a Dirac node at the edge of the Brillouin zone, located at $k_z = \pm\pi/d$. For all other values $|\Delta_S| \neq |\Delta_D|$, the band structure is gapped for all $\boldsymbol{k}$.

The Dirac phase at $|\Delta_S| = |\Delta_D|$ marks the critical point between topological and trivial phases, similarly to the Chern insulator model shown in Figure 2.1. The regimes deviating from the critical ratio can be deduced from a physical standpoint. When the TI layers are thin compared to the NI layers, hopping between surfaces on the same layer will dominate $\Delta_S > \Delta_D$, and the system will behave like a trivial insulator. Conversely, a predominantly topological heterostructure with TI layers thicker than NI layers, will be characterized by $\Delta_D > \Delta_S$.

The fourfold degenerate Dirac point is comprised of a pair of two-component Weyl fermions with opposite chirality ± 1. This can be shown explicitly by Taylor expanding the Dirac Hamiltonian around $\boldsymbol{k}_0 = (0, 0, \pi/d)$ for the case $\Delta_S = \Delta_D \equiv \Delta$, and keeping terms up to linear order in momentum $\delta\boldsymbol{k} = \boldsymbol{k} - \boldsymbol{k}_0$. This takes $\Delta_S + \Delta_D e^{\pm\delta k_z d} \to \mp i\tilde{v}_F\delta k_z$, where

$\tilde{v}_F = d\Delta$. The low energy Hamiltonian near the Dirac point becomes

$$H(\delta\boldsymbol{k}) = \begin{pmatrix} 0 & iv_F\delta k_- & -i\tilde{v}_F\delta k_z & 0 \\ -iv_F\delta k_+ & 0 & 0 & -i\tilde{v}_F\delta k_z \\ i\tilde{v}_F\delta k_z & 0 & 0 & -iv_F\delta k_- \\ 0 & i\tilde{v}_F\delta k_z & iv_F\delta k_+ & 0 \end{pmatrix}. \tag{2.12}$$

Performing a unitary transformation , $H'(\delta\boldsymbol{k}) = \mathcal{U}^\dagger H(\delta\boldsymbol{k})\mathcal{U}$, where $\mathcal{U} = (\mathcal{I}+i\tau_x\sigma_z)/\sqrt{2}$, block diagonalizes the low-energy Hamiltonian:

$$H'(\delta\boldsymbol{k}) = \begin{pmatrix} \tilde{v}_F\delta k_z & iv_F\delta k_- & 0 & 0 \\ -iv_F\delta k_+ & -\tilde{v}_F\delta k_z & 0 & 0 \\ 0 & 0 & -\tilde{v}_F\delta k_z & -iv_F\delta k_- \\ 0 & 0 & iv_F\delta k_+ & \tilde{v}_F\delta k_z \end{pmatrix} = \begin{pmatrix} H_+(\delta\boldsymbol{k}) & 0 \\ 0 & H_-(\delta\boldsymbol{k}) \end{pmatrix} \tag{2.13}$$

splitting it into two independent 2×2 blocks $H_\pm(\delta\boldsymbol{k}) = v_F\delta k_y\sigma_x - v_F\delta k_x\sigma_y \pm \tilde{v}_F\delta k_z\sigma_z$, describing Weyl fermions[19]. In this case, the presence $\mathcal{T}$ and $\mathcal{P}$ symmetries constrains the two Weyl fermions to the same point in momentum space, making them topologically unstable, so the Dirac node is eliminated by any perturbation of the ratio $|\Delta_S/\Delta_D|$ away from unity. In general, breaking these symmetries will separate the oppositely charged nodes in momentum space, and produce a topologically stable Weyl semimetal phase, as will be discussed below.

As an aside, it is noted that material realizations of Dirac semimetals fall into two classes: *nonsymmorphic* Dirac semimetals and *topological* Dirac semimetals. In nonsymmorphic Dirac semimetals, the four-fold degeneracy arises at high symmetry points in the Brillouin zone, when the little group describing the point has a four-dimensional irreducible representation. Alternatively, such three-dimensional Dirac points can arise on a rotation axis in the presence of $\mathcal{T}$ and $\mathcal{P}$ symmetry, as the intersection point of pairs of eigenstates

belonging to different representations of the C_n rotation axis little group. Such topological Dirac semimetals can be classified in terms of eigenvalues of the rotation operator C_n for $n = 3, 4, 6$, but are generally unstable, since a perturbation can remove the band inversion without breaking any symmetries.

In the model described above, the four–fold degenerate point corresponds to a topological Dirac semimetal phase. A topological Dirac semimetal phase can only exist in the presence of both time–reversal and inversion symmetry, and vanishes when perturbations breaking these symmetries are introduced. The semimetallic phase obtained by perturbatively removing this Dirac point, can host either topological nodal lines[20] or Weyl points[19, 21], depending on which symmetries remain. Nodal line semimetals can arise in several different ways[22, 23]: protected by mirror symmetry [20], protected by a two-fold screw rotation[24], or in the absence of spin orbit coupling [25, 26]. The existence of Weyl points on the other hand, does not require *any* special symmetries, aside from the translation symmetry of the lattice. The remainder of this chapter will focus on the theoretical description of the various kinds of Weyl semimetals and their properties.

2.2 Weyl Semimetals

The touching of two non-degenerate bands defined by these two-component equations can occur at general points in momentum space $\boldsymbol{k_0}$, when either the $\mathcal{T}$ or $\mathcal{P}$ symmetry specifying the Dirac Hamiltonian is broken[16, 17, 18]. As shown previously, the four-component massless Dirac Hamiltonian in Eq. 2.13 decouples into a pair of 2×2 blocks, each describing a two-component Weyl fermion with either left or right handed chirality. These are a special case of the low-energy linear expansion around a generic degeneracy in momentum space:

$$H_{\text{Weyl}}(\delta\boldsymbol{k}) = \boldsymbol{v}_0 \cdot \delta\boldsymbol{k} + \sum_{i=x,y,z} \boldsymbol{v}_i \cdot \delta\boldsymbol{k}\sigma_i \tag{2.14}$$

where $\boldsymbol{v}_0, \boldsymbol{v}_{x,y,z}$ are the effective velocities describing the dispersion near the degeneracy. The velocity v_0 in the first term determines the tilting of the Weyl cones, controlling the transition between between Type-I and Type-II Weyl semimetal phases, which will be discussed in a later section. The remaining velocities define the chirality of each Weyl fermion, given by $C = \text{sign}(\boldsymbol{v}_x \cdot \boldsymbol{v}_y \times \boldsymbol{v}_z)$. In the special case described above, where $H_\pm(\delta\boldsymbol{k}) = v_F \delta k_y \sigma_x - v_F \delta k_x \sigma_y \pm \tilde{v}_F \delta k_z \sigma_z$, the $C = \pm 1$, confirming that a four-component Dirac node is indeed composed of a pair of two-component Weyl nodes with opposite chirality.

The decoupling of the Dirac point into two oppositely charged Weyl nodes highlights a more general property of these Weyl fermions. The Nielsen-Ninomiya theorem [27] guarantees that in a periodic Hamiltonian, each Weyl point must have a partner of opposite chirality. This can be demonstrated by examining the topological nature of a Weyl node in terms of the Berry phase near the degeneracy. In general, Weyl points are either sources or sinks of Berry curvature, with the integral of Berry curvature $\oint_{\partial V} \boldsymbol{\mathcal{F}}_n(\boldsymbol{k}) \cdot dS = 2\pi C$, over a closed surface V surrounding the node, yielding the chiral charge of the Weyl point. When such a closed surface is extended to fill the entire Brillouin zone, periodicity mandates that the Berry curvature flux through opposite surfaces must be equivalent, meaning the total enclosed chiral charge must be zero. In order to guarantee this, each Weyl node must have a partner of opposite chirality to cancel the total chiral charge in the Brillouin zone.

An important consequence is that unlike Dirac points, Weyl points cannot be removed by introducing a gap through a finite mass perturbation. They can only be removed pairwise, through a perturbation that moves two oppositely charged Weyl points to the same location in momentum space and annihilates them. Additionally, Berry curvature is odd under time-reversal $\mathcal{T}\boldsymbol{\mathcal{F}}_n(\boldsymbol{k}) = -\boldsymbol{\mathcal{F}}_n(-\boldsymbol{k})$, and even under inversion $\mathcal{P}\boldsymbol{\mathcal{F}}_n(\boldsymbol{k}) = \boldsymbol{\mathcal{F}}_n(-\boldsymbol{k})$. A system with both $\mathcal{T}$ and $\mathcal{P}$ symmetry must then necessarily have vanishing Berry curvature, and consequently, one of the two symmetries must be broken in order for Weyl points to appear.

The particular symmetry that is broken also determines the number of Weyl points

that are created. The momentum–space location of a Weyl point $\boldsymbol{k_0}$ is odd under both time-reversal $\mathcal{T}(\boldsymbol{k_0}) = -\boldsymbol{k_0}$, and inversion $\mathcal{P}(\boldsymbol{k_0}) = -\boldsymbol{k_0}$. However, the chirality of the Weyl point transforms differently with $\mathcal{T}$ and $\mathcal{P}$. Inversion symmetry flips the chirality of a Weyl point, so in a system which breaks $\mathcal{T}$, the persisting inversion symmetry guarantees that each Weyl point at $\boldsymbol{k_0}$ will have an opposite chirality partner at $-\boldsymbol{k}_0$, satisfying the theorem. On the other hand $\mathcal{T}$ symmetry leaves the chirality unchanged, so $\mathcal{P}$-breaking systems will have two equal chirality Weyl points at $\pm\boldsymbol{k}_0$. Each of these must have an opposite chirality partner elsewhere in the Brillouin zone, making the total number of Weyl points in inversion-broken systems a multiple of four.

Further features of $\mathcal{T}$ and $\mathcal{P}$-broken Weyl semimetals can be demonstrated by breaking the appropriate symmetries[16, 17, 18] in the model Hamiltonian defined in Eq. 2.9.

2.2.1 $\mathcal{P}$-broken Weyl Semimetal

Inversion symmetry in the basis of the Hamiltonian defined in Eq. 2.9 is given by τ_x, and it can be easily verified that the Hamiltonian is invariant under inversion, $H(\boldsymbol{k}) = \tau_x H(-\boldsymbol{k})\tau_x$. The simplest inversion symmetry breaking term that can be introduced is $V\tau_z$, which conveniently preserves the rotational symmetry around the z-axis. With this term included, the Hamiltonian now becomes

$$H(\boldsymbol{k}) = \sum_{\boldsymbol{k}_\perp, i, j} \Big[\, v_F \tau_z (\hat{z} \times \boldsymbol{\sigma}) \cdot \boldsymbol{k}_\perp \delta_{i,j} + V\tau_z \delta_{i,j} + \Delta_S \tau_x \delta_{i,j} + \frac{1}{2}\Delta_D \tau_+ \delta_{i,j+1} + \frac{1}{2}\Delta_D \tau_- \delta_{i,j-1} \, \Big] c^\dagger_{\boldsymbol{k}_\perp i} c_{\boldsymbol{k}_\perp j} \tag{2.15}$$

which can be diagonalized to find the dispersion

$$\epsilon(k) = \pm\sqrt{\left(V \pm v_F\sqrt{k_x^2 + k_y^2}\right)^2 + (\Delta_S^2 + \Delta_D^2 + 2\Delta_S\Delta_D\cos(k_z d))}. \tag{2.16}$$

The bands are degenerate along the k_z-axis, where $k_x = k_y = 0$. Away from this line, the bands can touch if both terms under the root vanish. For the second term, the situation is equivalent to when $\mathcal{P}$ is not broken, therefore $\Delta_S = \Delta_D$ and $k_z = \pi/d$. The second term can become zero in the difference case, giving the condition $V = v_F\sqrt{k_x^2 + k_y^2}$. Taken together, these constraints result in a continuous degeneracy along a circle radius V/v_F in the $k_z = \pi/d$, called a nodal line (NL). As discussed previously, this kind of extended degeneracy has its own topological properties, but its existence requires additional symmetries.

Since this band touching only occurs when $\Delta_S = \Delta_D$, just as the Dirac point discussed before, it is not robust. In order to obtain a robust phase with topological Weyl nodes, rotational symmetry around the k_z-axis must be broken by making the hopping amplitudes momentum dependent:

$$\begin{aligned}\Delta_S &= \Delta_S^{(0)} + \Delta_S^{(1)}(\boldsymbol{k}) \\ \Delta_D &= \Delta_D^{(0)} + \Delta_D^{(1)}(\boldsymbol{k}).\end{aligned} \tag{2.17}$$

As discussed previously, the minimal number of Weyl points in a periodic inversion-broken system is four, which in this case will be confined to the $k_z = \pi/d$ plane. By preserving the C_2 rotational symmetry around the k_z-axis, and the (xz) and (yz) mirror planes (also sometimes labeled σ_v and σ_v'), we can constrain those four points to be located at $(\pm k_{x0}, \pm k_{y0})$ on a circle. Additionally, since this term must continue to preserve $\mathcal{T}$ symmetry, and must therefore be quadratic in momentum. Simple $\boldsymbol{k}$-dependent terms satisfying all of these symmetries have the form

$$\begin{aligned}\Delta_S^{(1)}(\boldsymbol{k}) &= \delta_S k_x^2 = \delta_S |\boldsymbol{k}|^2 \cos^2\theta \\ \Delta_D^{(1)}(\boldsymbol{k}) &= \delta_D k_x^2 = \delta_D |\boldsymbol{k}|^2 \cos^2\theta\end{aligned} \tag{2.18}$$

where we have introduced a transformation to polar coordinates $k_x, k_y \to |\boldsymbol{k}|, \theta$, and δ_S,

δ_D are tuning parameters. With these momentum-dependent terms included, the vanishing condition for the second term in Eq. 2.16 becomes $\Delta_S^{(0)} + \delta_S|\boldsymbol{k}|^2\cos^2\theta = \Delta_D^{(0)} + \delta_D|\boldsymbol{k}|^2\cos^2\theta$ in the $k_z = \pi/d$ plane. Using the trigonometric identity $\cos^2\theta = (\cos 2\theta + 1)/2$, this can be rearranged to give

$$\cos 2\theta = \frac{2(\Delta_S^{(0)} - \Delta_D^{(0)})}{|\boldsymbol{k}|^2(\delta_D - \delta_S)} - 1. \tag{2.19}$$

This condition has four solutions only when $0 < (\Delta_S^{(0)} - \Delta_D^{(0)})/[|\boldsymbol{k}|^2(\delta_D - \delta_S)] < 1$ corresponding to the four Weyl points on the circle radius V/v_F. It also clarifies the robustness of this phase; unlike the previously required fine tuning of $\Delta_S = \Delta_D$, any small change of the parameters $\Delta_S^{(0)}$, $\Delta_D^{(0)}$, δ_D, and δ_S will not destroy the Weyl nodes, and only shift them in momentum space.

The different phases of this model can be scanned by decreasing $\Delta_S^{(0)}$ starting from the NI phase with $\Delta_S^{(0)} > \Delta_D^{(0)}$ and $\delta_D > \delta_S$, while keeping the remaining parameters fixed.

2.2.2 $\mathcal{T}$-broken Weyl Semimetal

Another way that Weyl points can be realized within this toy model is by breaking time-reversal symmetry. This can be achieved by introducing a $\mathcal{T}$-breaking magnetization term, $b\sigma_z$, perpendicular to the layers in the TI/NI heterostructure:

$$\begin{aligned} H(\boldsymbol{k}) = \sum_{\boldsymbol{k}_\perp,i,j} \Big[& v_F\tau_z(\hat{z}\times\boldsymbol{\sigma})\cdot\boldsymbol{k}_\perp\delta_{i,j} + b\sigma_z\delta_{i,j} + \Delta_S\tau_x\delta_{i,j} \\ & + \frac{1}{2}\Delta_D\tau_+\delta_{i,j+1} + \frac{1}{2}\Delta_D\tau_-\delta_{i,j-1} \Big] c^\dagger_{\boldsymbol{k}_\perp i}c_{\boldsymbol{k}_\perp j} \end{aligned} \tag{2.20}$$

This term introduces a Zeeman-like splitting that breaks the Kramer's degeneracy of the bands, splitting the Dirac cone, which is located at the edge of the Brillouin zone, at $\boldsymbol{k} =$

$(0, 0, \pm\pi/d)$, for $\Delta_S = \Delta_D$. The dispersion of the four bands is now given by:

$$\epsilon(k) = \pm\sqrt{v_F^2(k_x^2 + k_y^2) + \left(b \pm \sqrt{\Delta_S^2 + \Delta_D^2 + 2\Delta_S\Delta_D \cos k_z d}\right)^2} \tag{2.21}$$

which exhibits several phases depending on the values of magnetization b, and the effective mass splitting determined by Δ_S and Δ_D.

The prior condition for degeneracy, arising from the first term under the root, persists for the $\mathcal{T}$-broken case, constraining the Weyl points to $k_x, k_y = 0$. The second term vanishes only for the negative root case, when $b^2 = \Delta_S^2 + \Delta_D^2 + 2\Delta_S\Delta_D \cos k_z d$, which can be inverted to find the locations of the Weyl points $k_z = \frac{\pi}{d} \pm k_0$, where

$$k_0 = \frac{1}{d} \arccos\left(\frac{b^2 - \Delta_S^2 - \Delta_D^2}{2\Delta_S\Delta_D}\right) \tag{2.22}$$

The $[-1, 1]$ domain of the arccos function determines the extent of the Weyl semimetal phase. As b is increased from zero, the system gap disappears when a band touching at $k_z = \pm\frac{\pi}{d}$ first occurs for a value of $b = |\Delta_S - \Delta_D|$. With further increasing magnetization, two Weyl nodes are created and propagate in opposite directions, merging at at $\boldsymbol{k} = 0$, when $b = |\Delta_S + \Delta_D|$. For $b > |\Delta_S + \Delta_D|$, the system is again fully gapped.

Since $\mathcal{T}$-symmetry is broken, it is no longer possible to distinguish between normal and topological insulating states. Nevertheless, our prior definition of Weyl points as topological entities allows us to distinguish the various phases. In the Weyl phase ($|\Delta_S - \Delta_D| < b < |\Delta_S + \Delta_D|$), each k_x-k_y plane for $\frac{\pi}{d} - k_0 < k_z < \frac{\pi}{d} + k_0$ can be thought of as a 2D Chern insulator, which is a direct result of the topological charges of the two Weyl points. Since one of the Weyl points is a source and the other a sink of Berry curvature, there will be a net Berry flux through any plane located between the two topological nodes. Therefore, the initial phase at low b is a trivial insulator, and when the Weyl points merge, the stack of 2D

Chern insulators spans the entire BZ, resulting in a 3D Chern insulator.

2.2.3 Physical properties of Weyl semimetals

The previous discussion summarized the momentum-space topological properties of Weyl points, and showed how this topology can be conveniently understood by describing them as monopoles of Berry curvature. As was the case for topological insulators, the topology of Weyl semimetals manifests itself in various observables, including nontrivial surface states and responses to applied fields.

One of the most striking consequences of the topological Weyl points is the Fermi arcs that connect them at the surface of Weyl semimetals [21, 28]. The existence of such a surface state can be proven using an argument similar to the reasoning used above for the $\mathcal{T}$-broken Weyl semimetal. For a slab constructed in the x-direction, the Brillouin zone of the surface is parametrized by k_y and k_z. Between the Weyl points, for $\frac{\pi}{d} - k_0 < k_z < \frac{\pi}{d} + k_0$, each 2D Chern insulator layer must have a corresponding linearly dispersing chiral edge mode $E \propto \nu k_y$, which is guaranteed to cross the Fermi energy[14]. Taken together, these form a continuous Fermi arc surface state connecting the projections of the Weyl points within the surface Brillouin zone.

These Fermi arcs can be derived explicitly using a minimal two-band lattice model of a Weyl semimetal [29, 30, 31, 32, 33]. The momentum-space component of the Hamiltonian $H(\boldsymbol{k}) = \sum_{\boldsymbol{k}} \left(\tilde{H}(\boldsymbol{k})\right)_{\alpha\beta} c^{\dagger}_{\boldsymbol{k}\alpha} c_{\boldsymbol{k}\beta}$, can be expressed as:

$$\begin{aligned}\tilde{H}(\boldsymbol{k}) = &- \left[m(2 - \cos(k_y) - \cos(k_z)) + 2t_x(\cos(k_x) - \cos(k_0))\right]\sigma_x \\ &- 2t\sin(k_y)\sigma_y - 2t\sin(k_z)\sigma_z. \end{aligned} \tag{2.23}$$

For the model in Eq. 2.23, $\mathcal{T}$-symmetry is broken along the k_x direction, resulting in two

Weyl nodes at $\boldsymbol{k} = (\pm k_0, 0, 0)$. The Fermi arc surface states can be revealed by constructing a slab of this model along the z-direction and imposing finite boundary conditions between the top and bottom surface, as shown in Figure 2.3. The bands for the slab calculation

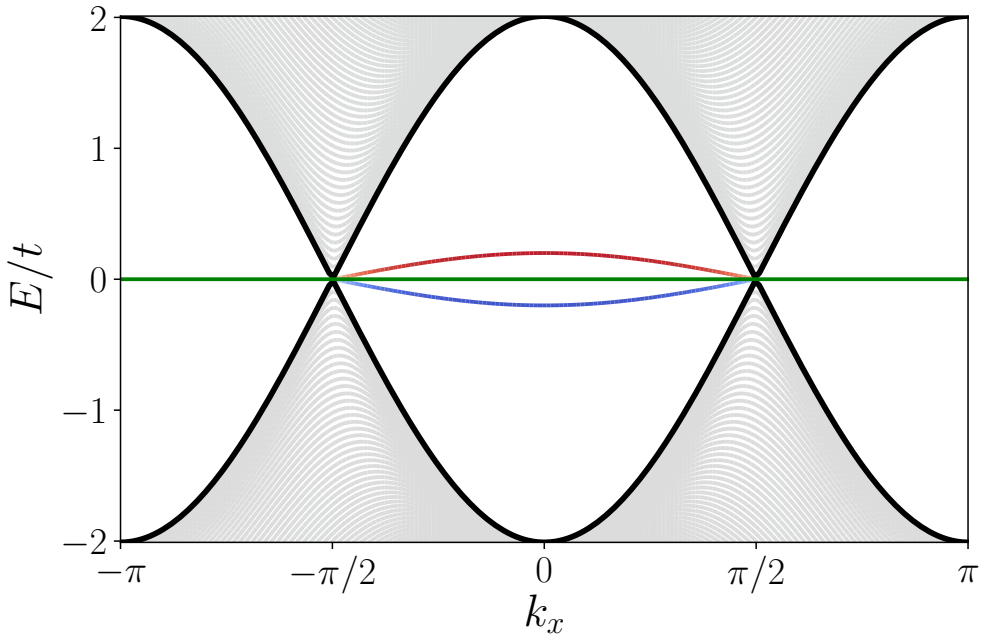

Figure 2.3: Plot of the energy bands along the k_x direction for the model in Eq. 2.23 solved using a 100-unit-cell finite slab in the z-direction with the parameters $k_0 = \pi/2$ and $t_x = t = m/2$. Surface states for the top/bottom surfaces are colored red/blue respectively. The green line marks the Fermi energy $E_F = 0$

are colored based on the probability density of each eigenstate at the surface. To avoid the degeneracy of the Fermi arc states along the k_x axis, an additional symmetry-breaking term $\propto \cos(k_x)\sigma_y$ must be included.

Materials in which $\mathcal{T}$-symmetry broken, for instance by magnetism, will display an extraordinarily large Hall conductivity even in the absence of an external magnetic field, known as the anomalous Hall effect [11]. This can occur as a result of various mechanisms, such as spin-dependent scattering, or intrinsically, as a result of non-trivial Berry curvature. The topology of $\mathcal{T}$-broken Weyl semimetals thus also has a direct effect on their transport, resulting in a semi–quantized intrinsic anomalous Hall effect [34]. Once again, we can argue this is the case by considering the layers between Weyl points as 2D Chern insulators. Each

layer will contribute a factor of e^2/h to the conductivity, meaning the total conductivity is proportional to the separation q of the Weyl points in the Brillouin zone

$$\sigma_{xy} = \frac{e^2}{2\pi h} q \tag{2.24}$$

When multiple features are present, σ_{xy} and other transport properties can be computed directly by taking an integral over the Berry curvature. The anomalous transport properties of Weyl materials will be further explored in Chapter 4.

2.2.4 Type-II Weyl semimetals

One degree of freedom that has not yet been discussed for Weyl points is the tilting of the Weyl cone itself. So far, we have discussed how the low energy excitations around topological Dirac and Weyl points have linear dispersions, similarly to Dirac and Weyl fermions, their massless relativistic analogues in high–energy physics. High–energy physics has the constraint that particles must respect Lorentz symmetry, which forbids any terms that would tilt their cone–like dispersion. However, unlike high–energy physics, particles are instead constrained by the crystal space group symmetry, for which there is no such tilt constraint. Such a tilting term can be written as follows

$$H_0 = \sum_{i,j=1}^{3} \hbar \nu_{ij} k_i \sigma_j + \sum_{i=1}^{3} \nu_{ii} a_i k_i \sigma_0 \tag{2.25}$$

where ν_{ij} is the general velocity tensor for an anisotropic Weyl point, and a_i is a uniform tilting parameter.

This kind of tilting can be visualized using the minimal lattice model provided above, by adding an additional term $\sim \gamma(\cos(k_x) - \cos(k_0))$ to tilt the Weyl cones [33]. When $\gamma > 2t_x$, the Weyl cones tilt below the Fermi energy, resulting in a Type-II Weyl semimetal

phase, as illustrated in Figure 2.4.

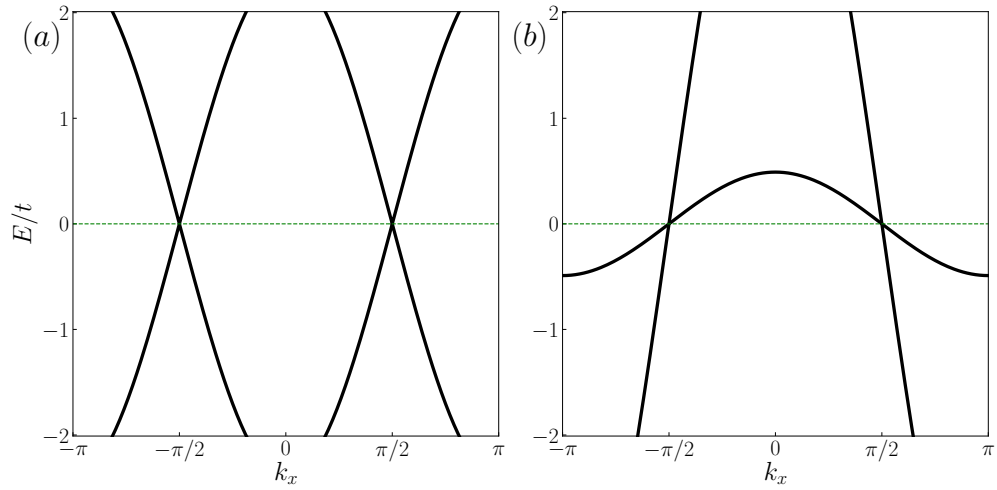

Figure 2.4: Plot of the energy bands along the k_x direction for the model in Eq. 2.23 with an additional term $\sim \gamma(\cos(k_x) - \cos(k_0))$ controlling the tilt of the Weyl cones. Setting $\gamma = 0$ yields untilted, Type-I Weyl cones (a), while $\gamma = 2.5t_x$ yields Type-II Weyl cones tilted below the Fermi energy (b).

The possibility of a term that can tilt the dispersion of a Weyl cone has enormous consequences. In particular, if a Weyl cone is so strongly tilted that the edge falls below the horizontal, its intrinsic properties change dramatically. In such a case, if the Fermi level is fixed to the Weyl energy, the Weyl point occurs at the touching point between electron and hole pockets. This results in a finite density of states at the Fermi level, which can lead to a significant enhancement of transport properties. This enhancement of anomalous Hall and Nernst effects will be discussed further in Chapter 4.

Finally, it should be emphasized that this tilting has no effect on the chiral topological properties of Weyl points. For instance, there can be unequal or odd numbers of Type-I or Type-II Weyls in a material. However, the total number of Weyl points must be even, and there must be equal number Weyl points with opposite chirality, regardless of their type.

Chapter 3

Topological Phases in Real Materials

Chapter 2 described various topological phases and introduced the concept of topological invariants that arise from integrals of the Berry curvature over closed surfaces. In real materials hosting topological phases, these topological invariants lead to the quantization of observable properties such as quantum Hall, quantum spin Hall, and quantum anomalous Hall effects. Chapter 3 will discuss the numerical methods that have been developed for identifying these topological phases in real materials, first demonstrating their application to weakly-correlated materials, and then strongly correlated materials, including lanthanides and actinides. Using specific material examples, we will examine how various topological features inform our understanding of the physics in these complex systems.

The work described in this chapter was done in collaboration with Xiangang Wan and Sergey Savrasov. It is published in Physical Review B [35], Physical Review B (Letters) [36], and Physical Review X [37], and was presented at APS March Meeting 2019 and APS March Meeting 2020.

3.1 Link method for Topological Insulators

There has been recent surge of interest in topological quantum materials, motivated by the robust electronic states which are insensitive to perturbations[1, 14] that exist in these systems. A method has been proposed to detect the protected surface states in topological insulators (TIs) [5] by computing the Z_2 invariants, which for centrosymmetric crystals, reduces to finding band parities of electronic wave functions at time–reversal invariant points in the Brillouin zone (BZ)[7]. For a general case, the calculation of the Z_2 invariant involves an integration of Berry fields [4]

$$D = \frac{1}{2\pi i}\left[\oint_{\partial\mathcal{B}^-} \boldsymbol{\mathcal{A}}(\boldsymbol{k}) - \int_{\mathcal{B}^-} \boldsymbol{\Omega}(\boldsymbol{k})\right], \tag{3.1}$$

where the region $\mathcal{B}^-$ is defined as the lower half-plane in the Brillouin zone $[-\pi,\pi]\otimes[-\pi,0]$, and $\partial\mathcal{B}^-$ – its boundary. $\boldsymbol{\mathcal{A}}(\boldsymbol{k}) = \langle u_n(\boldsymbol{k})|i\boldsymbol{\nabla}_{\boldsymbol{k}}|u_n(\boldsymbol{k})\rangle$ is the Berry connection, and $\boldsymbol{\Omega}_n(\boldsymbol{k}) = \boldsymbol{\nabla}_{\boldsymbol{k}} \times \langle u_n(\boldsymbol{k})|i\boldsymbol{\nabla}_{\boldsymbol{k}}|u_n(\boldsymbol{k})\rangle$ is the Berry curvature, which are defined in terms of the periodic part of the Bloch wavefunction $|\psi(\boldsymbol{k})\rangle = e^{i\boldsymbol{k}\cdot\boldsymbol{r}}|u_n(\boldsymbol{k})\rangle$ of the electron within the crystal. The Berry curvature is often expressed in tensor form $\Omega^n_{\mu\nu}$, which is related to the vector form through the Levi-Cività symbol $\Omega^n_{\mu\nu} = \epsilon_{\mu\nu\xi}(\boldsymbol{\Omega}_n)_\xi$. Using the identity $\langle u_n(\boldsymbol{k})|\boldsymbol{\nabla}_{\boldsymbol{k}}H(\boldsymbol{k})|u_{n'}(\boldsymbol{k})\rangle = [\epsilon_n(\boldsymbol{k}) - \epsilon_{n'}(\boldsymbol{k})]\langle u_n(\boldsymbol{k})|\boldsymbol{\nabla}_{\boldsymbol{k}}|u_{n'}(\boldsymbol{k})\rangle$, where $\epsilon_n(\boldsymbol{k})$ are the eigenenergies of the Hamiltonian $H(\boldsymbol{k})$, the Berry curvature can be expressed as the sum [11, 9]

$$\begin{aligned}\Omega^n_{\mu\nu}(\boldsymbol{k}) &= i\sum_{n'\neq n}\frac{\langle u_n(\boldsymbol{k})|\partial H/\partial k_\mu|u_{n'}(\boldsymbol{k})\rangle\langle u_{n'}(\boldsymbol{k})|\partial H/\partial k_\nu|u_n(\boldsymbol{k})\rangle - (\mu\leftrightarrow\nu)}{[\epsilon_n(\boldsymbol{k}) - \epsilon_{n'}(\boldsymbol{k})]^2} \\ &= i\sum_{n'\neq n}\frac{\langle u_n(\boldsymbol{k})|v_\mu(\boldsymbol{k})|u_{n'}(\boldsymbol{k})\rangle\langle u_{n'}(\boldsymbol{k})|v_\nu(\boldsymbol{k})|u_n(\boldsymbol{k})\rangle - (\mu\leftrightarrow\nu)}{[\epsilon_n(\boldsymbol{k}) - \epsilon_{n'}(\boldsymbol{k})]^2}.\end{aligned} \tag{3.2}$$

Here the second form can be obtained by using the definition of the velocity operator

$$\boldsymbol{v}(\boldsymbol{k}) = \frac{1}{i\hbar}[\boldsymbol{r}, H(\boldsymbol{k})] = \frac{1}{\hbar}\boldsymbol{\nabla}_{\boldsymbol{k}}H(\boldsymbol{k}). \tag{3.3}$$

The expression for the Z_2 invariant (Eq. 3.1) has been implemented in numerical electronic structure calculations[38] using density functional theory. The implementation is defined on the reciprocal lattice of the Brillouin zone with the translations $\mathbf{G}_{\nu=1,2,3}$, which is divided into $N_1 \times N_2 \times N_3$ microcells spanned by the primitive vectors $\mathbf{q}_{\nu=1,2,3} = \mathbf{G}_\nu / N_\nu$. A link variable can be defined between adjacent pairs of $\boldsymbol{k}$-points on the grid,

$$U_{\mathbf{q}}(\boldsymbol{k}) = \frac{\det\left[\langle \boldsymbol{k} + \boldsymbol{q} j' | e^{i\boldsymbol{q}\boldsymbol{r}} | \boldsymbol{k} j \rangle\right]}{\left|\det\left[\langle \boldsymbol{k} + \boldsymbol{q} j' | e^{i\boldsymbol{q}\boldsymbol{r}} | \boldsymbol{k} j \rangle\right]\right|} \tag{3.4}$$

which represents a $U(1)$ angle. Using this link variable, discrete analogues for the Berry connection $A_\mu(\boldsymbol{k}) \sim \boldsymbol{\mathcal{A}}(\boldsymbol{k})$ and Berry curvature $F_{\mu\nu}(\boldsymbol{k}) \sim \Omega^n_{\mu\nu}(\boldsymbol{k})$, can be introduced

$$\begin{aligned} A_\mu(\boldsymbol{k}) &= \ln U_{q_\mu}(\boldsymbol{k}) \\ F_{\mu\nu}(\boldsymbol{k}) &= \ln \frac{U_{q_\mu}(\boldsymbol{k}) U_{q_\nu}(\boldsymbol{k} + q_\mu)}{U_{q_\mu}(\boldsymbol{k} + q_\nu) U_{q_\nu}(\boldsymbol{k})}. \end{aligned} \tag{3.5}$$

When arbitrarily fine grids are used for evaluation these analogues converge to the exact values of the Berry connection and Berry curvature respectively. Moreover, an analogue of the continuous relationship $\boldsymbol{\Omega}_n(\boldsymbol{k}) = \boldsymbol{\nabla}_{\boldsymbol{k}} \times \boldsymbol{\mathcal{A}}(\boldsymbol{k})$ can be written using a discrete derivative $\Delta_\mu f(\boldsymbol{k}) = f(\boldsymbol{k} + q_\mu) - f(\boldsymbol{k})$:

$$F_{\mu\nu}(\boldsymbol{k}) = \Delta_\mu A_\nu(\boldsymbol{k}) - \Delta_\nu A_\mu(\boldsymbol{k}) + 2\pi i n_{\mu\nu}(\boldsymbol{k}), \tag{3.6}$$

where $n_{\mu\nu}(\boldsymbol{k})$ is an integer field that matches the complex logarithmic branches $\in (-\pi, \pi)$ of the two sides. As a result, the discrete version of Eq. 3.1

$$D = \frac{1}{2\pi i}\left[\sum_{\boldsymbol{k}\in\partial\mathcal{B}^-} A_\mu(\boldsymbol{k}) - \sum_{\boldsymbol{k}\in\mathcal{B}^-} F_{\mu\nu}(\boldsymbol{k})\right] = -\sum_{\boldsymbol{k}\in\mathcal{B}^-} n_{\mu\nu}(\boldsymbol{k}) \tag{3.7}$$

is guaranteed to be an integer. Additionally, this form has been shown to be quite numerically stable, yielding the correct values of topological indices even for relatively coarse $10 \times 10 \times$

10 $\boldsymbol{k}$-point grids [38, 39]. The development of this method has allowed for high-throughput searches to identify candidate materials hosting topological insulator phases [40, 41, 42].

3.2 Link method for Topological Points and Lines

Weyl semimetals (WSMs) are systems closely related to topological insulators and characterized by a bulk band structure which is fully gapped except at isolated points described by the 2x2 Weyl Hamiltonian [14]. Sometimes these Weyl points extend into lines in the BZ giving rise to nodal line semimetals (NLSMs) [20]. Due to their intriguing properties such as Fermi arc surface states [21], chiral anomaly induced negative magnetoresistance [27], and a semi–quantized anomalous Hall effect [29, 16], the search for WSM materials is currently very active. Unfortunately, their identification in infinite space of chemically allowed compounds represents a challenge: there is no corresponding topological index characterizing WSM phase, and the Weyl points may appear randomly in the bulk BZ. General principles, such as broken time reversal or inversion symmetry, or emergence of the WSM phase between topologically trivial and non–trivial insulating phases [21] are too vague to guide their high throughput screening, and recent group theoretical arguments[43, 44] to connect crystal symmetry with topological properties still await their practical realization. The progress in this field was mainly serendipitous, although the ideas based on band inversion mechanism[12] or analyzing mirror Chern numbers[45, 46] were proven to be useful in many recent discoveries[47, 48, 49, 50, 51, 52], and computer oriented searches of topological semimetals are beginning to appear [53, 54, 55].

Here we propose a straightforward method to identify Weyl semimetals by using a well–known result that every Weyl point acts as a Dirac monopole [19, 56] producing a non–zero Berry flux when it is completely enclosed by a surface in the BZ. The enclosed charge is given by the chirality of the Weyl point similarly to Gauss's theorem in Coulomb's law.

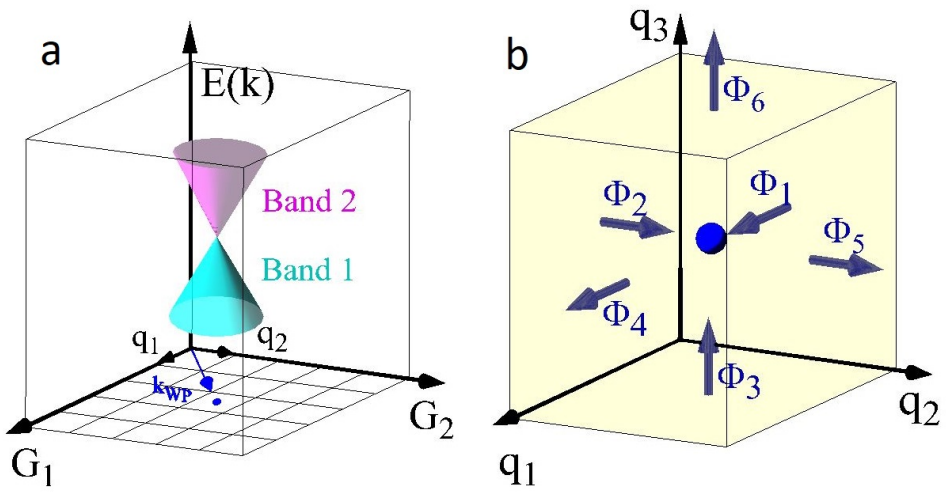

Figure 3.1: a. A typical cone dispersion relationship $E(\mathbf{k})=\pm v|\mathbf{k}-\mathbf{k}_{WP}|$ for the Weyl point plotted within a rectangular area in k–space set by divisions of reciprocal lattice translations $\mathbf{G}_1$ and $\mathbf{G}_2$ for a fixed value along the third translation $\mathbf{G}_3$. b. The Weyl point located within a microcell set by the grid vectors $\mathbf{q}_1, \mathbf{q}_2, \mathbf{q}_3$ generates a Berry flux through each plaquette as given by the (right handed) circulation of the Berry connection with sign convention defined in text.

Rectangular grids of k–points that are widely employed in self–consistent electronic structure calculations for the BZ integration either via special points (Monkhorst-Pack) technique [57] or a tetrahedron method[58], are ideally suited for this purpose since they divide the volume of the BZ onto microcells and the electronic wave functions are automatically available at the corners of each microcell. It is thus a matter of rearranging the data to extract Berry phases of these wave functions in order to recover the Dirac monopoles inside the BZ. While there are some uncertainties connected to energy bands cutoffs used while defining Berry fields for metallic systems, our method allows a subsequent refinement provided a signal from a monopole is detected. The entire procedure resembles data mining technology used in computer science as an intelligent method to discover patterns from large data sets in a (semi–) automatic way so that the extracted data can subsequently be used in further analysis.

Since we are dealing with grids, there is a chance that the grid microcell will enclose both chiral positive and negative charges whose Berry fluxes cancel each other. Although

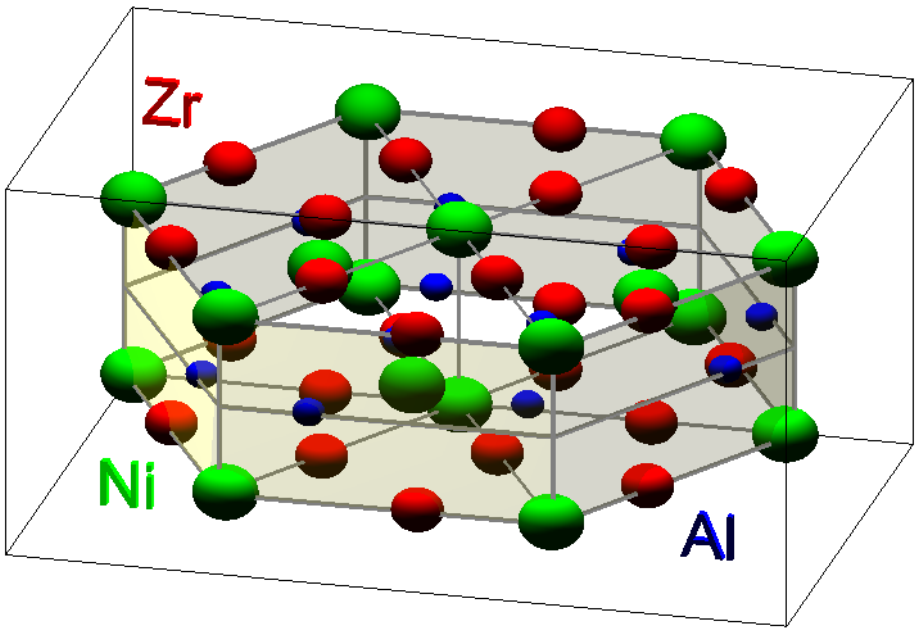

Figure 3.2: ZrNiAl–type crystal structure (# 189 space group $p\bar{6}2m$) of noncentrosymmetric hexagonal compounds compounds studied in this work.

the resolution here is obviously adjustable by changing the grid size, and modern computers allow thousands and even millions of k–points to be handled in parallel, trying to identify Weyl points that are very close makes no sense from both practical and fundamental reasons. Practically, properties such as anomalous Hall effect[29, 16] are proportional to the distance between the Weyl points and so does the density of Fermi arc surface states[21]. Disorder, electronic interactions, thermal broadening and Heisenberg uncertainty principle provide fundamental limitations. Therefore, distances between the Weyl points need not be smaller than a few percent of the reciprocal lattice spacing, and this does not require dealing with very dense grids.

Now we will outline the method to evaluate the Berry flux due to a single Weyl point appearing somewhere in the bulk BZ with the typical dispersion relationship $E(\mathbf{k}) = \pm v|\mathbf{k} - \mathbf{k}_{WP}|$, as illustrated in Fig.3.1a. Proceeding in the same way as we did for topological insulators, we use the link variable $U_{\mathbf{q}}(\mathbf{k})$ on the edges of k-grid microcells into which the BZ is divided.

In Eq. 3.4, the matrix elements between the periodic parts of the wave functions are cast into the form $\langle \mathbf{k}+\mathbf{q}j'|e^{i\mathbf{qr}}|\mathbf{k}j\rangle$, which frequently appear in density functional linear response calculations[59] and thus are straightforward to evaluate. The set of energy bands j is spanned over occupied states and includes those that cross the Fermi level. However, some uncertainty exists in this enumeration procedure because the Berry flux from the negative and positive branches of the monopole (bands 1 and 2 for the example shown in Fig.3.1a)will cancel each other. For the example being discussed, this means that either band 1 or 2 (but not both) needs to be taken into account while evaluating Eq.3.4. In real materials, this may result in contribution for some monopoles cancelling, but since we are mostly interested in the Weyl points in the immediate vicinity of the Fermi level, varying the upper cutoff value for j by one or two will resolve this problem. We also note that the link field $U_{\mathbf{q}}(\mathbf{k})$ needs to be computed for the entire grid of k–points, where the group symmetry operations help to generate the wave functions that are normally available within only irreducible portion of the BZ.

We now evaluate the Berry flux through faces of each microcell of the $N_1 \times N_2 \times N_3$ grid. This is illustrated in Fig.3.1b, where the flux $\Phi_{i=1..6}$ through each plaquette with the origin at particular $\mathbf{k}$ and spanned by a pair of vectors $q_\mu q_\nu$ is conveniently encoded into the following formula

$$2\pi\Phi \equiv Im \ln \left[\frac{U_{\mathbf{q}_\mu}(\mathbf{k}) U_{\mathbf{q}_\nu}(\mathbf{k}+\mathbf{q}_\mu)}{U_{\mathbf{q}_\nu}(\mathbf{k}) U_{\mathbf{q}_\mu}(\mathbf{k}+\mathbf{q}_\nu)} \right], \tag{3.8}$$

which differs in convention from Eq. 3.5 by a factor of 2π. This procedure is similar to one employed while evaluating Z_2 invariants [38] on six two–dimensional tori introduced in Ref. [60] but now the roles of the tori are played by the slices of the BZ spanned by each pair of the reciprocal vectors $G_\mu G_\nu$ with a fixed value along the third vector G_ξ. We only need to take care of the fact that the flux as given by Eq. 3.8 produces right (alternatively left) handed circulation of the Berry connection but inner (or outer) normal should be chosen

consistently for the total flux through each surface of the microcell. Thus, the total Berry flux is given by

$$c = \Phi_1 + \Phi_2 + \Phi_3 - \Phi_4 - \Phi_5 - \Phi_6 \tag{3.9}$$

Although the flux through each plaquette is generally non–integer, the total flux is guaranteed to be an integer since individual contributions (3.8) from adjacent plaquettes cancel each other in Eq.(3.9), up to an addition of $2\pi n$. Therefore c returns ether the chiral charge of the monopole or zero.

The entire algorithm is now viewed as an automated procedure that is either done following the self–consistent band structure calculation or "on the fly". We illustrate it on the example of TaAs Weyl semimetal whose electronic properties are well documented in recent literature [48]. We use a full potential linear muffin–tin orbital method (FP LMTO) developed by one of us [61] and perform a self–consistent density functional calculation with spin–orbit coupling using the Generalized Gradient Approximation [62]. We subsequently set up a k–grid using $20 \times 20 \times 20$ divisions of the reciprocal lattice unit cell. These types of grids were previously shown to be sufficient for calculating Z_2 invariants in topological insulators[63]. For evaluating the link field, Eq. (3.4), the energy window is chosen to span the entire valence band with the cutoff value corresponding to the band number that crosses the Fermi level. It appears this is sufficient to recover all monopoles. The net result is that 24 out of 8000 microcells produce non–zero Berry flux and yield approximate positions for the Weyl points. We take the coordinates of the corresponding microcells (only non–equivalent by symmetry are needed; two for TaAs) and mine these areas of k–space by introducing similar rectangular grids inside each microcell in order to refine the locations of the Weyl points to the positions: $(0.009, 0.506, 0)$, $(0.019, 0.281, 0.579)$ in units $2\pi/a, 2\pi/a, 2\pi/c$. This is in agreement with the previous calculation [48].

We also considered CuF, recently predicted to be a Weyl semimetal by one of us[52]. The exact same setup ($20 \times 20 \times 20$ divisions with the energy panel spanning up to the band that crosses the Fermi level) returns 24 microcells that are all related by symmetry. Zooming into one microcell returns the following location of the Weyl point: $(0.281, 0.119, 0)2\pi/a$, consistent with our previous result [52].

3.3 Application to weakly correlated materials with broken inversion symmetry

To demonstrate the predictive power of the method, we scanned several hundred non-centrosymmetric hexagonal compounds in the $p\bar{6}2m$ (# 189) space group with the ZrNiAl structure (see Fig. 3.2). Their complete crystallographic data can be found in Ref. [64]. Topological electronic structures in few of these systems have already drawn recent attention. CaAgP was predicted to be a line–node Dirac semimetal while CaAgAs was found to be a strong topological insulator [65]. Similar properties have been discussed for NaBaBi under pressure[66]. We perform self–consistent band structure calculations and subsequent monopole mining procedure in exactly the same manner as we illustrated for TaAs and CuF. The experimental lattice constants from Ref. [64] were used, and the discrepancies caused by deviations from the theoretically predicted lattice parameters were found to be small.

As many of the compounds in this structure include rare earth elements with their f electron states appearing in the vicinity of the Fermi level, we first provide a list of only those compounds that do not explicitly include Lanthanides (see Table 3.1). These are the systems for which density functional based calculations can be trusted in general. Quite a few of them include magnetic elements (such as Fe) which can potentially develop a magnetic order at low temperatures. Unfortunately, the literature contains very limited information

about the existence of magnetism and the type of order (ferro, antiferro, incommensurate, *etc.*), and at the absence of established theoretical procedures to search for the lowest energy ground state in infinite space of possible magnetic configurations, all calculations reported here assume a paramagnetic ground state.

We can also comment on the compounds that include Lanthanide elements. They can be separated into two large groups. The first group includes the materials where the narrow f–band appears crossing the Fermi level in the calculated band structures. This would be an indication that a many–body renormalization of the single particle spectra (such, e.g., as band narrowing, multiplet transitions, etc) is expected. Although modern electronic structure approaches based on combinations of density functional and dynamical mean field theories [67] allow handling such cases, those are outside the scope of the present study, and we do not study topological properties of these compounds. The second group includes the materials with either fully empty or fully occupied f band, namely f^0 : LaAuCd, LaAuIn, LaAuMg, LaCuIn, LaCuMg, LaInMg, LaIrSn, LaNiIn, LaNiZn, LaPdCd, LaPdHg, LaPdIn, LaPdMg, LaPdPb, LaPdSn, LaPdTl, LaPtIn, LaPtPb, LaPtSn, LaRhIn, LaRhSn, LaTlMg; f^{14}: LuAsPd, LuAuIn, LuAuZn, LuCuIn, LuGaMg LuGeAg, LuGeLi, LuInMg, LuIrSn, LuNiAl LuNiIn, LuNiPb, LuPbAg, LuPdIn, LuPdSn LuPdZn, LuPtIn, LuPtSn, LuRhSn, LuSiAg, LuTlMg. These are the cases where static mean field description can in principle capture single particle excitations (apart from the question whether the position of the f–band is correctly predicted by such theory).

There are a few materials that include Sm ion with its non–magnetic configuration f^6 : SmAgMg, SmAuCd, SmAuIn, SmAuMg, SmCuAl, SmCuIn, SmIrIn, SmIrSn, SmNiAl, SmNiIn, SmNiSn, SmNiZn, SmPdCd, SmPdHg, SmPdIn, SmPdMg, SmPdPb, SmPdTl, SmPtIn, SmPtMg, SmPtPb, SmPtSn, SmRhIn, SmRhSn, SmSiAg, SmTlMg. Here $j = 5/2$ and $j = 7/2$ subbands appear below and above the Fermi level, respectively. The Coulomb renormalzation in these compounds has a predictable effect by renormalizing the spin–orbit

Table 3.1: List of noncentrosymmetric hexagonal compounds in the $p\bar{6}2m$ (# 189) space group with the ZrNiAl structure studied in this work. The compounds containing a Lanthanide element are explicitly excluded from the Table.

Class	X =	Class	X =	Class	X =
YXMg	In, Au, Tl, Ga, Cu, Al	ZrGeX	Os, Zn	XNiGa	Hf, Zr
CrAsX	Ti, Pd, Fe, Co, Ni, Rh	XPtIn	Sc, Y	MnGeX	Pd, Rh
ScGeX	Fe, Rh, Cu, Os, Pd, Ru	ZrCoX	Ga, Sn	HfXRu	P, As
MnAsX	Ti, Ni, Rh, Fe, Ru	TiGeX	Co, Pd	CrPX	Pd, Ni
YPdX	Mg, Al, Tl, In, Zn	XAsOs	Hf, Zr	XPdPb	Ca, Y
YXIn	Ni, Rh, Au, Cu	TiPX	Cr, Os, Ru	ScPX	Ir, Na
XSiRe	Hf, Ta, Ti, Zr	ZrXRu	Si, As, P	XSiMn	Nb, Ta
HfGeX	Fe, Os, Rh, Ru	MnPX	Rh, Pd, Ni	ZrPX	Os, Mo
FeAsX	Ti, Co, V, Ni	CaXCd	Ge, Sn, Pb	NbCrX	Ge, Si
XPNi	Fe, Mo, W, Co	ScSiX	Cu, Ru, Mn	HfSiX	Os, Ru
XGeMn	Hf, Nb, Sc, Ta	XNiAl	Hf, Y, Zr	CaXAg	P, As
XAsPd	Hf, Ti, Zr, Mn	YXAg	Pb, Si, Mg	XBFe	Nb, Ta
Other: YRhSn, YPtSn, YAuCd, YAuZn, YCuAl, YSiLi, YGeLi BaBiNa, ScGeAg, ScSnAg, HfIrSn					

coupling through a Hubard–type interaction, and the states in the immidiate vicinity of the Fermi level are not affected.

Out of the compounds that we studied, we clearly identify 11 materials which show WSM behavior, 1 NLSM and 1 hosting both Weyl points and nodal lines. The two NLSMs also host topologically distinct triple fermion points [68]. Table 3.2 summarizes our results for each compound , giving the locations of the non–equvalent low–energy Weyl and/or triple points, their number and energies relative to E_F in eV. We find both Type-I and Type-II Weyl points in these systems, according to classification introduced in Ref. [69]. Complete crystallographic and electronic structure data for these compounds is given in Appendix A.

Many of the Weyl semimetals that we predict in our work display remarkably similar locations of their Weyl points. LaInMg[70], LuGeAg[71], YGeLi[72],YPbAg[73], and YSiAg[74], exhibit 6 pairs (chiral positive and negative) of points, that are all symmetry related and are only slightly displaced from the $k_z = 0$ plane. They are located along the ΓM direction in the BZ. We illustrate their precise positions for LaInMg in Fig. 3.3a and refer

Table 3.2: List of non–equivalent Weyl and triple points (in units $2\pi/a, 2\pi/a, 2\pi/c$), their number and energies relative to the Fermi level (in eV) recovered using the monopole mining method for noncentrosymmetric hexagonal compounds in the $p\bar{6}2m$ (# 189) space group with the ZrNiAl structure that are predicted to exhibit Weyl/nodal line semimetal behavior. The typical appearance of the Weyl points in the Brillouin Zone is cited by referencing to either sort A or B as illustrated in Fig. 3.3ab.

Compound	Topological Points	Sort	#	E (eV)
LaInMg	$(0.00000, 0.36868, 0.01123)$	Weyl-A	12	$-$ 0.06
LuGeAg	$(0.00000, 0.42190, 0.00098)$	Weyl-A	12	$-$ 0.23
YGeLi	$(0.00000, 0.27793, 0.00817)$	Weyl-A	12	$-$ 0.13
YPbAg	$(0.00000, 0.40335, 0.03142)$	Weyl-A	12	$-$ 0.09
YSiAg	$(0.00000, 0.37864, 0.00384)$	Weyl-A	12	$-$ 0.09
HfPRu	$(0.46280, 0.06931, 0.02210)$	Weyl-B	24	+ 0.06
ZrPRu	$(0.45982, 0.07532, 0.01698)$	Weyl-B	24	+ 0.06
LaTlMg	$(0.00000, 0.38916, 0.03236)$	Weyl-A	12	$-$ 0.13
	$(0.41450, 0.02567, 0.00724)$	Weyl-B	24	$-$ 0.13
YTlMg	$(0.00000, 0.43303, 0.02319)$	Weyl-A	12	$-$ 0.05
	$(0.44076, 0.02908, 0.00441)$	Weyl-B	24	$-$ 0.11
LuAsPd	$(0.00000, 0.11481, 0.14140)$	Weyl-A	12	+ 0.18
	$(0.00000, 0.12004, 0.13942)$	Weyl-A	12	+ 0.19
ZrAsOs	$(0.47365, 0.02591, 0.04792)$	Weyl-B	24	+ 0.02
	$(0.47406, 0.01215, 0.04789)$	Weyl-B	24	+ 0.02
TiGePd	$(0.00000, 0.00000, 0.16495)$	Triple	2	+ 0.14
	$(0.00000, 0.00000, 0.20775)$	Triple	2	+ 0.12
VAsFe	$(0.00000, 0.00000, 0.32279)$	Triple	2	+ 0.14
	$(0.00000, 0.00000, 0.47625)$	Triple	2	+ 0.19
	$(0.00000, 0.38339, 0.17269)$	Weyl-A	12	+ 0.09

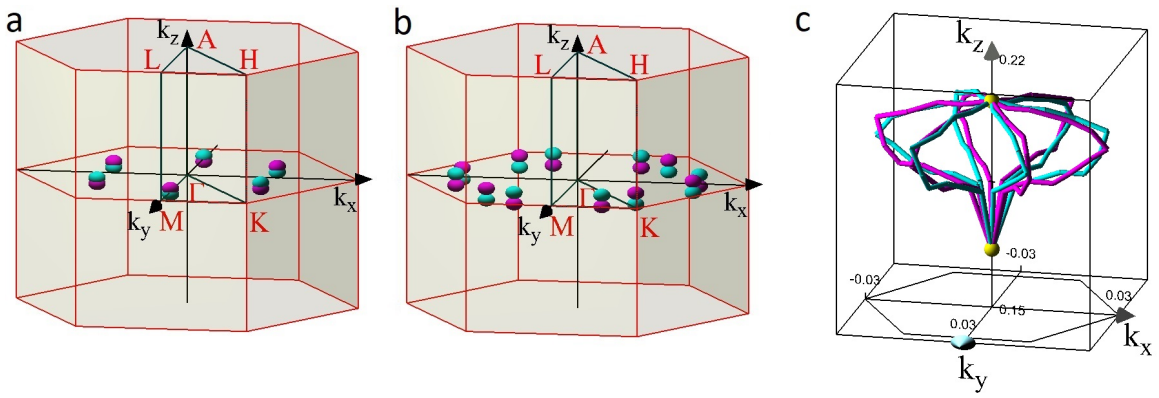

Figure 3.3: a. Positions of 6 pairs (cyan for chiral positive and magenta for chiral negative) of low–energy Weyl points seen along the ΓM direction in the BZ for LaInMg and referenced in Table 3.2 as sort A; b. Positions of 12 pairs of Weyl points that are shifted symmetrically away from the ΓK line for HfPRu and referenced in Table 3.2 as sort B; c. A set of nodal lines for TiGePd that is recovered by the monopole mining method presented in this work. The color (cyan and magenta) distinguishes chiral positive and negative lines, respectively. The zoomed area of the BZ is bounded by $0.15 \leq 2\pi k_z/c \leq 0.22$ and $-0.03 \leq 2\pi k_{x,y}/a \leq +0.03$. Also shown in yellow are the triple degenerate topological points [68].

to them in Table 3.2 as Weyl points of sort A. We find that HfPRu[75], and ZrPRu[70] show another sort (referred to as sort B) of Weyl points, namely 12 pairs that are shifted symmetrically away from the ΓK line (see Fig. 3.3b). Interestingly, LaTlMg[76] and YTlMg[70] host both sorts (A and B) of Weyl points. LuAsPd[77] shows two sets of sort A Weyl points (24 total), while ZrAsOs[78] shows two sets of sort B Weyl points (48 total). Their displacement from the $k_z = 0$ plane is much larger than that found in previous cases. For each reported Weyl point, we also provide independent verification by calculating the band structures along k_x, k_y and k_z directions with the boundary vectors confining the Weyl point. These data can be found in Appendix A.

Another interesting outcome of our high–throughput screening is the materials exhibiting nodal lines and triple–point fermions. TiGePd[79] and VAsFe[80] both host 12 pairs (chiral positive and negative) of nodal lines that are located very close to the ΓA direction in the BZ. We illustrate this behavior for TiGePd in Fig. 3.3c by zooming into the area of the BZ bounded by $0.15 \leq 2\pi k_z/c \leq 0.22$ and $-0.03 \leq 2\pi k_{x,y}/a \leq +0.03$. Interestingly,

the nodal lines start and end at triple degenerate points that have recently enriched our classification of topological features [68]. These triple points are located along the ΓA line of the BZ. We provide their coordinates for TiGePd and VAsFe in Table 3.2.

One of the most striking features of Weyl semimetals is the presence of the Fermi arcs in their one–electron surface spectra[21]. Although computations of their shapes are possible via a self–consistent supercell (slab) calculation of the surface energy bands, given the number of compounds that we consider in this work, it is a computationally demanding study. Nevertheless, since the arcs connect the Weyl points of different chirality, one can expect that most of the materials that we list in Table 3.2 would have rather short arcs since the distances between positive and negative chiral charges are quite small. One notable exception is VAsFe which, as we list in Table 3.2, exhibits not only nodal lines and triple points, but also a set of Weyl points which are well separated from each other. These are expected to produce very long Fermi arcs for the (100) or (110) crystallographic types of surfaces. We have recently shown [32] that long and straight Fermi arcs are generally capable of supporting nearly dissipationless surface currents, therefore it could be interesting to explore such possibility in VAsFe.

In conclusion, we presented an automated monopole mining method to identify Weyl and nodal line semimetals. We tested the method by recovering the Weyl points in several known systems as well as demonstrating its predictive power by high throughput screening hundreds noncentrosymmetric hexagonal compounds in the $p\bar{6}2m$ (# 189) space group and finding 13 materials whose locations of the topological nodal points and lines have been reported. As we judge from our calculated energy bands, the WSMs identified in this work exhibit regular Fermi surface states, while the Weyl points are not exactly pinned at the Fermi level. This is similar to other recently discovered WSMs, such as TaAs[48], for which a large negative magnetoresistance has been recently measured[81]. Despite the latter representing a signature of the much celebrated chiral anomaly feature in Weyl semimetals, there exists

an obvious problem of distinguishing contributions from the Weyl points and regular Fermi states. In this regard, our automated approach should be helpful for scanning vast material databases in identifying an ideal WSM with only nodal points at the Fermi level as it was originally envisioned in pyrochlore iridates[21]

3.4 Application to a class of strongly correlated superconductors

Superconductivity (SC) in non-centrosymmetric compounds has received much attention due to their potential for hosting unconventional pairing states. The lack of inversion symmetry permits antisymmetric spin-orbit coupling (ASOC), which splits the Fermi surface (FS) and mixes spin-singlet and spin-triplet SC pairing states. This ASOC can also lead to topological features. Here we apply the methods discussed in previous sections to identify topological features in a class of inversion–broken superconductors and consider the effect of topology on the superconducting state.

The $CeTX_3$ (T = Co, Rh, Ir, X = Si, Ge) family of compounds crystallize in the $BaNiSn_3$-type structure ($I4mm$ space group no. 107), which breaks spatial inversion symmetry. With the exception of paramagnetic $CeCoSi_3$, their low-temperature phases are anti-ferromagnetic (AF) at ambient pressure. Application of pressure suppresses the Néel temperature to zero, where the magnetic ground state gives way to SC. The SC in this group exhibits many unconventional features, including upper critical fields H_{cw} that far exceed the Pauli limiting field $H_p[T] \sim 1.86T_C[K]$[82, 83, 84, 85, 86, 87, 88, 89] which has been suggested as evidence of an odd parity SC gap function. Recent works argue that AF fluctuations play a role in the development of SC, indicating the importance of the spin structure to the unconventional physics in these compounds.

The absence of inversion symmetry is also a necessary ingredient for the existence of topological Weyl points. Since the role of ASOC and lack of inversion symmetry in the development of the SC state is not well understood, we hope to shed some light by investigating the topological properties of these materials. Furthermore, the narrow Ce-4f band is sensitive to temperature and pressure, allowing Weyl points to be tuned without introduction of chemical or site disorder. This feature makes these heavy fermion materials promising candidates for the study of Weyl physics [90] in the proximity of SC and quantum criticality.

Our electronic structure calculations are performed within the framework of the full potential linear muffin–tin orbital method with spin-orbit coupling, using the experimentally measured lattice parameters [91, 92, 93, 94]. The compounds are locked to the paramagnetic state to mimic the experimentally observed suppression of magnetism by pressure. The on-site interactions between the Ce-4f electrons must be treated with special care, as the strong Coulomb repulsion narrows the bandwidth considerably. We handle renormalization of quasiparticle bands through the LDA+Gutzwiller (LDA+G) method, taking Hubbard U values of 5eV and 6eV[95]. The method is described in more detail in Refs. [96, 97, 98, 99, 100]

In LDA+G, the double-counting potential must carefully be chosen to account for the Coulomb correction included in both the single-particle and interacting terms of the Hamiltonian. Specifically, for the electron self-energy correction, $\Sigma_\alpha(0) - V_{\mathrm{DC},\alpha}$, there are several options for the double counting potential $V_{\mathrm{DC},\alpha}$ [96]. One such option is to set $V_{\mathrm{DC},\alpha} = \Sigma_\alpha(0)$, which leaves the LDA FS intact. Another option is to compute the crystal-field modifications self-consistently using an average over orbital self-energies, $V_{DC,\alpha} = \frac{1}{N}\sum_\alpha^N \Sigma_\alpha(0)$.

For the $CeTX_3$ compounds, the crystalline electric field (CEF) effect of the tetragonal symmetry lifts the degeneracy of the J=5/2 total angular momentum state, splitting it into three doublets. Magnetic susceptibility and inelastic neutron scattering experiments [101,

102, 103, 104] have determined the ground state doublet to be $\Gamma_7^{(1)}$ with Γ_6 and $\Gamma_7^{(2)}$ slightly higher in energy. Our LDA calculation shows that the lowest energy doublet hybridizes with the four bands crossing the Fermi energy (E_F), which are largely responsible for the shape of the FS. This is consistent with prior works that show qualitative agreement between the LDA FS and experimental de Haas-van Alphen measurements for $CeRhSi_3$ [94]. In order to best match the experimentally determined Fermi surfaces and mass enhancements we take a phenomenological approach, selecting a hybrid double counting scheme which independently treats the lowest energy doublets while the remaining states are shifted upward by 0.1Ry. In Appendix B, we show that a different choice of shift parameter does not affect the states near the Fermi energy, and does not change the conclusions of our work. An analogous energy shift was used to find the FS of the isostructural $LaTX_3$, which is presumed to be very similar to that of the respective $CeTX_3$ compounds since their Ce-4f electrons are highly localized [105, 106].

Our LDA+G procedure yields band-dependent quasiparticle residues z_α, which are summarized in Table 3.3. It is worth noting that the $\Gamma_7^{(2)}$ doublet has been determined to be the lowest lying state in $CeRhSi_3$ [106]. However, our calculations place the $\Gamma_7^{(1)}$ doublet at the lowest energy for all six isoelectronic compounds.

The trends in the $CeTX_3$ series can be understood in terms of a Doniach phase diagram

Table 3.3: Quasiparticle residues z_α for the lowest energy states for the members of the $CeTX_3$ series.

	$z_{\mathrm{LDA+G}}$ (U=5 eV)			$z_{\mathrm{LDA+G}}$ (U=6 eV)		
	$\Gamma_7^{(1)}$	Γ_6	$\Gamma_7^{(2)}$	$\Gamma_7^{(1)}$	Γ_6	$\Gamma_7^{(2)}$
$CeCoSi_3$	0.59	0.57	0.87	0.54	0.52	0.82
$CeRhSi_3$	0.43	0.41	0.86	0.37	0.36	0.81
$CeIrSi_3$	0.43	0.42	0.86	0.38	0.36	0.81
$CeCoGe_3$	0.38	0.36	0.85	0.33	0.32	0.78
$CeRhGe_3$	0.16	0.14	0.92	0.12	0.10	0.89
$CeIrGe_3$	0.15	0.14	0.93	0.11	0.09	0.91

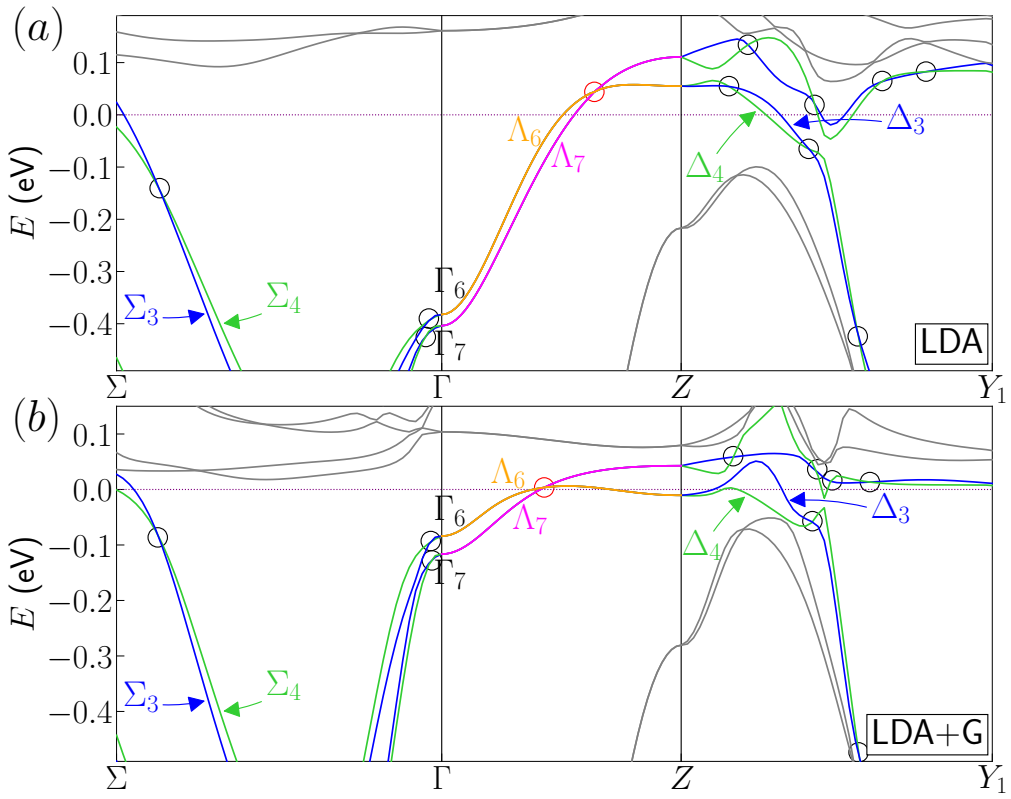

Figure 3.4: Band structures for $CeCoGe_3$ using (a) LDA, and (b) LDA+G. Bands are labeled with their character representations according to their mirror eigenvalue: Σ_3/Δ_3 (blue) for $-i$ and Σ_4/Δ_4 (green) for i within the mirror planes. Along the $\Gamma - Z$ line, doublets Λ_6 (orange) and Λ_7 (magenta) form a DP. NL crossings and DPs are indicated by black and red circles respectively.

arising from competing RKKY and Kondo interactions [107]. The tuning parameter in the Doniach phase diagram is $|J_{cf}|N(0)$ where J_{cf} is the magnetic exchange interaction and $N(0)$ is the density of states at the E_F. Experimentally, this parameter can be tuned by compressing the lattice using pressure, resulting in a greater hybridization of the conduction and Ce-4f bands, thus decreasing the localization of the electrons. This is reflected directly in the trend of Néel temperatures, with $CeTGe_3$ compounds exceeding their Si counterparts, (T_N = 21K, 14.6K, 8.7K vs. 0K, 1.8K, 5.0K for T = Co, Rh, Ir), due to their larger lattice constants [91]. The Néel temperatures of $CeRhSi_3$ and $CeIrSi_3$ are suppressed to zero at relatively low pressures $P_c \sim 2$ GPa, indicating their proximity to a quantum critical point.

The computed z_α values follow a decreasing trend with increasing lattice volumes, and

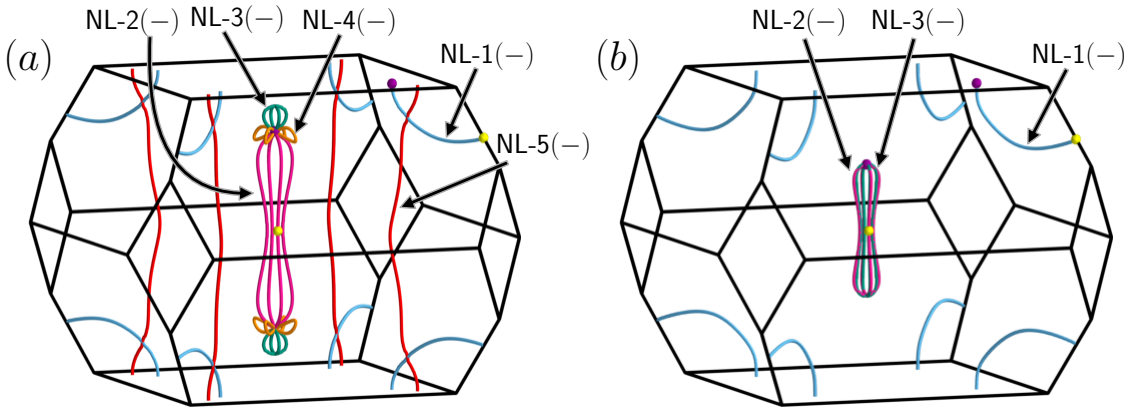

Figure 3.5: Selected NLs in $CeCoGe_3$ for LDA (a), and LDA+G (b), with colored spheres showing start (yellow)/end (purple) points for NLs plotted in Fig. 3.6.

qualitatively match the experimental trend of larger quasiparticle masses as the mass of the transition metal atom increases. These imply a factor of $\sim$2−9-fold increase in Sommerfield γ values, but experimental measurements on $CeTX_3$ compounds in the high pressure paramagnetic state are not presently available for comparison.

The bands crossing E_F are predominantly Ce-4f in character, with a minor contribution from the transition metal d-orbitals away from the Fermi level. When Coulomb interactions are considered through the LDA+G calculation described above, their bandwidth is narrowed and the Fermi level is pinned to the lower doublet due to the increased density of states (Figure 3.4), changing the electronic structure and associated topological features near E_F. We emphasize that while the particular number and shape of the topological features depend on the choice of double counting potential and magnitude of Hubbard-U, their existence is guaranteed by symmetry and robust to correlations. Since the $CeTX_3$ compounds are isoelectronic, the general picture of their topological properties is the same, with each compound hosting different sets of particular features based on the relative band positions determined by the CEF splitting. For the remainder of this work we will focus on describing the electronic properties of $CeCoGe_3$, which hosts representative members of each type of topological features found in the series, including Dirac points (DPs) [15, 108, 109, 110, 111, 112], Weyl points (WPs) [21, 113, 114, 69], and nodal lines (NLs)

[20, 25, 115, 26].

To locate and confirm the topological features, we use a one shot method for data mining the bands [35]. We divide the BZ into an initial $20 \times 20 \times 20$ **k**-grid, computing the integral of Berry curvature fluxes through the surface of each k-cube to find sources and sinks. The locations of these topological points are recursively refined by repeating the procedure on a $4 \times 4 \times 4$ grid within their **k**-cube until the desired precision is achieved, thus resolving much finer details of the material topology.

We find two classes of WPs in $CeCoGe_3$. The first appears in sets of eight confined to the $k_z = 0$ plane, while the second comes in sets of 16 which are additionally separated in the k_z direction. Table 3.4 shows selected WPs of $CeCoGe_3$ listed along with their presumptive counterparts in LDA+G, which are shifted slightly in momentum space due to band renormalization. In total, $CeCoGe_3$ has seven (eight) non-equivalent Weyl points in LDA (LDA+G); additional details can be found in Appendix B.

The most striking topological structure in the BZ is the set of nodal lines emerging from the Dirac point in this material. The band inversion mechanism generating the DP along the $\Gamma - Z$ axis is similar to that responsible for the DP in the inversion broken Cd_3As_2 [109], which shares the C_{4v} point group symmetry. Along the $\Gamma - Z$ direction, compatibility relations for the double group connect $\Gamma_7 \to \Lambda_7$ and $\Gamma_6 \to \Lambda_6$. When moving along $\Gamma - Z$, the lowest lying Λ_7 Kramer's doublet switches with the Λ_6 doublet. The DP formed by the

Table 3.4: Non-equivalent WPs of $CeCoGe_3$, with columns: topological charge (C), number of symmetry equivalent WP in this set (#), location ($\mathbf{k}_{\text{Weyl}}$) given in units of $(2\pi/a, 2\pi/a, 2\pi/c)$, and energy in meV (E). The Fermi energy is set to 0 eV.

$CeCoGe_3$		LDA		LDA+G	
C	#	$\mathbf{k}_{\text{Weyl}}$	E	$\mathbf{k}_{\text{Weyl}}$	E
+1	8	(0.097, 0.187, 1.000)	-109	(0.161, 0.133 , 1.000)	-49
−1	16	(0.118, 0.152, 0.556)	-140	(0.131, 0.168 , 0.586)	-110
+1	16	(0.235, 0.271, 0.676)	+78	(0.167, 0.236 , 0.530)	+33
−1	16	(0.057, 0.285, 0.996)	+118	(0.083, 0.221 , 0.617)	+37

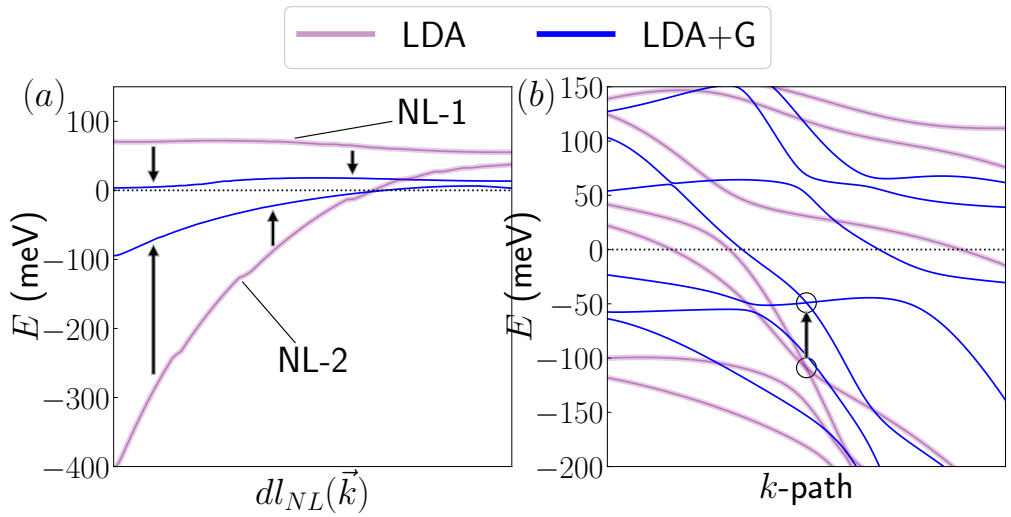

Figure 3.6: Renormalization of topological features in $CeCoGe_3$ between LDA (violet) and LDA+G (blue). (a) Renormalization of NL-1 and NL-2. Energy is plotted along the length of each NL (normalized to unity), with start/end points as shown in Fig 3.5. (b) Plots of bands around the first WP from Table 3.4. k-path is the straight line connecting $\mathbf{k}_{\text{Weyl}} \pm 0.1\hat{k}_y$.

two doublets persists with the inclusion of band renormalizations, shifting from a position $k_z = 0.644\frac{2\pi}{c}$ in LDA to $k_z = 0.4285\frac{2\pi}{c}$ in LDA+G, closer to the Γ point, as shown in Figure 3.4.

Moving away from the $\Gamma - Z$ axis within the σ_v (σ_d) mirror plane, compatibility relations dictate that the Λ_6 and Λ_7 doublets split into bands with Σ_3/Σ_4 (Δ_3/Δ_4) irreducible representation. They can be distinguished by their mirror eigenvalue, with $-i$ corresponding to Σ_3/Δ_3 and $+i$ to Σ_4/Δ_4. Intersecting bands belonging to different mirror plane irreducible representations form a topologically protected continuous line of degeneracy called a Weyl nodal line [22]. Such NLs are protected by mirror symmetry, and are robust against perturbations. Verification of NL topology is further discussed in Appendix B.

A selection of NLs in $CeCoGe_3$ are shown in Figure 3.5. In LDA, three NLs emerge from the DP, with NL-2 and NL-3 forming loops within the σ_v plane and NL-4 forming a loop in the σ_d planes. The two other NLs within the σ_d plane, NL-1 and NL-5, do not form loops, instead connecting across the edge of the BZ. When correlations are considered, the

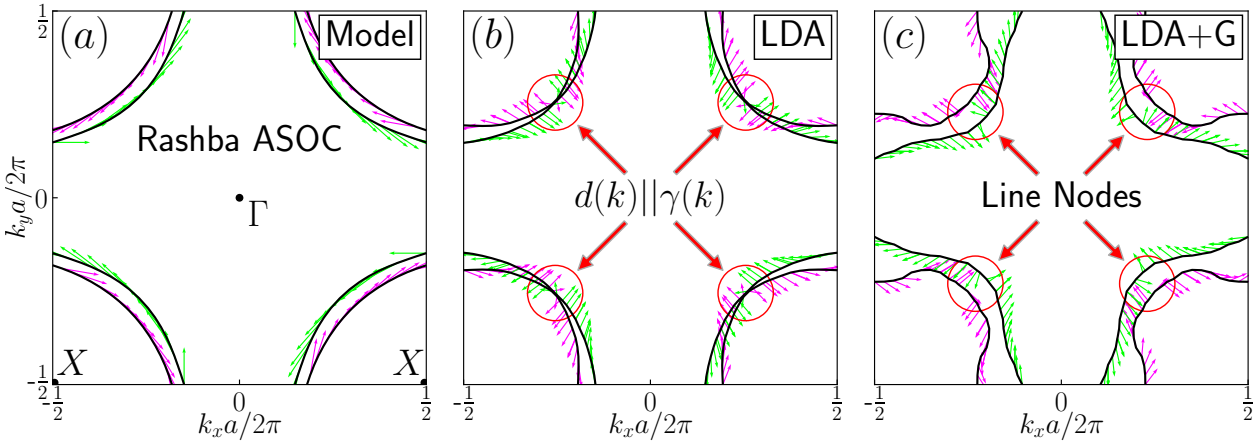

Figure 3.7: Plots of the FS of $CeCoGe_3$ within the $k_z = 0$ plane for (a) the TB model, (b) LDA and (c) LDA+G. Green (magenta) arrows show the direction of spins projected into the $xy-$plane for the upper (lower) band at each point. For LDA+G the energy is shifted by -5meV to avoid FS distortion due to pockets created by a set of Type-II Weyl points located just above E_f. Red circles highlight the spin distortion caused by the NLs in the normal state, which indicates the existence of zeros in $\boldsymbol{\gamma}(\mathbf{k})$ and implies line nodes in the SC gap function.

NL structure of $CeCoGe_3$ changes dramatically. NL-3 mixes with other NLs (not pictured), inverting to connect across the $k_z = 0$ plane, nearly coinciding with NL-2, while NL-4 and NL-5 are destroyed by correlations. On the other hand, the momentum-space structures of NL-1 and NL-2 do not change much in LDA+G. We note that since NL-3 and NL-4 are very small features and are strongly affected by correlations, it is unlikely that they can be resolved experimentally. Appendix B contains the details of several additional NLs which lie farther from E_F, for a total of 15 (12) NLs in LDA (LDA+G).

As we have mentioned previously, the renormalization of quasiparticle bands by correlations affects not only the momentum-space position of topological features, but also the energy at which they are located. Coulomb interactions substantially reduce the width of the Ce-4f bands and pin them to the Fermi energy due to the increased density of states. A consequence of this renormalization is that any topological features formed by the Ce-4f bands move closer to the E_F, becoming more relevant for the SC physics.

We illustrate this by showing the renormalization of the first WP in Table 3.4 as well

as NL-1 and NL-2 (Figure 3.6). Since the two NLs are formed from bands with a large Ce-4f component, the renormalization of these bands by correlations has a twofold effect, narrowing the energy dispersion of the NLs and move them closer to the E_F. Likewise, the Weyl point located at $(0.09700\frac{2\pi}{a}, 0.18704\frac{2\pi}{a}, 1.0\frac{2\pi}{c})$ is formed from bands that have primarily Ce-4f character near this momentum. The correlations introduced by LDA+G raise the energy by 60 meV, and shift the Weyl point to a new momentum space position $(0.16138\frac{2\pi}{a}, 0.13255\frac{2\pi}{a}, 1.0\frac{2\pi}{c})$.

While SC in the $CeTX_3$ compounds has been studied extensively, the nature of the pairing state has not been settled. There are a number of good reviews on superconductivity in non-centrosymmetric materials [116, 117, 118, 119], which we will briefly outline here. The absence of inversion symmetry allows for an ASOC term,

$$H_{\text{ASOC}} = \sum_{\mathbf{k}} \sum_{\alpha\beta=\uparrow,\downarrow} \boldsymbol{\gamma}(\mathbf{k}) \cdot \tilde{\boldsymbol{\sigma}}_{\alpha\beta} c^{\dagger}_{\mathbf{k}\alpha} c_{\mathbf{k}\beta}, \tag{3.10}$$

where the Pauli matrices $\tilde{\boldsymbol{\sigma}} = (\tilde{\sigma}_x, \tilde{\sigma}_y, \tilde{\sigma}_z)$ act on the pseudospin basis states $|\mathbf{k}, \uparrow\rangle$ and $|\mathbf{k}, \downarrow\rangle$, and $c^{\dagger}_{\mathbf{k}\alpha}(c_{\mathbf{k}\beta})$ are the corresponding creation (annihilation) operators.

The form of $\boldsymbol{\gamma}(\mathbf{k})$ explicitly determines the local spin structure in $\mathbf{k}$-space. This places a constraint on the superconducting gap function $\Delta(k)$, which in general can be expanded in the basis of Pauli matrices as $\Delta(k) = [\psi(\mathbf{k}) + \mathbf{d}(\mathbf{k}) \cdot \tilde{\boldsymbol{\sigma}}] i\tilde{\sigma}_y$, with even-parity scalar $\psi(k)$ (singlet) and odd-parity vector $\mathbf{d}(\mathbf{k})$ (triplet) components. For sufficiently strong ASOC, $|\pm\mathbf{k}, \uparrow\rangle$ states become non-degenerate, which suppresses the component of $\mathbf{d}(\mathbf{k})$ that is not parallel to $\boldsymbol{\gamma}(\mathbf{k})$ [116, 117, 120, 121]. It then follows that the triplet component of the gap $\mathbf{d}(\mathbf{k})$ can be infered directly from the spin structure at the Fermi surface. The symmetry of the pairing gap has been studied in the context of anti-ferromagnetic spin-fluctuations near the SC transition [122, 123]. It has also been suggested that $CeRhSi_3$ and $CeIrSi_3$ may be topological Weyl superconductors [124, 125], and indeed our present study has identified a

number Weyl nodes in the energy dispersion. However, the WPs found in our calculations are Type-II, with a hyperbolic FS that does not enclose the node. Their contribution to the FS topology is quite small, and most are too far away from E_f to be relevant for the SC physics, even when taking band renormalization into account.

Instead we focus on the effect of topological NLs found in these compounds, which occupy a significantly larger phase space. Figure 3.7 shows cross sections of the $CeCoGe_3$ FS in the $k_z = 0$ plane for LDA and LDA+G, compared to a two band (TB) model (Figure 3.7a) which reproduces the principal FS features of the $CeTX_3$ family [122], showing a realignment of the spins beyond the usual Rashba-type ASOC due to the topological nodal lines near E_F. In LDA, the Type-II nodal line NL-5 passes through the k_xk_y-plane close to E_F, and its strongly tilted dispersion results in hyperboloid FS sheets around the X point in Fig 3.7b. The spins along the surface rotate by an angle π in the vicinity of the NL, creating a vortex-like defect which shrinks as the energy approaches the nodal line intersection. Exactly at the nodal line energy this vortex becomes vanishingly small, but the spin texture remains continuous due to the degeneracy of the bands. In LDA+G (Fig 3.7c), correlations shift the NL away from E_F, resulting in a gap between the Fermi surfaces, but leave the vortex-like spin defect unaffected. This spin distortion at the σ_d planes is a direct consequence of the topological nature of the NLs, making it distinct from spin structures beyond Rashba ASOC which have been considered in other works [126, 127, 128].

It has been proposed that line nodes in the superconducting gap function could arise as a result of a topological defect in $\boldsymbol{\gamma}(\mathbf{k})$, and that such a state would be dominated by spin-triplet pairing and robust to perturbation[129]. The vortex-like defects in the spin structure that arise from the topological nodal lines in the normal state of $CeTX_3$ compounds can therefore serve as a natural origin for line nodes in the superconducting gap. This result is consistent with experiments that have found evidence of gapless line-node superconductivity in $CeRhSi_3$ and $CeIrSi_3$ [130, 131, 89, 132]. Additional experiments are needed to clarify the

form of the SC gap in this family of materials.

In summary, we have performed simulations of SC compounds in the $CeTX_3$ series with LDA and LDA+G, choosing the double counting potential in such a way that reproduces the experimental Fermi surfaces. We characterized the topological properties of their energy dispersion finding WPs and NLs, which are renormalized close to the E_F by the strong Coulomb interactions of the Ce$-4f$ orbitals. These topological features in turn affect the spin-structure at the FS in these materials, which we have used to make a first-principles prediction of the superconducting gap structure.

3.5 Application to a correlated actinide system

Strongly correlated systems are known for a whole range of spectacular phenomena such as, *e.g.*, colossal magnetoresistance of manganese oxides[133], high–temperature superconductivity of cuprates[134] and iron arsenides[135] , enormous volume expansions in elemental Cerium[136] and Plutonium[137], heavy electron–mass renormalizations in compounds containing f and, sometimes, d electrons[138], *etc.* Recently, the theme of strong correlations has come into play with the notion of topology in electronic band structures, whose robust quantum states are insensitive to perturbations and are currently attracting a great interest in materials such as Topological Insulators (TIs) [1] and Weyl semimetals (WSMs)[14]. Starting from an original proposal that pyrochlore iridates, subjected to a moderate Coulomb repulsion of their *5d* electrons, should exhibit a dispersion in the vicinity of the bulk Fermi level characteristic of Weyl fermions in particle physics and the associated Fermi–arc surface states[21], the field has been enriched by the discoveries of topological Kondo insulator[139] behavior in SmB_6[140] and filled skutterudites[141], Plutonium and Americium TIs based on rocksalt structure [142], as well as heavy–fermion Weyl–Kondo semimetals [90]. These systems, representing a merge between paradigms of correlations and topology, could serve

as the basis for studying yet unknown electronic phases, transitions and functionalities, and may lead to interesting applications in the future.

Unfortunately, identifying topological properties of correlated electrons represents a challenge due to a well–known problem associated with redistribution of spectral weight driven by the interplay between Coulomb repulsion and kinetic degrees of freedom for the electrons. As a result, signatures of localized electronic states originating from atomic multiplet transitions, known as Hubbard bands, as well as strongly renormalized quasiparticle bands in the vicinity of the Fermi level, often both appear in materials with strong correlations. Such competition between localization and delocalization is at the heart of the Mott transition problem [143] which has been well understood through the development of the Dynamical Mean Field Theory (DMFT) [144]. This approach defies static mean–field approximation as, *e.g.*, implemented in Density Functional Theory (DFT) based electronic structure calculations [145]. These methods have provided a single–particle framework for computing topological indices[7, 5, 60, 38], and are currently playing a central role in identifying topological materials, using, in particular, a powerful method of high–throughput screening that allows testing hundreds or even thousands of compounds [42, 54, 55, 35]. The strongly correlated problem generally requires studying the topological character, such as Berry phases, of many–body wave functions[5, 146, 147] and has been primarily addressed on the level of many–body model Hamiltonians[148, 149, 150].

Nowadays, modern electronic structure approaches based on combinations of local density approximation (LDA)[145] and DMFT (LDA+DMFT method) [67] allow for a more accurate treatment of Coulomb correlations via computations of local self–energies $\Sigma(\omega)$ for the interacting electrons. This is achieved by treating a correlated atomic shell as an impurity hybridized with the non–interacting bath which is then periodized and subjected to self–consistency. Searches of correlated topological matter with the use of LDA+DMFT would be advantageous as they incorporate the detailed chemistry and structure of a mate-

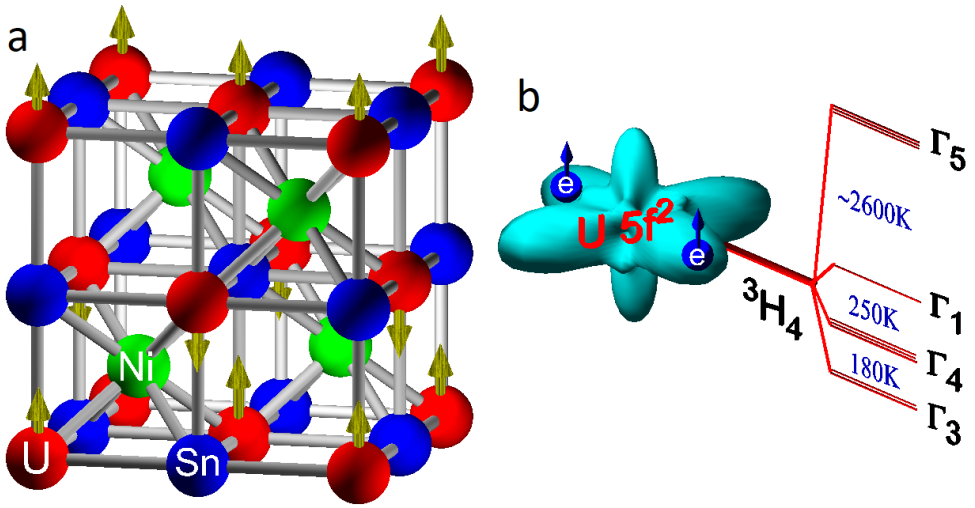

Figure 3.8: a. Crystal structure of UNiSn showing antiferromagnetic type I ordering [151], b. Effect of the cubic crystal field splitting on the $^3H_4$ ground state multiplet of the U f^2 two–electron state with its lowest non–magnetic Γ_3 doublet as found experimentally[153].

rial into the calculation. It is the purpose of this work to demonstrate how the LDA+DMFT method can be applied to uncover the rich topological behavior of actinide system UNiSn, and provide a framework for studying other compounds where genuine many–body effects need to be taken into account while searching for their topological properties.

An unusual phase transition at T_N=43K between a higher temperature paramagnetic semiconducting (PM–S) and low temperature antiferromagnetic metallic (AFM–M) phase was discovered for UNiSn long ago[151]. This actinide compound was extensively studied during last several decades owing to the unconventional (inverse) nature of this metal–insulator transition with the gap opening above T_N and the associated behavior of its strongly correlated 5f electrons. It crystallizes in a cubic structure (MgAgAs–type) (see Fig. 3.8a) and its paramagnetic semiconducting phase has an estimated energy gap of about 100 meV [152]. Its antiferromagnetic structure was found to be of type I with the ordered U moment 1.55 μ_B oriented along the (001) axis [151].

The central issue in understanding the physical properties of actinides is the degree to which their *5f* electrons are localized. Due to the absence of any signatures of heavy fermion

behavior in the specific heat data[152], the magnetic properties of UNiSn have been explained [153] on the basis of a localized $5f^2$ (U^{4+}) ionic state, whose ground state multiplet $^3H_4$ ($J = 4$) subjected to a cubic crystal field is split into a doublet (Γ_3), two triplets (Γ_4, Γ_5) and a singlet (Γ_1)[154]. Measured temperature–dependent susceptibility and magnetic entropy analysis suggested that the non–magnetic doublet is the lowest lying state 180K below the Γ_4 triplet and 430 K below the $\Gamma_1$singlet (see Fig. 3.8b). Since Γ_3 has a quadrupole moment, it was further proposed that tetragonal distortions and quadrupolar ordering exists below T_N[151]. The valence band photoemission spectra revealed a dominant 5f electron character for the states in the vicinity of the Fermi level with a contribution from U 6d, Ni 3d and Sn 6p states [155].

Previous band structure calculations of UNiSn emphasized the role of relativistic effects and electronic correlations among 5f electrons [156]. Both PM–S and AFM–M behavior have been captured correctly within the LDA+U framework[157], where on–site Coulomb correlations among f electrons are treated via the introduction of the Hubbard U term and subsequent static mean field approximation. Such a method is expected to work well in a symmetry broken AFM state, but would be invalid for the genuine two–electron Γ_3 doublet represented by a mixture of Slater determinants. One can however, assume that paramagnetism originates from the non–magnetic Γ_1 singlet, for which LDA+U should be sufficient. Within a single–particle picture this is interpreted as a doubly occupied Γ_7 level that appears when a 14 fold degenerate manifold of 5f electrons subjected to spin–orbit coupling and cubic crystal field is split into Γ_7, Γ_8 (for j=5/2) and $\Gamma_6, \Gamma_7, \Gamma_8$ (for j=7/2) sublevels. Detailed comparisons between theory and experiment revealed discrepancies in the position of the occupied f–band with respect to the Fermi energy: –0.3 eV in the photoemission vs. –1 eV in the LDA+U calculation[155].

In the present work we go beyond static mean–field approaches and utilize a modern LDA+DMFT method in order to account for the interaction effect among 5f electrons more

accurately. As our main result, we uncover that the two well–known phases of actinide compound UNiSn, correspond to Topological Insulator (TI) and Weyl semimetal (WSM) phases of topological quantum matter. Thus, the unconventional insulator–metal transition observed in UNiSn is also a TI–to–WSM transition. The ability to trigger changes in topological phases by varying temperature is interesting both fundamentally and from the point of view of applications, since metal–insulator transitions are very attractive in general for making all kinds of electrical and thermal conductivity switches or optical modulators. Using the magic of highly conductive coating in terms of disorder tolerant surface states that exist in TIs and WSMs, can provide additional control in those applications, as for example, Weyl semimetals thin films or nanostructures exhibiting ultra–high conductivities[32, 158]. Other functionalities could take advantage of very different responses to an applied magnetic field relevant for magnetotransport or differences between spin textures of the Dirac cone or Fermi arc states that could allow a temperature control of current–induced surface spin polarization relevant for spintronics[159, 160].

An improved treatment of Coulomb interactions in UNiSn should include a frequency–dependent self–energy $\Sigma_f(\omega)$ within the spin–orbit coupled space of the 5f electrons (dimension 14) which is incorporated into the single–particle LDA Hamiltonian describing all other (weakly correlated) states. A family of approaches that allow such a combination of the self–energy with LDA (the SELDA family) has been developed with help of projector operators long ago[161]. The LDA+DMFT method [67] delivers $\Sigma_f(\omega)$ by iteratively solving an auxiliary Anderson impurity model (AIM) that considers hybridization between 5f states and other non–interacting electrons as a self–consistent function that changes during the DMFT iterations. The charge density self–consistency is subsequently utilized in a manner prescribed by DFT. The exact solution of AIM is possible in principle via a recently developed Continuous Time Quantum Monte Carlo (CT–QMC) method [162], although accounting for the full Hilbert space of interacting f electrons together with spin–orbit and crystal field terms represents a challenge. In addition, the CT–QMC works on the imaginary

time–frequency axis and obtaining the frequency dependence of the self–energy on the real axis involves an analytical continuation algorithm which is known to be not very accurate.

In order to study the topology of correlated electrons in UNiSn here we take a pragmatic approach and make the DMFT impurity problem numerically tractable by using the experimental fact that the Uranium f electrons are localized in their $5f^2$ Γ_3 ground state, from which the one–electron multiplet transitions can be obtained by exact diagonalization. The corresponding f–electron self–energies are subsequently expanded in the Laurent series which allows us to replace the non–linear (in energy) Dyson equation by a linear Schroedinger–like equation in an extended subset of "pole states" [163] (see Appendix for details). Remarkably, the pole representation for the self–energy results in the appearance of many–body satellites and multiplets in the spectra as effective band states, in general carrying a fractional occupancy due to the spectral weight transfer. It is ideally suited for studying topological indices, as the corresponding auxiliary wave functions representing the many–body features, carry all the necessary information about the Berry phase of the interacting electrons[164].

For UNiSn, we carry out all calculations by treating the f–electrons in their $5f^2$ Γ_3 ground state. The Coulomb interaction matrix elements needed for the exact diagonalization procedure ($F^{(0)}, F^{(2)}, F^{(4)}, F^{(6)}$ Slater integrals) have been found from the atomic 5f–electron wave functions and scaled to account for screening effects. We cover a range of these parameters: 2–4 eV for the Hubbard $U = F^{(0)}$ and 0–1 eV for the exchange $J = (286F^{(2)} + 195F^{(4)} + 250F^{(6)})/6435$, in order to make sure that our conclusions are not altered by the lack of an accurate procedure for determining the screening. It has been argued earlier that these values are typical for obtaining the best agreement between theory and experiment for several Uranium compounds [155, 156]. The position of the bare f–level is fixed by reproducing the experimentally observed $f^2 \rightarrow f^1$ electron removal transition at –0.3 eV [155]. The charge density self–consistency is carried out within LDA+DMFT as implemented by one us earlier[165]. For PM calculation, the spin up and spin–down

self-energies are forced to be equivalent which prevents developing a magnetic state. The AFM instability is studied by first introducing a staggered magnetic field perturbation and letting the self–consistent solution to converge. If sustainable, the spin–up and spin–down self energies become different and the solution develops magnetic moments on corresponding sites of the lattice.

We now present the results of our calculation for the paramagnetic phase of UNiSn. Fig. 3.9 shows our calculated many–body electronic spectrum in the vicinity of the Fermi level using a set of Slater integrals $F^{(0)} = 0.15, F^{(2)} = 0.3, F^{(4)} = 0.2, F^{(6)} = 0.15$ in Rydberg units. Although cast into a conventional band structure plot, we stress that the 5f electron states are treated here as true one–electron removal ($f^2 \rightarrow f^1$) and addition ($f^2 \rightarrow f^3$) processes that come from exact diagonalization, and the corresponding "energy bands" carry non–integer occupation. This can be seen by realizing that the multiplet transitions within the $j = 5/2$ manifold (shown in this Figure by red and blue) are represented by 6 energy bands that appear both below and above the Fermi level. These are the famous lower and upper Hubbard bands within the Mott gap picture that acquire a significant dispersion due to hybridization with U 6d and Sn 5p orbitals. The deduced value of the indirect energy gap shows some dependence on the Slater integrals, but falls into the same range as experiment ($\sim$100 meV [152]).

We now turn to the prediction of topological properties for the paramagnetic semiconducting phase of UNiSn. First, we point out that the underlying crystal structure is not centro–symmetric, therefore the Fu and Kane parity criterion[7] developed for insulators with both time reversal and inversion symmetries does not apply. Nevertheless, given the fact that the Uranium sites arrange themselves on an inversion symmetric face centered cubic sublattice with their odd parity localized 5f electrons lying in close proximity to the Fermi level, it is interesting to speculate whether the possibility of inversion with the even parity U 6d band is taking place. Such an f–d band inversion was at the center of recent interest

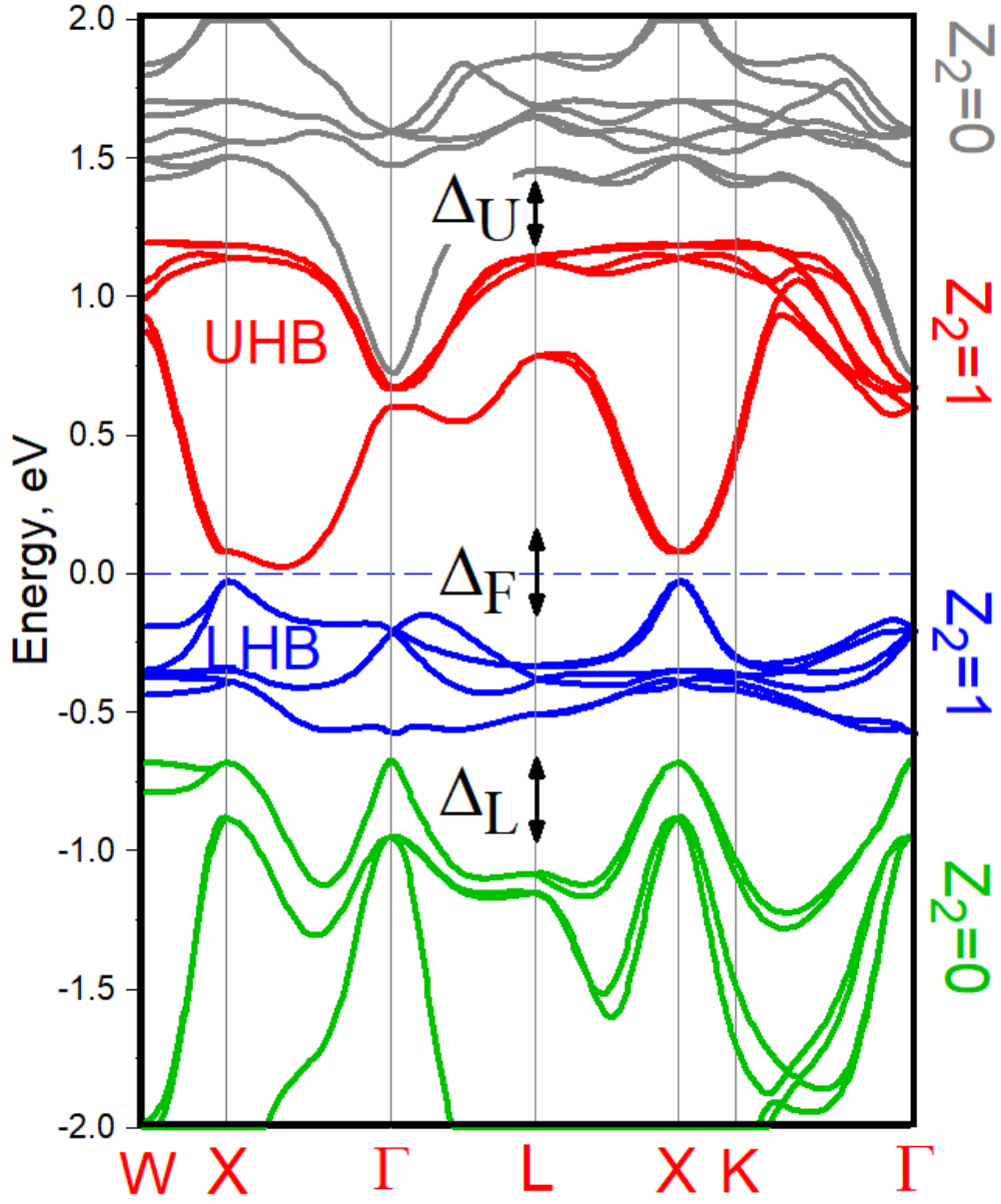

Figure 3.9: Calculated electronic structure of UNiSn using density functional theory combined with dynamical self–energies for the Uranium f–electrons assuming experimentally determined $5f^2$ Γ_3 doublet as a ground state[153], The locations of energy panels with non–zero Z_2 invariants and corresponding gaps $(\Delta_L, \Delta_F, \Delta_U)$ are indicated.

for several topological Kondo insulator materials with 4f electrons[139], as well as in some actinide systems such as AmC[142]. While the U 6d band is expected to be unoccupied, it is very wide, with its lower portion hybridized with the Hubbard bands. The Fu and Kane criterion would then imply the existence of topological Dirac cone states in UNiSn.

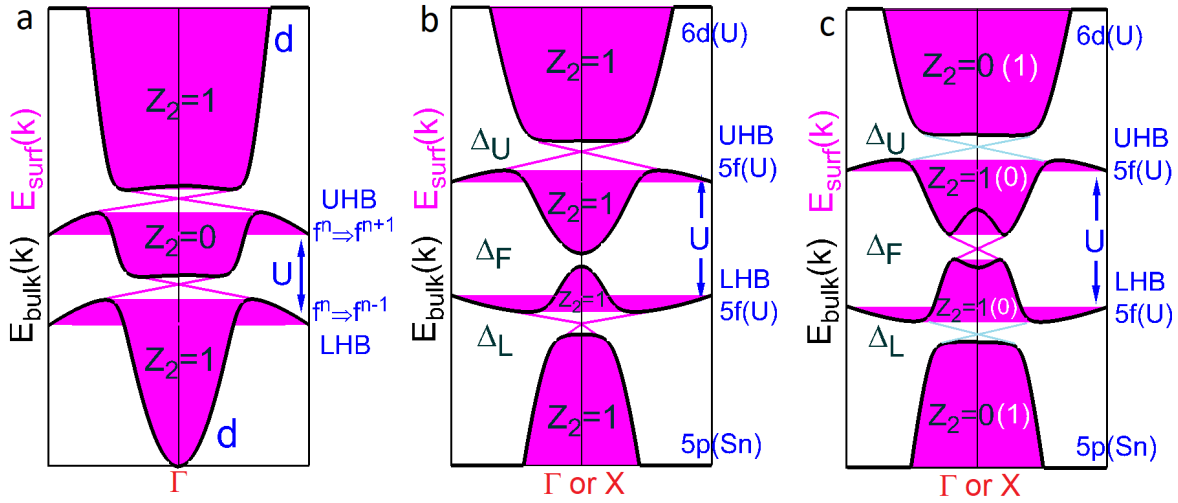

Figure 3.10: Band inversion mechanism applicable for UNiSn: a. In the periodic Anderson model, hybridization between a wide d-band centered at $\mathbf{k}$=0 Γ point and f–electron multiplet transitions (lower and upper Hubbard bands, LHB and UHB) results in three energy panels (shown by black lines) and two gaps that are both topologically non-trivial. The corresponding surface spectrum is shown by magenta color, where the spectral weight of the Dirac cone is distributed between the two gaps. b. In UNiSn, the upper Hubbard band is inverted with the wide 6d band of Uranium while the lower Hubbard band is inverted with the 5p band of Tin, resulting in four energy panels and three gaps. With two such band inversions, upper, Δ_U, and lower, Δ_L, the hybridization gaps are topological while the fundamental bulk gap, Δ_F, is not. c. The band inversion between U 6d and Sn 5p states around zone boundary X point makes the fundamental gap Δ_F topological. The topological features of the gaps Δ_U, Δ_L are seen to disappear in the LDA+DMFT calculation, but this is not a requirement within the considered model (Z_2 invariants shown in parentheses are expected).

To uncover the topological physics one needs to compute Z_2 invariants [5] for the occupied band manifold in the difficult regime of strong correlations. Fortunately, it was recently proved that utilizing a pole representation for the self–energy[163], reduces this problem to an effective non–interacting system in the extended set of pole states, whose topological indices are exactly matched [164]. We develop and carry out this computation

within the n–field approach[38] (see Appendix for details). However, some care should be taken to define an appropriate energy panel because as it is seen from our calculations that multiple gaps appear in the excitational spectrum of UNiSn (we show the panels by various colors and denote the gaps between them as $\Delta_L, \Delta_F, \Delta_U$ in Fig. 3.9). For example, the six dispersive features that represent the lower Hubbard bands (blue colored "spaghetti" in Fig. 3.9 labeled as LHB) are completely gapped from the remaining band manifold everywhere in the BZ. The same is seen for the six eigenstates representing the upper Hubbard bands above the E_F (red colored "spaghetti" in Fig. 3.9 labeled UHB). Our computations of Z_2 invariants for the four energy panels separated by $\Delta_L, \Delta_F, \Delta_U$ reveal their topological indices, which we indicate on the right margin in Fig. 3.9. The energy panels below and above the fundamental gap correspond to the indices equal to 1;(000) in the notations of Ref. [5] (we denote this result by $Z_2 = 1$ in Fig. 3.9). This proves that UNiSn is a strong topological insulator and suggests the existence of protected Dirac cone states at its surface.

To understand which orbitals are responsible for the appearance of the topological phase, we carry out calculations using a constrained hybridization approach[166]. In this method, the energies of particular orbitals are shifted by applying a constant potential constrained within the orbital space by projector operators. This is similar to the LDA+U, LDA+DMFT and other SELDA families of methods, restricting the application of the self–energy to the subspace of correlated orbitals. Utilizing this procedure, we are able to de–hybridize various states, such as U-5f, U-6d, Ni-3d, Sn-5p, etc., by shifting their energies away from the relevant energy window, and recompute Z_2 invariants. The outcome of this study is the existence of multiple band inversions in UNiSn: The upper Hubbard band is inverted with the U 6d electrons around the Γ point of the BZ, while the lower Hubbard band is inverted with Sn 5p electrons. On top of that, U 6d electrons at the very bottom of the conduction band and Sn 5p states at the very top of the valence band are also inverted around the X point of the BZ (see Fig. 3.9). These multiple band inversions are responsible for the topological insulator behavior in UNiSn.

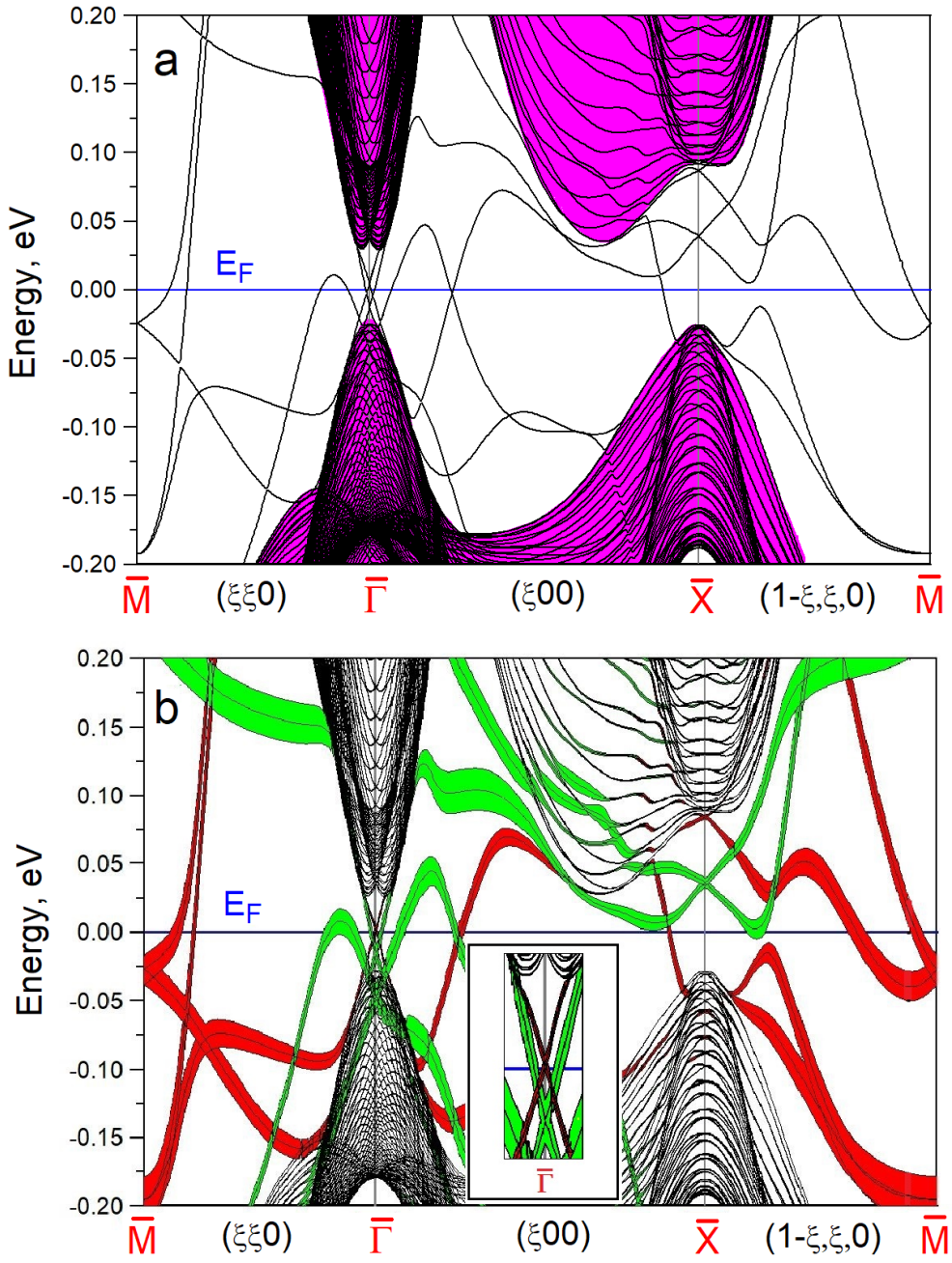

Figure 3.11: (001) surface spectrum of UNiSn calculated along high symmetry lines of the surface Brillouin Zone, $\bar{\Gamma}(000), \bar{X}(100), \bar{M}(\frac{1}{2}\frac{1}{2}0)$,using LDA+DMFT method, assuming a $5f^2$ Γ_3 doublet as a ground state. a) Projected bulk spectrum is shown by magenta. b) Top (green) and bottom (red) surface states are fattened according to the partial character of the topmost (U-Sn) and bottommost (Ni) atomic plane of the slab. Inset provides close view of the Dirac states near the $\bar{\Gamma}$ point.

To illustrate the emergent physical picture, we use the periodic Anderson model (PAM) of strong correlations. It has been recently employed for developing the concept of topological Kondo insulators where the Fermi level falls into the gap between a heavy fermion (f–like) and non–interacting (d–like) bands[139]. It has also been recently used to describe Weyl–Kondo semimetals via hybridization of a heavy–fermion state with non–interacting bands containing the nodal points[90]. In our case the f–electrons are localized and their self–energies behave similarly to the famous Hubbard I approximation: $\Sigma(\omega) = U^2/4\omega$. The solution of the PAM in this limit is schematically illustrated in Fig. 3.10a. Hybridization between a wide d–band and f–electron multiplet transitions denoted as LHB and UHB results in the appearance of two gaps in the spectrum and three energy panels (shown by black lines). Both gaps are seen to be topologically non–trivial due to the d–f band inversion mechanism. For a centrosymmetric lattice, this can be understood based on the Fu and Kane parity criterion [7]: for the lower (upper) panel, the parities of the eigenstates are odd (even) at the X and L time reversal invariant momenta (TRIM), but even (odd) at Γ. As a result, the energy gap above (below) the panel is topological. For the central panel, the parities of the eigenstates are odd everywhere, but this does not preclude having a topological gap both below and above the panel, each with its own Dirac cone (the total number of cones is even). We illustrate the corresponding surface spectrum in magenta. Note that since the Hubbard bands carry no integer occupation, the spectral weight of the Dirac cones is also re–distributed between the two gaps.

Now, in UNiSn, our constrained hybridization procedure reveals multiple band inversions around different TRIM points in the BZ: First, as illustrated in Fig. 3.10b, the upper Hubbard band is inverted with the U 6d at Γ. Due to the d–f band inversion, the topological Dirac cone is expected to appear inside the gap Δ_U at the surface spectrum. Since Uranium atoms occupy sites of the centrosymmetric face centered cubic lattice, this can be understood based on the parity criterion [7]. For the lower Hubbard band, U 5f and Sn 5p orbitals are both odd, but belong to different irreducible representations which makes it

possible to produce a strong topological insulator with a Dirac cone inside the gap Δ_L. This picture emerges when the bottom of the U 6d and the top of Sn 5p bands are not inverted around the X point, making the fundamental gap Δ_F not topological, as we show in 3.10b. Realizing the band inversion between the U 6d and Sn 5p bands at the X point (see Fig. 3.10c) results in the fundamental gap Δ_F becoming topological. Additionally, we monitor the cancellation of the topological features inside the gaps Δ_U, Δ_L. This is apparently due to a more complex overlap between various orbitals in the real calculation than the one assumed in the simplified model illustrated in Fig. 3.10c where one would in principle expect all three gaps to become topological ($Z_2 = 0$ for the LHB and UHB, and $Z_2 = 1$ for the lowermost and topmost panels as shown in brackets in Fig. 3.10c).

To shed some additional light on the nature of the topological phase, we check the one–electron spectrum for a slab that is oriented along 001 direction, and terminated at the top by U–Sn atomic plane and at the bottom by Ni plane, where we expect to see the topological boundary states originating from the two surfaces around the TRIM points of the surface BZ where the band inversion occurs. We perform a real space transformation of our LDA+DMFT Hamiltonian that is possible due to the use of a non-orthogonal tight–binding LMTO representation, which can be interpreted as the unitary transformation of the linear muffin–tin orbital basis set [167]. The slab size containing 48 original unit cells along z axis provides a completely convergent surface spectrum. Our results are plotted in Fig. 3.11, where we show both the projected bulk spectrum (Fig. 3.11a) and the top/bottom surface states that are fattened according to the partial character of the topmost (U–Sn, green) and bottommost (Ni, red) atomic plane (Fig. 3.11b). We find a clear evidence of the Dirac–cone states that appear around the $\bar{\Gamma}$ point of the surface BZ (see inset in Fig. 3.11b). Note that because we are considering 001 surface, one bulk X point is actually projected onto the surface $\bar{\Gamma}$ point, therefore the appearance of the Dirac cone around the surface $\bar{\Gamma}$ point is likely due to the band inversion around the bulk X point. We also identify Dirac cones in the immediate vicinity of the $\bar{X}$ point. However, we see that they do not span across the

gap likely due to hybridization with other surface states that appear in this energy range. Nevertheless, we can easily count that there is always an odd number of surface states that crosses the Fermi level between the time reversal invariant momenta. For example, there are 3 "green" states and 3 "red" states that cross the Fermi energy shown in Fig. 3.11b between $\bar{\Gamma}$ and $\bar{X}$. The emergent physical picture resembles the case of SmB_6 [140] where the band inversion between Sm 4f and 5d states around the bulk X point and the apparent lack of trivial surface states for the 001 surface results in Dirac cones spanning across the energy gaps around the surface $\bar{X}$ and $\bar{\Gamma}$ points.

We now turn to discussing the results of our calculation for the low temperature AFM phase of UNiSn. The origin of magnetism has been explained earlier [153] based on a molecular–field model, where owing to the second–order effect in the magnetic exchange field, the Γ_3 doublet is split into two levels with a deduced magnetic moment value of $\sim 2.6\mu_B$. Here our exact diagonalization for the 5f states is almost identical to to the static mean field solution, because the double degeneracy of Γ_3 is broken and a single Slater determinant description suffices. It has been also proven earlier that the LDA+DMFT method reduces to the LDA+U in the Hartree–Fock limit[168]. Our calculation with Slater integrals $F^{(0)} = 0.15, F^{(2)} = 0.3, F^{(4)} = 0.2, F^{(6)} = 0.15$ in Rydberg units, converges to an antiferromagnetic state with a total magnetic moment of $2.1\mu_B$ ($+3.2\mu_B$ for its orbital and $-1.1\mu_B$ for its spin counterparts) slightly larger than the experimentally deduced value of 1.55 μ_B [151]. This is in agreement with previous works [155, 156] that also pointed out the inclusion of spin fluctuations as a possible way to reduce these values. Our calculated spin density matrices resemble those obtained from the molecular–field exchange model [153].

Fig. 3.12a shows our calculated band structure along the major high symmetry directions of the BZ. A few energy bands are seen to cross the Fermi level indicating the metallic nature of the solution. Since both time reversal and inversion symmetries are now broken, it is interesting to see if there are any Weyl points in close proximity to the Fermi level.

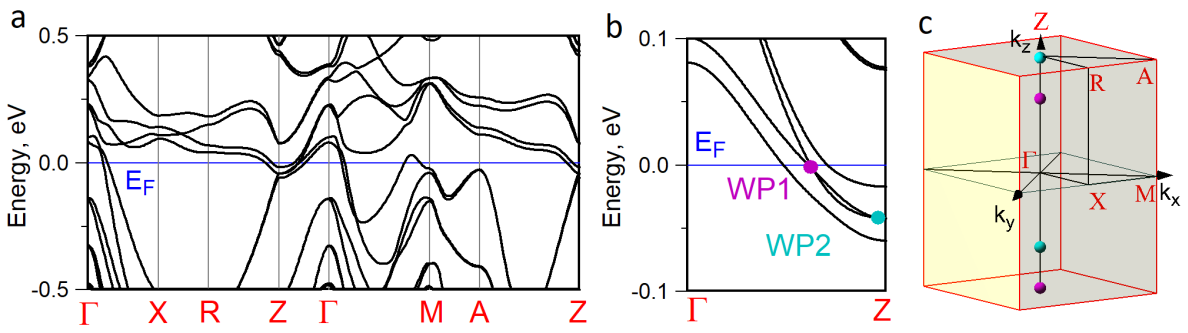

Figure 3.12: Calculations for antiferromagnetic configuration of UNiSn. a. Energy band dispersions along major high symmetry lines of the Brillouin Zone, b. Zoomed area along the ΓZ direction of the BZ showing the locations of the Weyl points with their coordinates $\mathbf{k}_{WP1} = (0, 0, 0.317)2\pi/a$ (chiral positive, energy relative to E_F is -5meV) and $\mathbf{k}_{WP2} = (0, 0, 0.492)2\pi/a$ (chiral negative, energy relative to E_F is -42 meV) c. Brillouin Zone of the AFM UNiSn with the positions of the Weyl points (magenta color refers to positive and cyan color refers to negative chiral charges).

It is well known that the Weyl point acts as a Dirac monopole in k–space and produces a non–zero Berry flux through an area surrounding it[19, 56]. We take advantage of this result and utilize a monopole mining method developed by us recently[35] in order to search for their locations. This search is rewarded by finding two Weyl points that appear exactly along the ΓZ line of the BZ, serving here as the magnetization direction. The corresponding band structure is shown in Fig. 3.12b. Despite the Weyl points aligning with ΓZ , their positions along this line were found to be sensitive to the value of Hund's rule J for 5f electrons used in the calculation, as the latter controls the shape of the bands in this energy range. The WSM phase begins to appear starting with J=0.2 eV and persists for higher values of J. Fig. 3.12c shows the positions of these Weyl points in the Brillouin Zone for J=0.3 eV. Their precise locations are given by the wave vectors $\mathbf{k}_{WP1} = (0, 0, 0.317)2\pi/a$ (chiral positive, energy relative to E_F is -5 meV) and $\mathbf{k}_{WP2} = (0, 0, 0.492)2\pi/a$ (chiral negative, energy relative to E_F is -42 meV). Unfortunately, in the absence of detailed knowledge about how the screening reduces the intra–atomic exchange interaction, these data can only serve as a guideline for possible experimental verification. Nevertheless, it should be easy to locate these Weyl points since they are expected to appear along the ΓZ line regardless of the inaccuracies

in our predictions of their coordinates. Also, it would be interesting to check the value of the longitudinal magnetoresistance whose negative sign could indicate that our predicted WSM phase and the associated chiral anomaly exists. Negative magnetoresistance has in fact been reported for this compound [169, 170] but the setup was related to measuring the (transverse) Hall coefficient.

To understand the physical origin behind magnetization induced Weyl state in UNiSn, we introduce a $k \cdot p$ model for two relativistic orbitals with an inversion breaking term.

The Hamiltonian reads

$$H_{eff} = \begin{pmatrix} A(\mathbf{k}) + \Delta_1 & 0 & Pk_z + iVk_xk_y & Pk_- + Vk_zk_+ \\ 0 & B(\mathbf{k}) - \Delta_1 & Pk_+ - Vk_zk_- & -Pk_z - iVk_xk_y \\ Pk_z - iVk_xk_y & Pk_- - Vk_zk_+ & C(\mathbf{k}) + \Delta_2 & 0 \\ Pk_+ + Vk_zk_- & -Pk_z + iVk_xk_y & 0 & D(\mathbf{k}) - \Delta_2 \end{pmatrix} \tag{3.11}$$

where $k_\pm = k_x \pm ik_y$ and diagonal elements are parametrized as follows: $A(\mathbf{k}) = A_0 + A_1\mathbf{k}^2$, $B(\mathbf{k}) = B_0 + B_1\mathbf{k}^2 - B_2\mathbf{k}^4, C(\mathbf{k}) = C_0 + C_1\mathbf{k}^2 - C_2\mathbf{k}^4, D(\mathbf{k}) = D_0 + D_1\mathbf{k}^2$ (we include quartic terms to allow multiple Weyl points to exist). The parameter P controls the inversion breaking. A similar model was previously used to describe topological insulator and Weyl semimetal phases in zincblende–like structures[52]. Here we apply a Zeeman splitting by setting the parameters $\Delta_{1,2} \neq 0$ along the magnetization (z) axis. Once the effective "spin up" and "spin down" states cross, they produce Weyl points exactly along 001 direction in the BZ while the gap between these bands is open for all other k–points. We illustrate this behavior in Fig. 3.13a which shows the dispersion of the eigenvalues of Eq. 3.11, and the existence of two Weyl points along k_z axis. The parameters of the model are the following: $A_0 = B_0 = 0.24, A_1 = B_1 = 1, B_2 = 3.376, C_0 = D_0 = -0.56, C_1 = D_1 = 0.3, C_2 = 0.3, P = 0.9, V = 0.5, \Delta_1 = 0.3, \Delta_2 = 0.6$.

One of the most striking features of Weyl semimetals is the presence of the Fermi arcs in their one–electron surface spectra [21]. Although computations of their shapes are possible via a self–consistent supercell (slab) calculation of the surface energy bands, given the variety of regular Fermi states that emerge from our AFM calculation together with the fact that the Weyl points are not exactly pinned at the Fermi level, makes it hard to resolve them in the actual surface spectrum of UNiSn. Nevertheless, since the arcs connect the Weyl points of different chirality, one can expect the existence of long arc–like features in UNiSn that should be protected from perturbations such as disorder[32].

To illustrate the shape of the Fermi arcs, we have performed the diagonalization for the k*p model that is periodized on the cubic lattice with subsequent construction of the Hamiltonian for the slab oriented perpendicular to the x axis. The results are shown in Fig. 3.13b where almost straight Fermi arcs stretched along k_z axis are seen to connect the Weyl points of opposite chirality. The parameters of the model are exactly the same as used in Fig. 3.13a. If these numbers are tweaked a little to simulate the case seen in Fig.3.12b for UNiSn so that one Weyl point sinks just below the Fermi level producing a small Weyl Fermi sphere, the portion of the arc merging with this Weyl point rotates slightly away from the k_z axis and now merges into the Fermi circle originating from the projection of the Weyl sphere to the surface BZ. At the end, we note that the limit of straight arc geometry was recently found [32] to be remarkably disorder tolerant, making it capable of producing ultra–high conductivities of WSM nanostructures [158]. The present physical picture could therefore serve as one way to engineer such arcs and make a control of topological surface transport possible.

In conclusion, based on a computational approach combining density functional theory of electronic structure and dynamical mean field theory of strong correlations, we showed that two topological phases of quantum matter, topological insulator and Weyl semimetal, accompany the unconventional insulator–metal transition in the *5f* electron compound UNiSn.

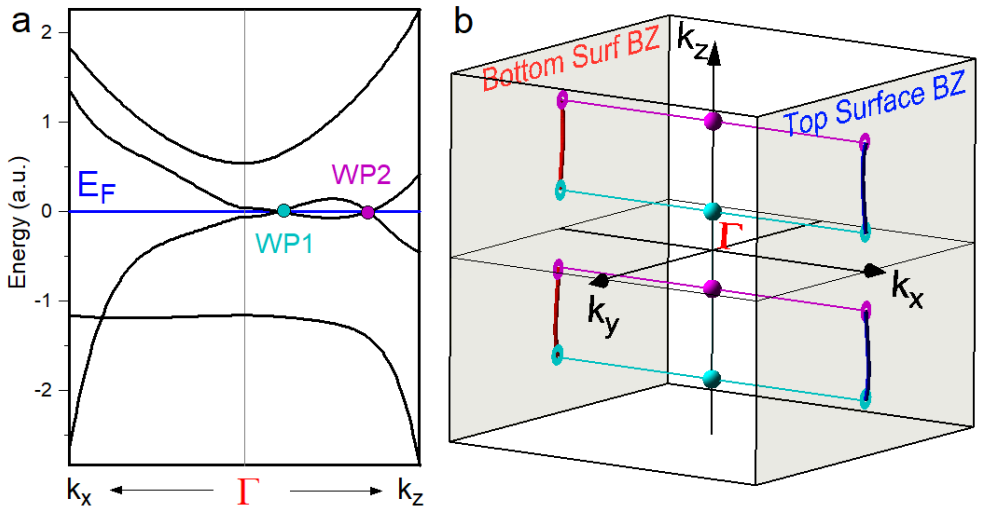

Figure 3.13: a. Dispersion of eigenstates of a 4x4 k*p model used to illustrate the magnetization induced Weyl semimetal state in UNiSn. The band structure is gapped for all k–points in the BZ except along the ΓZ line where the Weyl points are formed. b. Position of the Weyl points in the BZ of the k*p model periodized on the cubic lattice as well as shapes of the Fermi arc surface states for the slab geometry with the normal along the x axis. Magenta color refers to positive and cyan color referes to negative chiral charges.

We uncovered the physical origin of its topological insulator behavior via the occurrence of multiple band inversions between localized f–electrons and regular band states. We also concluded that the magnetic ordering triggers the Weyl state with the nodal points appearing along the magnetization direction.

Our study reveals interesting opportunities for finding other topological phase transitions in strongly correlated systems. Of particular interest are some non–centrosymmetric actinide compounds. A sister compound UPtSn is known to exhibit properties that are similar to UNiSn[152]. Another series that has been studied in the past through transport, heat capacity, neutron diffraction, and magnetic measurements is given by the Uranium compounds in an expanded half–Heusler structure [$MgCu_4Sn$–type, cF24-F43m, derived from the cubic $AuBe_5$ lattice.] Among those, UCu_4Pd is one of the most heavily investigated compounds owing to its strange dependence of the resistivity, magnetization and specific heat, which scale as $T^{1/3}$ for temperatures below 10K [171]. The quantum critical point and

non–Fermi liquid behavior of this compound is fairly well understood, but the transition between low and higher temperature phases has not fully been explained. Other famous systems to mention here are UCu_4Ni[172] and UPt_4Au[173]. Understanding the interplay between delocalized band electrons and correlated 5f–states known for their largest spin–orbit coupling is expected to provide an ideal playground for studying topological properties of interacting electrons.

Chapter 4

Anomalous Hall and Nernst Effects in Weyl Semimetals

A major consequence of the topological features found in electronic structures of materials, is that their presence is accompanied by non-trivial Berry curvature. This Berry curvature becomes important when considering the dynamics of electrons within these periodic crystals, which can be described by Bloch states [9]. In fact, a careful treatment of the semiclassical dynamics of Bloch electrons reveals that this geometric phase results in an additional term in the equations describing transport properties of topological materials [174, 175]. Analyses of this sort have been used to understand the quantum Hall effect [2], spin transport [176, 177], electric polarization [178, 179], as well as the anomalous Hall effect (AHE) [180, 56, 181, 8, 11], and anomalous Nernst effect (ANE) [182]. This chapter will derive the Berry curvature contributions to the AHE and ANE, and discuss how these transport properties can be enhanced by certain features of correlated topological materials.

The work described in this chapter was done in collaboration with Tomoya Asaba, Sean Thomas, Joe Thompson, Eric Bauer, and Filip Ronning of Los Alamos National Laboratory,

with the supervision of Sergey Savrasov. It is published in Science Advances [183].

4.1 Berry curvature contribution to AHE and ANE

When a crystal with non–vanishing Berry curvature $\boldsymbol{\Omega}_n(\boldsymbol{k})$ is placed in a weak electric and magnetic field, the semiclassical equations of motion for the Bloch electrons acquire an additional term[175, 182]

$$\begin{aligned}\dot{\boldsymbol{r}} &= \frac{1}{\hbar}\frac{\partial \epsilon_n(\boldsymbol{k})}{\partial \boldsymbol{k}} - \dot{\boldsymbol{k}} \times \boldsymbol{\Omega}_n(\boldsymbol{k}) \\ \hbar\dot{\boldsymbol{k}} &= -e\boldsymbol{E}(\boldsymbol{r}) - e\dot{\boldsymbol{r}} \times \boldsymbol{B}(\boldsymbol{r}).\end{aligned} \tag{4.1}$$

Here, the Berry curvature $\boldsymbol{\Omega}_n(\boldsymbol{k})$ can be written as the curl of the Berry connection $\boldsymbol{\Omega}_n(\boldsymbol{k}) = \boldsymbol{\nabla}_{\boldsymbol{k}} \times \langle u_n(\boldsymbol{k})|i\boldsymbol{\nabla}_{\boldsymbol{k}}|u_n(\boldsymbol{k})\rangle$ where $|u_n(\boldsymbol{k})\rangle$ is the periodic part of the Bloch wave-function $|\psi(\boldsymbol{k})\rangle = e^{i\boldsymbol{k}\cdot\boldsymbol{r}}|u_n(\boldsymbol{k})\rangle$. The most straightforward way to proceed is to determine how the evolution of the state variables $(\boldsymbol{r}, \boldsymbol{k})$ over time actually results in a change in the phase-space volume of the system $\Delta V = \Delta\boldsymbol{r}\Delta\boldsymbol{k}$. This in turn leads to a modified density of states in phase space, resulting in computed observables acquiring an additional term due to the non-zero Berry curvature.

Inserting the equations (4.1) for the time evolution of the state variables into the expression for the time evolution of the phase space volume $(1/\Delta V)d\Delta V/dt = \boldsymbol{\nabla}_{\boldsymbol{r}}\cdot\dot{\boldsymbol{r}} + \boldsymbol{\nabla}_{\boldsymbol{k}}\cdot\dot{\boldsymbol{k}}$, we find

$$\frac{1}{\Delta V}\frac{d}{dt}\Delta V = \boldsymbol{\nabla}_{\boldsymbol{r}} \cdot \dot{\boldsymbol{r}} + \boldsymbol{\nabla}_{\boldsymbol{k}} \cdot \dot{\boldsymbol{k}} = -\frac{d}{dt}\ln(1 + e\boldsymbol{B}\cdot\boldsymbol{\Omega}/\hbar). \tag{4.2}$$

Assuming an initial volume element ΔV_0 at $t = 0$, this can be solved to find the evolution of the volume element

$$\Delta V = \frac{\Delta V_0}{1 + e\boldsymbol{B} \cdot \boldsymbol{\Omega}/\hbar} \tag{4.3}$$

which becomes time-dependent as the state variables $(\boldsymbol{r}, \boldsymbol{k})$ change, since the magnetic field can vary spatially, and the Berry curvature is generally $\boldsymbol{k}$-dependent.

The number of states per volume element $D(\boldsymbol{r}, \boldsymbol{k})\Delta V$ should remain constant as the system evolves. To satisfy this constraint in three dimensions, the density of states is modified to be

$$D(\boldsymbol{r}, \boldsymbol{k}) = (2\pi)^{-3}(1 + e\boldsymbol{B} \cdot \boldsymbol{\Omega}/\hbar), \tag{4.4}$$

which can be integrated over the occupied states set by the Fermi-Dirac distribution $f(\boldsymbol{k})$ to yield the electron density

$$n_e = \int d\boldsymbol{k} f(\boldsymbol{k}) D(\boldsymbol{r}, \boldsymbol{k}) = \int \frac{d\boldsymbol{k}}{(2\pi)^3} f(\boldsymbol{k})(1 + e\boldsymbol{B} \cdot \boldsymbol{\Omega}/\hbar). \tag{4.5}$$

By taking the derivative of the electron density with respect to the $\boldsymbol{B}$-field, we can obtain the Hall conductivity [184]: $\sigma_{xy} = -e(\partial n_e/\partial B_z)_\mu$. This relationship can be understood by considering a region of a metal slab exposed to a time-dependent magnetic field. The changing flux generates electromotive force at the boundary of this region, resulting in a Hall current which in turn changes the electron density inside this region. Evaluating this derivative we recover

$$\sigma_{xy} = -\frac{e^2}{\hbar} \int \frac{d\boldsymbol{k}}{(2\pi)^3} f(\boldsymbol{k}) \Omega_z(\boldsymbol{k}), \tag{4.6}$$

the well-known result for the intrinsic anomalous Hall effect.

To derive an analogous expression for the intrinsic anomalous Nernst effect, we need to compute the Berry curvature-dependent contribution to the magnetization $\boldsymbol{M}(\boldsymbol{r})$. The current contribution arising from the magnetization must be subtracted from the current density $\boldsymbol{J}$ to obtain the true transport current $\boldsymbol{j} = \boldsymbol{J} - \boldsymbol{\nabla} \times \boldsymbol{M}(\boldsymbol{r})$ measured by experiments [182]. Starting from the grand canonical potential, we use the modified density of states we derived previously to obtain

$$F = -\frac{1}{\beta}\int d\boldsymbol{k} D(\boldsymbol{r},\boldsymbol{k}) \ln\bigl(1+e^{-\beta(\epsilon_M-\mu)}\bigr) = -\frac{1}{\beta}\int \frac{d\boldsymbol{k}}{(2\pi)^3}(1+e\boldsymbol{B}\cdot\boldsymbol{\Omega}/\hbar)\ln\bigl(1+e^{-\beta(\epsilon_M-\mu)}\bigr), \tag{4.7}$$

where $\beta = 1/k_B T$ and the energy $\epsilon_M = \epsilon(\boldsymbol{k}) - \boldsymbol{m}(\boldsymbol{k})\cdot\boldsymbol{B}$ is found by subtracting the perturbation arising due to the orbital magnetic moment $\boldsymbol{m}(\boldsymbol{k})$ from the original dispersion of the material. Taking the derivative with respect to magnetic field $\boldsymbol{B}$, we obtain the magnetization

$$\boldsymbol{M}(\boldsymbol{r}) = \int \frac{d\boldsymbol{k}}{(2\pi)^3} f(\boldsymbol{k})\boldsymbol{m}(\boldsymbol{k}) + \int \frac{d\boldsymbol{k}}{(2\pi)^3}\frac{e}{\beta\hbar}\boldsymbol{\Omega}(\boldsymbol{k})\ln\bigl(1+e^{-\beta(\epsilon-\mu)}\bigr). \tag{4.8}$$

The second term in $\boldsymbol{M}(\boldsymbol{r})$ is in fact the intrinsic contribution due to the non-zero Berry curvature. Thus we find the intrinsic Berry curvature correction to the transport current stemming from the magnetization

$$\boldsymbol{j}_{\text{in}} = -\boldsymbol{\nabla}\times\frac{1}{\beta}\int \frac{d\boldsymbol{k}}{(2\pi)^3}\frac{e}{\hbar}\boldsymbol{\Omega}(\boldsymbol{k})\ln\bigl(1+e^{-\beta(\epsilon-\mu)}\bigr). \tag{4.9}$$

In the particular case of a temperature gradient driving this transport current, we can

find:

$$\begin{aligned}\boldsymbol{j}_{\text{in},\nabla T} &= -\boldsymbol{\nabla} T \times \frac{d}{dT}\frac{1}{\beta}\int \frac{d\boldsymbol{k}}{(2\pi)^3}\frac{e}{\hbar}\boldsymbol{\Omega}(\boldsymbol{k})\ln\left(1+e^{-\beta(\epsilon-\mu)}\right) \\ &= -\boldsymbol{\nabla} T \times \frac{e}{\hbar}\int \frac{d\boldsymbol{k}}{(2\pi)^3}\boldsymbol{\Omega}(\boldsymbol{k})\left[k_B \ln\left(1+e^{-\beta(\epsilon-\mu)}\right) + \frac{\epsilon-\mu}{T}\frac{1}{1+e^{\beta(\epsilon-\mu)}}\right] \end{aligned} \tag{4.10}$$

Since the anomalous Nernst conductivity α_{xy} is defined as $j_x = \alpha_{xy}(-\nabla_y T)$, the result can be read off from the above expression:

$$\alpha_{xy} = \frac{e}{T\hbar}\int \frac{d\boldsymbol{k}}{(2\pi)^3}\Omega_z(\boldsymbol{k})\left[k_B T \ln\left(1+e^{-\beta(\epsilon-\mu)}\right) + (\epsilon-\mu)f(\boldsymbol{k})\right] \tag{4.11}$$

which we can further simplify using integration by parts [182] to

$$\alpha_{xy} = -\frac{1}{e}\int d\epsilon \frac{\partial f_n(\boldsymbol{k})}{\partial \mu}\sigma_{xy}(\epsilon)\frac{\epsilon-\mu}{T} \tag{4.12}$$

where $\sigma_{xy}(\epsilon)$ is the $T \to 0$ limit of Eq. 4.6:

$$\sigma_{xy}(\epsilon) = -\frac{e^2}{\hbar}\int \frac{d\boldsymbol{k}}{(2\pi)^3}\theta(\epsilon-\epsilon_{\boldsymbol{k}})\Omega_z(\boldsymbol{k}) \tag{4.13}$$

At low temperatures the anomalous Nernst conductivity is directly proportional to the derivative of the anomalous Hall conductivity with respect to energy. This relation is known as the Mott relation and has been shown to hold for both ferromagnets and non-magnetic materials [185, 186, 182]:

$$\alpha_{xy} = \frac{\pi^2}{3}\frac{k_B^2 T}{e}\sigma'_{xy}(\epsilon_F). \tag{4.14}$$

The origin of this relationship can be seen from the previous result in Eq. 4.12. The integral can be interpreted as a convolution with the weight function $w(\epsilon, T) = \frac{\epsilon-\mu}{T}\frac{\partial f_n(\boldsymbol{k})}{\partial \mu}$. The weight

function $w(\epsilon, T)$ looks approximately like the derivative of a gaussian, and thus approaches $\delta'(\epsilon)$ for low temperatures. Integrating a function over $\delta'(\epsilon)$ will yield its derivative, which gives the expected relationship $\alpha_{xy} \propto \sigma'_{xy}$.

4.2 Enhanced transport for critically tilted Weyl points

While the presence of Weyl points in a magnetic material necessarily generates a Berry curvature which leads to intrinsic anomalous Hall and Nernst effects, there are particular situations where these transport properties are especially enhanced. One such situation occurs when a pair of tilted Weyl points lies close to the critical transition between Type-I and Type-II. Near such such a Lifshitz transition, a logarithmic divergence in the slope of α_{xy} can result in the significant amplification of α_{xy} [187]

We can illustrate this effect by considering an effective model that takes the tilt into account [188]:

$$\begin{aligned} H(\boldsymbol{k})_+ &= +\hbar C(k_z - Q) - \hbar v \boldsymbol{\sigma} \cdot (\boldsymbol{k} - Q\hat{k}_z) \\ H(\boldsymbol{k})_- &= -\hbar C(k_z + Q) + \hbar v \boldsymbol{\sigma} \cdot (\boldsymbol{k} + Q\hat{k}_z). \end{aligned} \tag{4.15}$$

This model describes two Weyl points with chirality ± 1 separated by a distance $2Q$ in momentum space along the $\hat{k}_z$ direction. In this sign convection, positive v describes a negatively charged Weyl point at $k = Q$, and a positive Weyl point at $k = -Q$. Changing the sign of v interchanges the two Weyl points. The parameter C controls the tilting of the Weyl cones, with positive C describing a tilting of the Weyl cones *inward* towards $k_z = 0$, and negative C corresponding to both cones tilting *outward*, away from $k_z = 0$: In the Figure 4.1, the dashed lines denote untilted Type-I cones (second terms in equation 4.15). Taking the C-dependent terms into account tilts the Weyl cones. By increasing C until it

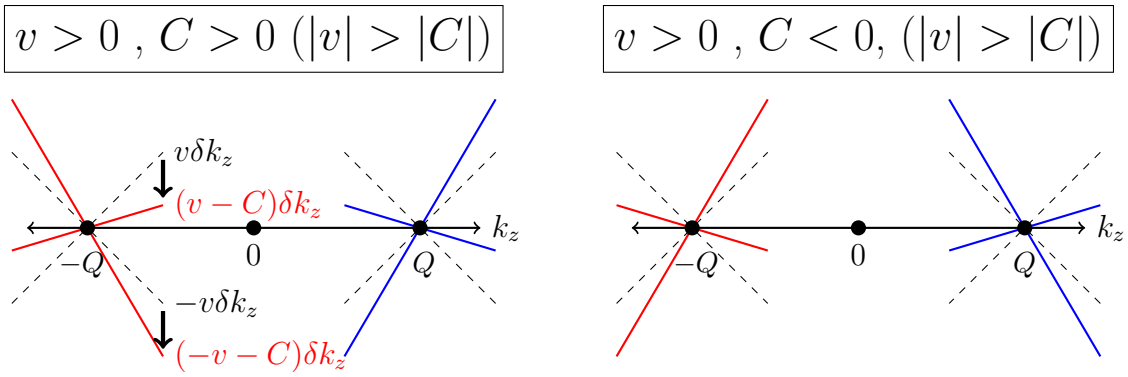

Figure 4.1: Type-I Weyl points with inward (left) and outward (right) tilted Weyl cones.

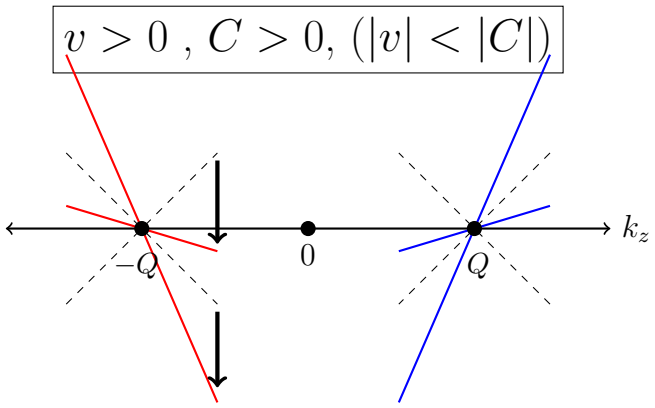

Figure 4.2: Type-II Weyl points tilted inward.

exceeds the Fermi velocity $|C| > |v|$, the Weyl cones can be tilted below the horizontal, transitioning from Type-I to Type-II Weyl points.

For this model, the anomalous Hall contribution in the limit of zero temperature can

be written[188]:

$$
\begin{aligned}
\sigma_{xy} = & \\
& -\frac{e^2}{8\pi^2}\int_{\Lambda-Q}^{-\Lambda-Q} dk_z \Bigg[\mathrm{sign}(k_z)\theta(v^2k_z^2-(Ck_z-\mu)^2) \\
& +\frac{vk_z}{|Ck_z-\mu|}(1-\theta(v^2k_z^2-(Ck_z-\mu)^2))\Bigg] \\
& +\frac{e^2}{8\pi^2}\int_{\Lambda+Q}^{-\Lambda+Q} dk_z \Bigg[\mathrm{sign}(k_z)\theta(v^2k_z^2-(-Ck_z-\mu)^2) \\
& +\frac{vk_z}{|-Ck_z-\mu|}(1-\theta(v^2k_z^2-(-Ck_z-\mu)^2))\Bigg]
\end{aligned}
\tag{4.16}
$$

where ϵ_W is the energy at which the Weyl point is located, $\theta(x)$ is the Heaviside step function, and Λ is an effective momentum cutoff. The first integral in the expression is the contribution from the Weyl at $k_z = Q$, and the second is from the Weyl at $k_z = -Q$. The terms in the first integral can be understood as a contribution of $vk_z/|Ck_z-\mu|$ when $-\mu/(V-C) < k_z < \mu/(V+C)$ and $\mathrm{sign}(k_z)$ otherwise (flip signs for terms in the second integral).

To show how the tilted Weyl cones can enhance the Nernst effect, we rewrite Eq. 4.11 in a more convenient form:

$$
\begin{aligned}
\alpha_{xy} &= \frac{ek_B}{\hbar}\int\frac{d\boldsymbol{k}}{(2\pi)^3}\Omega_z(\boldsymbol{k})\left[\ln\left(1+e^{-\beta(\epsilon-\mu)}\right)+\frac{\epsilon-\mu}{k_BT}f(\boldsymbol{k})\right] \\
&= \frac{ek_B}{\hbar}\int\frac{d\boldsymbol{k}}{(2\pi)^3}\Omega_z(\boldsymbol{k})\left[\ln\left(\frac{1}{1-f(\boldsymbol{k})}\right)+\ln\left(\frac{1-f(\boldsymbol{k})}{f(\boldsymbol{k})}\right)\right] \\
&= \frac{ek_B}{\hbar}\int\frac{d\boldsymbol{k}}{(2\pi)^3}\Omega_z(\boldsymbol{k})s(\beta(\epsilon-\mu))
\end{aligned}
\tag{4.17}
$$

where $s(\beta(\epsilon-\mu)) = -f(\boldsymbol{k})\ln[f(\boldsymbol{k})]-[1-f(\boldsymbol{k})]\ln[1-f(\boldsymbol{k})]$ is the entropy density. To change

variables, we integrate this expression with $\int d\epsilon \delta(\epsilon - \epsilon(\boldsymbol{k}))$, obtaining

$$\begin{aligned}\alpha_{xy} &= \frac{ek_B}{\hbar}\int d\epsilon \int \frac{d\boldsymbol{k}}{(2\pi)^3}\Omega_z(\boldsymbol{k})\delta(\epsilon - \epsilon(\boldsymbol{k}))s(\beta(\epsilon-\mu)) \\ &= \frac{ek_B}{\hbar}\int d\epsilon \frac{\partial \sigma_{xy}}{\partial \epsilon}(\epsilon)\ s(\beta(\epsilon-\mu))\end{aligned} \tag{4.18}$$

where we have recognized $\int \frac{d\boldsymbol{k}}{(2\pi)^3}\Omega_z(\boldsymbol{k})\delta(\epsilon - \epsilon(\boldsymbol{k}))$ as the derivative of Eq. 4.13. This reformulation explicitly shows the relationship between α_{xy} and $\partial\sigma_{xy}/\partial\epsilon$, which reduces to the Mott relation at low temperatures. Furthermore, the Dirac delta function $\delta(\epsilon - \epsilon_{\boldsymbol{k}})$ present within the expression $\partial\sigma_{xy}/\partial\epsilon$ ensures that only a partially occupied band at a given energy will contribute to α_{xy}. This opens up an additional route to increasing the magnitude of α_{xy} besides a larger Berry curvature; increasing the density of states.

Numerically evaluating Eq. 4.16 for various titled Weyl points reveals that the anomalous Hall conductivity σ_{xy} develops a sharp peak when the Weyl cone is tilted close to the transition between Type-I and Type-II ($|C/v| \approx 1$). If the chemical potential is located at the energy of the Weyl point ($\mu = \epsilon_W$), this is exactly the Lifshitz point of the transition between a Weyl semimetal with zero density of states, and a Weyl metal with finite density of states. While it is possible to compute an exact expression for σ_{xy} using Eq. 4.16 for certain model Hamiltonians of tilted Weyl points (See for instance [189]), this result is not particularly illuminating, and in general this problem is not solvable analytically. Instead, we will use a scaling argument to show how σ_{xy} and α_{xy} generally behave near the Lifshitz transition.

The relevant energy scale for the tilted Weyl point model in Eq. 4.15 is $E_c = \hbar v Q$, while the proximity to the Lifshitz point can be captured by the parameter $\delta = 1 - C/v$. From Eq. 4.16, we see that $\sigma_{xy} \sim Q \times e^2/4\pi^2$, with the proportionality term being a dimensionless

integral. We can therefore write the following scaling form [187]:

$$\frac{\partial\sigma_{xy}}{\partial\epsilon} \sim \frac{e^2}{4\pi^2}\frac{Q}{\hbar v Q} \quad \rightarrow \quad \frac{\partial\sigma_{xy}}{\partial\epsilon} = \frac{e^2}{4\pi^2\hbar v} F\left(\frac{\epsilon-\epsilon_W}{|\delta|\hbar v Q}\right) \tag{4.19}$$

where $F(x)$ is a dimensionless scaling function. It can be shown that this scaling result leads to a logarithmic singularity $\sim \ln\left(\frac{\epsilon-\epsilon_W}{|\delta|\hbar v Q}\right)$ in the energy derivative of the Hall conductivity $\partial\sigma_{xy}/\partial\epsilon$[189]. Near the Weyl energy, when $(\epsilon-\epsilon_W) \ll \hbar v Q$, the dominant contribution to this divergence will be $\partial\sigma_{xy}/\partial\epsilon \sim \ln\left(\frac{\epsilon-\epsilon_W}{\hbar v Q}\right)$, and away from this energy it will still experience a cutoff determined by δ, $\partial\sigma_{xy}/\partial\epsilon \sim \ln(|\delta|)$. This in turn leads to a low temperature result for the ANE, $\alpha_{xy} \sim T\ln\left(\frac{\epsilon-\epsilon_W}{\hbar v Q}\right)$, which will also have a logarithmic divergence. Crucially, at higher temperatures, the dependence becomes $\alpha_{xy} \sim T\ln\left(\frac{k_B T}{\hbar v Q}\right)$, violating the Mott formula (Eq. 4.14), where $\alpha_{xy} \sim T$. The temperature at which this occurs is determined by the proximity of the chemical potential to the Weyl energy, so a specific tuning can result in a violation of the Mott relation at arbitrarily low temperatures [187, 189].

4.3 Enhanced ANE in a correlated noncentrosymmetric kagome ferromagnet

In the previous section we explicitly showed how α_{xy} depends only on states near the Fermi energy, and how it is enhanced in a material with critically tilted Weyl points, owing to their non-vanishing density of states. This suggests additional routes for increasing the magnitude of α_{xy} by increasing the density of states. Strong electronic correlations are one such option. As was discussed in Chapter 3, strong correlations can confine electrons to localized orbitals, leading to narrow, renormalized bands at the Fermi energy, particularly when considering the 4f orbitals of lanthanides.

Another mechanism that leads to flat bands with large density of states can occur in

materials with specific kinds of lattice structures. Such a flat band occurs on the kagome lattice, which is a network of corner sharing triangles (or hexagons) in two dimensions. Solving a simple nearest-neighbor tight binding model on the kagome lattice results in two dispersive bands and one dispersionless band, which corresponds to a state of alternating positive and negative weight around the sites of each hexagon. It is clear that such a state is completely localized; considering hoppings from this state to a nearest neighbor on another hexagon, we that the two sites we can hop from will have hoppings of equal amplitude but opposite weight. This leads to a cancelation overall, which confines the wavefunction to a single hexagon and leads to a localized flat band.

This ideal construction breaks down when higher order hoppings are included, especially within a three-dimensional structure. Nevertheless, the presence of a kagome sublattice could result in bands with little dispersion in some or all of the Brillouin zone, which would in turn lead to enhanced transport effects if that band contained topological features. In fact, large AHE and ANE have been observed recently in a number of materials with a kagome sublattice [190, 191, 192, 193, 194].

Thus, in order to maximize the magnitude of AHE and ANE, a material must satisfy several criteria. In order to have non-vanishing intrinsic anomalous transport, the material must have strong spin-orbit coupling effects to produce topological features through the band inversion mechanism, and also break time-reversal symmetry. In addition to this, an ideal material will be strongly correlated and have a kagome sublattice, which will enhance the intrinsic AHE/ANE due to the large density of states of the flat bands these effects produce. Lanthanide and actinide compounds inherently satisfy many of these criteria, and indeed it was recently discovered that $UCo_{1-x}Ru_xAl$, which satisfies all of these criteria, has a large AHE and colossal ANE for a doping $x = 0.2$.

$UCo_{1-x}Ru_xAl$ crystalizes in the inversion-broken ZrNiAl structure type which was previously discussed in Chapter 3. The uranium atoms in this structure form a distorted kagome

lattice, where alternate corner sharing triangles are slightly rotated by opposite angles. The inversion-broken structure gives rise to numerous pairs of Weyl points, however these do not contribute to the AHE or ANE in the paramagnetic state. The endpoints in the doping series, UCoAl and URuAl are paramagnetic, but $UCo_{1-x}Ru_xAl$ is ferromagnetic for the doping range $x = 0.005 - 0.78$ [195, 196], which splits these Weyl points and results in non-zero AHE and ANE. Prior experiments measured a large AHE near the quantum critical point $x = 0.78$ [196].

There is convincing evidence of strong correlations throughout the entire range of dopings $0 < x < 1$. Sommerfeld coefficients γ_{exp} extracted from heat capacity data are around ~ 50 mJ/mol K^2 for the whole doping series [196, 197, 198]. Specifically for $UCo_{0.8}Ru_{0.2}Al$, the doping at which the large anomalous transport effects are observed, a value $\gamma_{\text{exp}} = 41$ mJ/mol K^2 is measured. Comparing this to the theoretical values $\gamma_{\text{the}} = 9 - 13$ mJ/mol K^2, which are computed for a range $E_F \pm 10$ meV to account for the uncertainty in determining the Fermi level, suggests a mass enhancement factor of ~ 3 due to correlations. Correlations have also been confirmed by photoemission and X-ray measurements [199, 200].

We will now summarize the main experimental results for $UCo_{0.8}Ru_{0.2}Al$ [183]. The resistivity ρ_{xy} is -11 $\mu\Omega$cm and -16 $\mu\Omega$cm at 2 K and 40 K respectively, with the former corresponding to a conductivity of $\sigma_{xy} = 980/\Omega$cm. These values are comparable with the giant values AHE recently measured for Co_2MnGa and $Co_3Sn_2S_2$ [187, 196]. However, the anomalous Nernst effect in $UCo_{0.8}Ru_{0.2}Al$ exceeds any previously recorded value, reaching reaching 23 μV/K at T = 40 K, exceeded even the $\alpha_{xy} = 6$-8 μV/K seen in Co_2MnGa [187]. What is most striking about this result is the relative magnitude of α_{xy} relative to σ_{xy}. It has been argued that since α_{xy} is related to entropy transport, and σ_{xy} is related to charge transport, there is a natural upper bound $\alpha_{xy}/\sigma_{xy} < k_B/e = 86\mu$V/K [201]. In $UCo_{0.8}Ru_{0.2}Al$ this ratio is 170μV/K at 47 K, which suggests that multiple bands are contributing to the large ANE[183].

To understand these experimental results, we compute the electronic structure of doped $UCo_{1-x}Ru_xAl$ within the framework of the full potential linear muffin tin orbital method [61], using the local spin density approximation (LSDA) which has been previously employed to study uranium compounds with the ZrNiAl-type structure [202, 203, 204].

To examine the effect of doping on the electronic structure, we perform calculations for the parent compound UCoAl, as well as doped at the $x = 1/3, 2/3$ and 1 levels, using the experimental lattice parameters. The UTAl (T=Co,Ru) structure has two inequivalent sites for atom T, T_1 and T_2, with Ru preferentially occupying the two T_2 sites [205, 206]. Therefore calculations on the chemically ordered compounds $UCo_{2/3}Ru_{1/3}Al$, $UCo_{1/3}Ru_{2/3}Al$ with Ru at the T_2 site will give a representative picture of the doping effects on the electronic structure of $UCo_{1-x}Ru_xAl$. The resulting band structures are shown below.

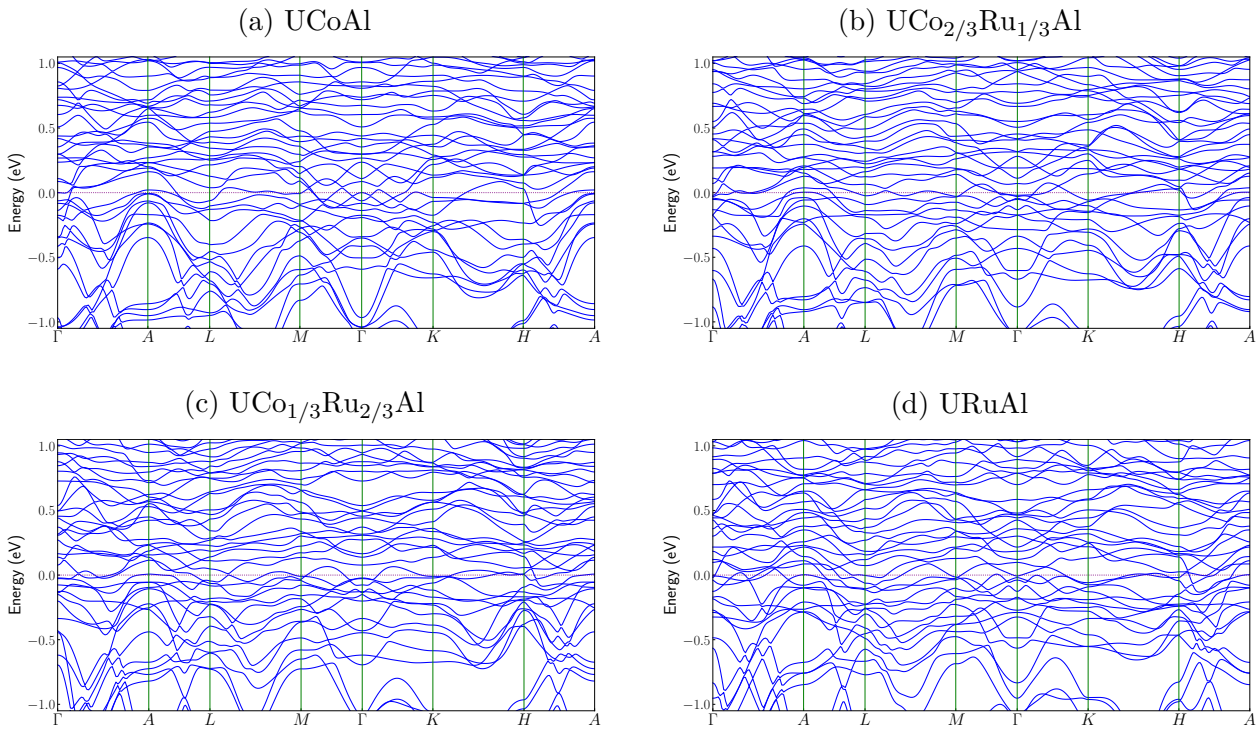

Figure 4.3: Computed band structures for the stoichiometric compounds in the $UCo_{1-x}Ru_xAl$ series, with $x = 0, 1/3, 2/3, 1$. $E_f = 0$ is the Fermi level corresponding to the $x = 0.2$ doping.

Figure 4.3 shows that as Ru is substituted for Co, the band structure remains largely

unchanged, aside from a downward shift in the Fermi level due to the removal of electrons. The Fermi level $E_f = 0$ is set to the energy corresponding to the $x = 0.2$ doping level, which will be used consistently throughout the supplement. These calculations indicate that a rigid band approximation for doped $UCo_{1-x}Ru_xAl$ is appropriate.

The uranium f-orbitals reside on a kagome lattice. Thus, the effects of frustrated hopping on such a lattice and the small spatial extent of the 5f orbitals will be intermixed. Identifying specifc bands associated with the kagome structure is further complicated by the multiorbital nature of uranium, the presence of ligand orbitals, and the three dimensionality of the structure. Nevertheless, multiple flat bands can be observed in the bandstructure plots of Fig. 4.3. One would expect the at bands near the Fermi energy to be renormalized by electronic correlations present in this system.

For UCoAl, the computed orbital $\mu_l = 1.19\mu_B$ and spin $\mu_s = -0.98\mu_B$ magnetic moments, which are similar to those found in prior calculations [207]. Experimentally $UCo_{1-x}Ru_xAl$ is non-magnetic, developing a magnetic moment in the doping range $x = 0.005 - 0.78$, with a maximum uranium magnetic moment $\mu_U = 0.6\mu_B$ around $x = 0.3$[208]. Therefore, with the appropriate adjustment of Fermi level, our calculated electronic structure for UCoAl is a reasonable model to compare with experimental observations for doped $UCo_{0.8}Ru_{0.2}Al$. It is important to note that our model is only valid at energies corresponding to dopings within the magnetic range, and not for the paramagnetic end points. We further emphasize that while details of the actual electronic structure may vary, the main observation of an abundance of topological features close to E_f will be insensitive to variations of the electronic structure.

4.4 Identification of Topological Features

To understand the origin of the large anomalous Hall and anomalous Nernst effects in $UCo_{0.8}Ru_{0.2}Al$, we perform previously developed mining procedure [35] to find topological features in the electronic structure of UCoAl. A density of states calculation revealed that the Fermi level of the $x = 0.2$ doped case lies 41 meV below the Fermi level of undoped UCoAl. Because the topological features closest to the Fermi level will be the most relevant to the transport properties, we scanned the range of energies $E_f \pm 60$meV for topological features.

We divide the BZ into an initial coarse k-grid of $30 \times 30 \times 30$ divisions, and compute the Berry curvature flux through the surface of each k-cube. This grid is subsequently refined by iteratively repeating the search procedure on a $2 \times 2 \times 2$ grid within each k-cube until the desired precision is achieved. This allows us to find the locations of sources/sinks of Berry curvature flux, simultaneously confirming the topological nature of the features as well as their positions in k-space. Our procedure reveals a number of topological features in $UCo_{0.8}Ru_{0.2}Al$, including Weyl points, nodal lines, and triple points. The triple points[68] only exist within the paramagnetic state, and therefore, will not be discussed further. Both Weyl nodes and nodal lines exist in the ferromagnetic state.

The Weyl points we identify in $UCo_{0.8}Ru_{0.2}Al$ are summarized in Table 4.1, and can be classified into one of three general sorts. The main two sorts of Weyl points we term Weyl-A′ and Weyl-B′, due to their relationship to the Weyl-A and Weyl-B sorts of Weyl points we have previously identified for compounds with the ZrNiAl-type structure [35].

For reference, Weyl points belonging to sort Weyl-A form six pairs found along the $\Gamma - M$ line, and separated along the k_z direction. Weyl-B points are instead 12 pairs which are found in sets of four, symmetrically displaced from the $\Gamma - K$ line. The reason for 12 Weyl points being the minimum number can be understood in terms of a symmetry argument.

Band	Location	T	#	δk_z	v (Ry/$\hat{k}$)	C (Ry/$\hat{k}$)	E
71	(0.00000, 0.33057, 0.02756)	A′	6	0.0030000	-0.0418333	0.0183333	-63
71	(0.00000,-0.53900, 0.09977)	A′	6	0.0268000	-0.0549254	0.0107090	-30
71	(0.00000, 0.15877, 0.12084)	A′	6	0.0174000	-0.0427011	-0.0177299	-15
71	(0.00000,-0.45758,-0.12498)	A′	6	0.0317400	0.0811122	-0.0017171	-22
71	(0.00000, 0.55407, 0.22190)	A′	6	0.0178400	-0.0225897	0.0070348	-6
71	(0.61459, 0.05412,-0.12708)	B′	12	0.0304600	0.0391005	0.0207814	-51
71	(0.41976, 0.10908,-0.42260)	B′	12	0.0112000	0.0174554	-0.0062946	-32
71	(0.00000, 0.31823,-0.45537)	A′	6	0.0112000	0.0132366	-0.0018973	-44
71	(0.00000,-0.38203, 0.38948)	A′	6	0.0240000	-0.0208750	0.0056250	+2
72	(0.00000, 0.38736, 0.00434)	A′	6	0.0040000	-0.0842500	0.0823750	-51
72	(0.00000, 0.51091,-0.01959)	A′	6	0.0078000	0.0377885	-0.0377884	+26
72	(0.00000,-0.07528,-0.03239)	A′	6	0.0049560	0.0329903	-0.0069613	-23
72	(0.27505,-0.00369, 0.03266)	B′	12	0.0030000	-0.0510833	0.0505833	-32
72	(0.00000, 0.08053, 0.02120)	A′	6	0.0048000	-0.0233333	0.0063542	-28
72	(0.00000, 0.23693,-0.05635)	A′	6	0.0126000	0.1351587	0.1173413	-1
72	(0.00000,-0.18377, 0.09803)	A′	6	0.0130000	-0.1004615	0.0413462	+28
72	(0.40132,-0.13379,-0.13770)	B′	12	0.0130000	0.0300000	0.0206538	+59
72	(0.00000, 0.00000, 0.22577)	k_z	2	0.0210000	-0.0063095	0.0300238	+57

Table 4.1: Weyl points of $UCo_{0.8}Ru_{0.2}Al$ series. The first column gives the lower band number of two bands comprising the Weyl point. The second column gives the position of one positive charge given for each symmetry-related set of Weyl points. The third and fourth columns give the classification type (T) of the Weyl points as Weyl-A′ (A′), Weyl-B′ (B′), or k_z, and the number of symmetry-related Weyl points in the set. The remaining columns give the momentum cutoff δk_z, velocities v and C, and energy E, of each Weyl point in meV relative to the Fermi energy. Wavevectors $\hat{k}$ are given in units of $2\pi/a, 2\pi/a, 2\pi/c$.

While Weyl points can arise due to the absence of either time-reversal $\mathcal{T}$ or inversion $\mathcal{I}$ symmetries, here they exist due to broken inversion. Now, while $\mathcal{T}(\boldsymbol{k}) = -\boldsymbol{k}$, the topological charge of a Weyl point is invariant under $\mathcal{T}$. This means that a positively charged Weyl point located at $\boldsymbol{k}$ will have a positively charged partner at $-\boldsymbol{k}$, each of which will have a negatively charged partner across the σ_z mirror plane as shown in Fig 4.4a. In combination with the three-fold symmetry of the BZ, this guarantees that each Weyl point belongs to a symmetry-related set with a number of members that is a multiple of twelve.

In $UCo_{0.8}Ru_{0.2}Al$, the uranium magnetic moments break $\mathcal{T}$-symmetry on top of the already absent inversion symmetry of the lattice. This means that the inversion symmetry

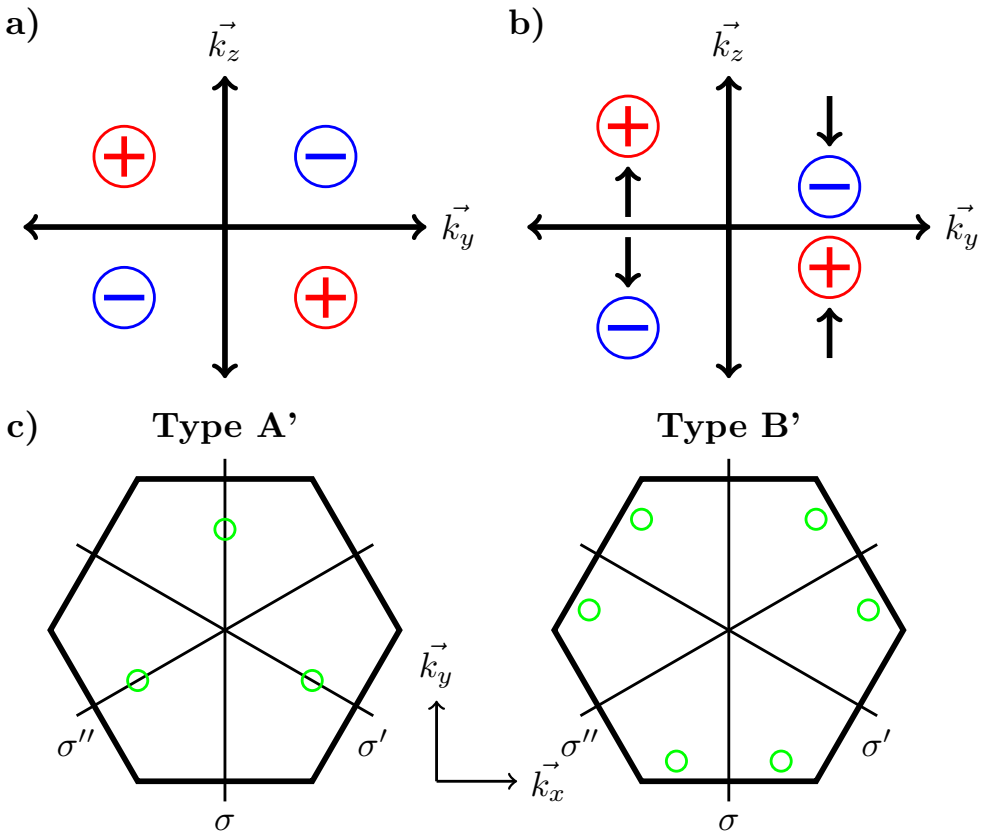

Figure 4.4: a) 4 Type-A Weyl points in $UCo_{0.8}Ru_{0.2}Al$ in the absence of magnetism. b) Turning on the magnetism breaks $\mathbf{k} \leftrightarrow -\mathbf{k}$ symmetry, splitting the original set of Weyl points into two sets of Type A' or Type B'. c) Symmetries of Type A' and Type B' Weyl points in $UCo_{0.8}Ru_{0.2}Al$ within the k_x–k_y plane.

$\mathbf{k} \leftrightarrow -\mathbf{k}$ in $\boldsymbol{k}$-space is fully broken, splitting the Weyl A and Weyl B sorts each into two sets of Weyl A′ or Weyl B′ sorts, with 6 and 12 members respectively (Fig 4.4c). This can be understood as a direct consequence of the Zeeman-like effect shifting the bands, causing the k_z-separation between Weyl point partners to increase or decrease (Fig 4.4b). A similar mechanism can create lone pairs of Weyl points along the $\Gamma - A$ axis, separated only along the k_z direction [37]. Since this sort of Weyl point is pinned to the k_z-axis, application of point group symmetries does not yield any new symmetry-related members. Therefore these sets have only two members, which is the minimum for materials with broken $\mathcal{T}$-symmetry.

In addition to the Weyl points we find a number of topological nodal lines in the electronic structure of UCoAl, shown in Figure 4.5a. This type of nodal line can arise at

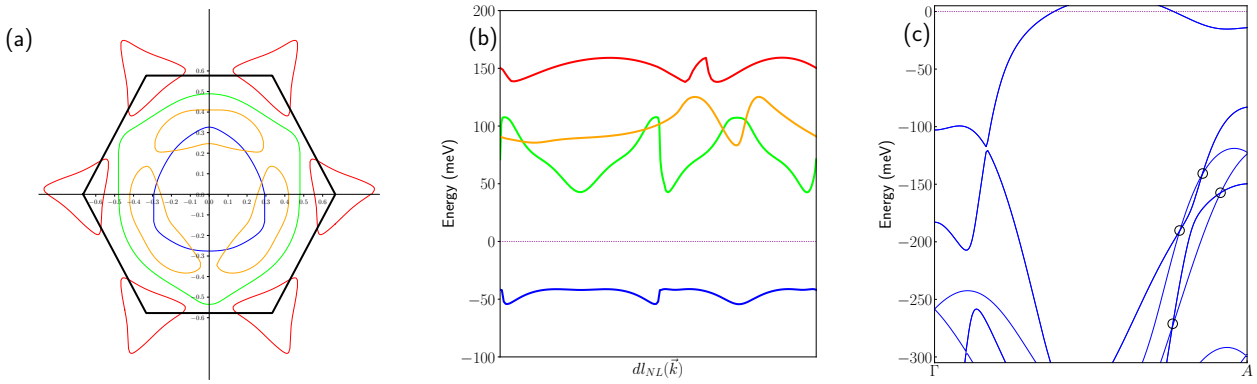

Figure 4.5: a) Nodal lines within the σ_z plane of UCoAl. b) Nodal lines plotted as a function of energy. c) Paramagnetic band structure plot of UCoAl computed with LDA. Triple point locations are indicated by black circles. $E_f = 0$ corresponds to the $x = 0.2$ doping level.

the intersection of two bands belonging to two different irreducible representations of the mirror plane point group. In UCoAl, these nodal lines have different eigenvalues when acted upon by the σ_z mirror plane. As a result the band degeneracy at their intersection point is topologically protected against small distortions.

These nodal lines are located at least 50 meV above/below the Fermi energy (Fig 4.5b). While they occupy a larger part of the topological phase space than the Weyl points, they likely don't make a significant contribution to the Berry curvature at the Fermi energy of the x = 0.2 doped case. Specifically, the nodal lines lying within the σ_z mirror plane will not contribute to Ω^z_{xy} and hence will not impact σ_{xy} or α_{xy}.

The UCoAl crystal structure belongs to the inversion broken $p\bar{6}2m$ (# 189) space group, which can also host triple-points [68]. Our procedure was able to locate several pairs of such triple points (Fig 4.5c). Like the nodal lines, these triple points are located far below the Fermi level, at -272 meV, -158 meV, -141 meV, and -191 meV below E_f, respectively. Hence, like the nodal lines, they would have a negligible effect on the Berry curvature calculation for $UCo_{0.8}Ru_{0.2}Al$. More importantly, the existence of these triple points requires time-reversal symmetry, which is broken in $UCo_{0.8}Ru_{0.2}Al$ by the uranium magnetic moments.

The large number of topological features in UCoAl result in a dense population of

singularities in the Berry curvature. This means that the standard approach for computing anomalous Hall and anomalous Nernst effects would require dense $\boldsymbol{k}$-grids that are too large to be computationally tractable. Instead, we take a pragmatic approach by using the solvable model (Eq. 4.15) we previously introduced to model each pair of identified Weyl points, allowing us to practically compute the anomalous Hall effect (Eq. 4.16) at $T = 0$.

Using this model, the anomalous Nernst effect α_{xy} can also be computed directly by integrating the zero-temperature anomalous Hall using Eq. 4.12 [182]:

$$\begin{aligned}\alpha(T,\mu) &= -\frac{1}{e}\int d\epsilon \left(\frac{\partial f_{\mathrm{FD}}}{\partial \mu}\right)\sigma(0,\epsilon)\frac{\epsilon-\mu}{T} = -\frac{1}{e}\int d\epsilon \frac{e^{(\epsilon-\mu)/(k_BT)}}{k_BT\left(e^{(\epsilon-\mu)/(k_BT)}+1\right)^2}\sigma(0,\epsilon)\frac{\epsilon-\mu}{T} \\ &= -\frac{1}{eT}\int w(\frac{\epsilon-\mu}{k_BT})\sigma(0,\epsilon)d\epsilon \end{aligned} \tag{4.20}$$

where f_{FD} is the Fermi-Dirac distribution, and $w(x) = xe^x/(e^x+1)^2$ is a weight function introduced to simplify the expression.

In turn, the anomalous Nernst effect can be computed from the zero-temperature anomalous Hall through the following formula [182]:

$$\begin{aligned}\alpha(T,\mu) &= -\frac{1}{e}\int d\epsilon \left(\frac{\partial f_{\mathrm{FD}}}{\partial \mu}\right)\sigma(0,\epsilon)\frac{\epsilon-\mu}{T} = -\frac{1}{e}\int d\epsilon \frac{e^{(\epsilon-\mu)/(k_BT)}}{k_BT\left(e^{(\epsilon-\mu)/(k_BT)}+1\right)^2}\sigma(0,\epsilon)\frac{\epsilon-\mu}{T} \\ &= -\frac{1}{eT}\int w(\frac{\epsilon-\mu}{k_BT})\sigma(0,\epsilon)d\epsilon \end{aligned} \tag{4.21}$$

where f_{FD} is the Fermi-Dirac distribution, and $w(x) = xe^x/(e^x+1)^2$ is a weight function introduced to simplify the expression.

The computed anomalous Hall effect for the Weyl points listed in Table 4.1 is shown in Figure 4.6a. A large value of σ_{xy} appears just above the Fermi level, suggesting that a collective contribution from several Weyl points could explain the large experimentally observed values. This plot must be interpreted very carefully for a number of reasons.

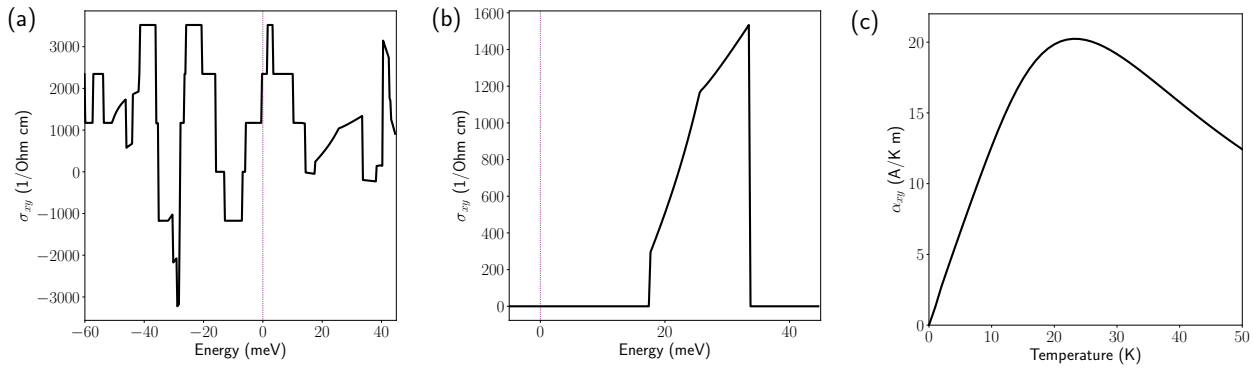

Figure 4.6: a) Anomalous Hall effect computed for all Weyl points in $UCo_{0.8}Ru_{0.2}Al$. b) The anomalous Hall effect for set of Weyl points at +26 meV c) The anomalous Nernst effect as a function of temperature computed with the chemical potential set at +26 meV.

Firstly, the anomalous Hall contribution for each pair of Weyl points depends on their k_z separation, which in turn depends on the uranium magnetic moments. As we have previously mentioned, these are difficult to reproduce numerically. Secondly, while we take a relatively dense initial grid of $30 \times 30 \times 30$ k-points to search for topological features, the dense distribution of the Weyl points we found suggests the possibility that some initial k-cubes may contain multiple Weyl points, meaning there may be yet more additional Weyl points missed by our procedure. Thirdly, this calculation does not include contributions from nodal lines and other sources. Finally, $UCo_{1-x}Ru_xAl$ is magnetic for dopings $x = 0.005 - 0.78$, so outside of this range, our model would not apply.

We also draw attention to the anomalous Hall effect contribution coming from the Weyl point located at (0.0, 0.51,-0.02) and 26 meV above the Fermi energy (and its symmetry related partners) (Fig 4.6b,c). The anomalous Nernst contribution of these points is computed by setting the chemical potential at +26 meV and evaluating the above integral. This set of Weyl points is close to a Lifshitz transition between Type-I and Type-II tilting. As has already been shown, for tilted Weyl points near the Lifshitz transition, $\partial\sigma_{xy}/\partial\epsilon$ diverges logarithmically at the critical tilt, resulting in large anomalous Hall and Nernst effects, as well as an amplification of α_{xy} relative to σ_{xy} [187]. In $UCo_{0.8}Ru_{0.2}Al$, these Weyl points are located +26 meV above the Fermi energy, corresponding to a doping of $x = 0.07$, and are

sufficient to explain the large anomalous Hall ($\sim$ 1200 [Ohm cm]$^{-1}$) and large anomalous Nernst ($\sim$ 20 A/K m) observed in this material.

We reiterate again that the Weyl points in this material, along with their associated Berry curvature and other observable properties, are highly sensitive to the uranium magnetic moments. This means that in the undoped case, the absence of magnetism would guarantee a zero anomalous Hall effect, even though Fig 4.6a suggests a large value near the Fermi energy. Additionally, as it is difficult to exactly reproduce the uranium magnetic moment μ_U, meaning that in the real material, this critical set of Weyl points may be located at a lower energy corresponding to the $x = 0.2$ doping level.

A final consideration is that the magnetism in UCoAl disappears at higher temperatures, meaning the anomalous Nernst effect will rapidly go to zero as it approaches the magnetic transition.

First principles calculations of the electronic structure of uranium compounds are notoriously challenging, and this is especially the case when very fine resolution of topological features is necessary. To summarize, our calculations yield a large number of topological features, including Weyl points, triple points, and nodal lines. Some Weyl nodes are sufficient to explain the large anomalous Hall and anomalous Nernst observed in $UCo_{0.8}Ru_{0.2}Al$. Additional calculations and measurements are needed to identify which features are most responsible. However, we emphasize that the observation of a large number of Weyl points, and hence large ANE and AHE, are independent of the details of the calculation. The colossal ANE observed in $UCo_{0.8}Ru_{0.2}Al$ is several times larger than any previously observed, and is likely the result of kagome structure and strong correlations which drive the formation of narrow bands and the enhancement of transport properties. We hope that this material can serve as a blueprint for the future design and realization of topological materials for thermoelectric applications.

Chapter 5

Calculated Exchange Interactions and Sensitivity of Ni Two-Hole Spin State to Hunds Coupling in Doped $NdNiO_2$

The discovery of high temperature superconductivity in cuprates[209] started an incredible effort to understand the superconducting mechanism. This effort is still ongoing to this day, and has spawned many subfields and models, which while ultimately falling short of a complete explanation of unconventional superconductivity in cuprates, have found applications in many other areas of condensed matter physics. The resonating valence bond model was one such model first proposed by Anderson in 1973 to represent a so-called "quantum spin liquid" that described the spin-1/2 Heisenberg antiferromagnet on the triangular lattice[210]. This resonating valence bond model was again employed by Anderson in 1987, when he proposed that superconductivity might emerge upon doping a quantum spin liquid[211]. It was soon realized that the physics of the ground states in the resonating band model could be understood as a long range topological order [212, 213], which was later described within the framework of Chern-Simons theory[214]. These early developments

laid the groundwork for understanding topological states in condensed matter systems, and served as the foundation for describing symmetry-protected topological states such as Chern insulators, topological insulators, and topological semimetals.

There are a number of excellent reviews on the history of quantum spin liquids, their connection to our understanding of high-temperature superconductivity, and the concept of topological order [215, 216, 217, 218], which will not be discussed here. While this long-range topological order is distinct from the short-range symmetry-protected topological states discussed in previous chapters, the study of unconventional superconductivity is deeply connected with these topics, and is a generally important topic in the field of strongly correlated condensed matter physics. This chapter will focus on the theoretical study of recently discovered superconductor $Nd_{1-x}Sr_xNiO_2$, and will discuss these results in the context of the structurally-similar cuprate superconductors.

The work described in this chapter was done in collaboration with Xiangang Wan, Giacomo Resta, Ivan Leonov, and Sergey Savrasov. It is published in Physical Review B [219], and was presented at APS March Meeting 2021.

5.1 Superconductivity in cuprates and nickelates

Since the discovery of high–temperature superconductors (HTSCs)[209], tremendous theoretical and experimental efforts have been devoted to understanding the novel physics of this family of compounds[220, 221, 218]. All HTSCs are comprised of quasi–two–dimensional CuO_2 planes separated by charge reservoir spacer layers, and their parent compounds have antiferromagnetic (AFM) order with very strong in–plane magnetic exchange interactions, belonging to the class of charge–transfer insulators[222]. Upon doping, holes occupy the O–$2p$ orbital, and due to the strong hybridization between Cu–$3d_{x^2-y^2}$ and O–$2p$ orbitals,

a Zhang–Rice singlet is formed[223]. It has been widely accepted that the HTSCs can be described by an effective single band t–J model, with different parameters explaining the variation in T_c in different materials [224, 225].

Inspired by HTSCs, the search for possible novel superconducting behavior in nickelates has been attracting significant attention, as their structure and electronic configuration is similar to that of the cuprates [226, 227, 228, 229]. Unfortunately, the monovalent Ni ion is strongly unstable and scarcely formed in mineral compounds, making, for example, $LaNiO_2$ difficult but possible to synthesize[227]. First–principles Local Density Approximation (LDA) based calculations revealed an important difference between $LaNiO_2$ and its sister infinite–layer HTSC compound $CaCuO_2$: the Fermi surface of $CaCuO_2$ consists of only one two–dimensional band, while $LaNiO_2$ seems quite three–dimensional, with La–derived $5d$ states and Ni–$3d$ states crossing the Fermi level[230]. Numerical calculations predicted AFM magnetic order[230, 231], but magnetization and neutron powder diffraction observe no long–range order in $LaNiO_2$[228]. At high temperatures (150K $<$ T $<$ 300K), the susceptibility of $LaNiO_2$ can be fitted by the sum of a temperature independent term, and a Curie–Weiss $S = \frac{1}{2}$ paramagnetic term with a large Weiss constant ($\theta = -257$K), indicating a significant correlation between Ni spins[228]. $LaNiO_2$ shows metallic behavior, but resistivity increases at lower temperatures and no superconducting state has been observed [226, 227, 228].

Recently, $Nd_{0.8}Sr_{0.2}NiO_2$ thin films were synthesized on a $SrTiO_3$ substrate using soft–chemistry topotactic reduction, and superconductivity with considerably high T_c (up to 15K) was observed[232]. The superconducting phase displays a doping–dependent dome for $Nd_{1-x}Sr_xNiO_2$ ($0.125 < x < 0.25$), which is remarkably similar to that of the cuprates [233, 234]. Very recently, superconductivity has also been observed in doped $PrNiO_2$[235].

These breakthroughs have stimulated large–scale theoretical efforts to understand the nature of the superconductivity in rare–earth nickelates. LDA band structures [236] predict

that both Nd–5d and Ni–3$d_{x^2-y^2}$ orbitals contribute significantly to the Fermi surface of parent compound $NdNiO_2$. Most calculations treat the three 4f electrons in Nd^{3+} as core electrons, although the role of Nd–4f has been emphasized recently[237]. Many–body perturbative GW calculations result in almost no modification to the Fermi–surface topology and its orbital composition[238]. Focusing on the Fermi surface, different minimal models have been proposed to describe the low energy physics of this material using a Wannier function approach, including: a three–band model with Ni-3$d_{x^2-y^2}$, Nd–5$d_{3z^2-r^2}$ and an interstitial s orbital[239]; a three–band model with Ni–3$d_{x^2-y^2}$, Nd–5$d_{3z^2-r^2}$ and Nd–5d_{xy}[240, 241]; a two–band model with Ni–3$d_{x^2-y^2}$ and Nd–5$d_{3z^2-r^2}$[242, 243]; and a four–band model[244]. The effect of topotactic hydrogen has been discussed as well[245].

Several works have addressed strong correlation effects among Ni 3d electrons [246, 247, 248, 249, 250, 251, 252, 253, 254, 255, 256, 257, 258, 259, 260, 261, 262, 263]. Due to a large energy difference between O–2p and Ni–3d levels, the undoped $NdNiO_2$ has been suggested to be a Mott insulator, and a coexistence/competition between low energy S=0 and S=1 states has been proposed for the hole doped case [246] where some Ni ions would acquire a formal $3d^8$ configuration. The origin of these two–hole states has been discussed in a recent literature[247, 248, 249, 250, 251, 252]. As it is commonly accepted that the undoped Ni $3d^9$ configuration corresponds to the hole of x^2-y^2 symmetry, the two–hole states produced by doping can either end up as intraorbital singlets or interorbital triplets. It has been first pointed out[246] that the S=1 state maybe incompatible with robust superconductivity, and indeed exact diagonalization study of Ni impurity embedded into the oxygen environment [246] as well as a number of many–body calculations using a combination of LDA with Dynamical Mean Field Theory (DMFT)[247, 250] pointed to the formation of the intraorbital singlets.

The first–principles physics of competing Ni-3$d_{x^2-y^2}$ vs. Ni–3$d_{3z^2-r^2}$, and the connected issue of having the Ni–3$d_{3z^2-r^2}$ states at the Fermi level with hole doping has been first put

forward in Ref. [251]. In addition, the role of Ni-3$d_{x^2-y^2}$ and Ni-3$d_{3z^2-r^2}$ orbitals has been emphasized in Ref. [247]. A recent GW+DMFT work [253], highlighted Ni-3$d_{3z^2-r^2}$ flat–band physics as well as Ref. [254]. Furthermore, a variant of the t–J model with S=1 has been proposed and shown to exhibit d–wave superconductivity[249]. Symmetries of the pairing states based on a two–orbital Ni-3$d_{x^2-y^2}$/Ni-3d_{xy} model Hamiltonian with competing S=0 and S=1 two–hole states have been discussed[248]. DMFT calculations for the two–orbital Ni–3$d_{x^2-y^2}$/Ni–3$d_{3z^2-r^2}$ system argued that a multiorbital description of nickelate superconductors is necessary [252]. Excitations and superconducting instabilities have also been explored by a random phase approximation [255]and by a variant of the t-J model[256]. Local spin, charge and orbital susceptibilities have been calculated using a combination of DMFT with a local quasiparticle self–consistent GW method and emphasized the Hund's physics of Ni–e_g electrons[257].

No sign of magnetic order has been observed in the original report on superconductivity in $NdNiO_2$[232], which may be attributed to defects, such as unwanted hydrides or hydroxides that might form as by–products of the creation of the rare Ni^+ oxidation state during the synthesis of this compound. Another consideration is that $LaNiO_3$ is close to an antiferromagnetic quantum critical point (QCP)[264], therefore it is reasonable to expect that with lower dimensionality, $NdNiO_2$ would pass the QCP and display magnetism. Very recently, strong spin fluctuations and considerable AFM exchange interactions have been observed in $NdNiO_2$[265] as well as nuclear magnetic resonance (NMR) data [266] provided an addtional evidence for quasi–static AFM order below 40 K and dominant spin fluctuations at higher temperatures in $Nd_{0.85}Sr_{0.15}NiO_2$ bulk materials. The exchange interactions have also been discussed in several works [240, 267, 268, 269]. The calculated electron–phonon interaction ($\lambda \leq 0.32$) is too small to explain the 15K T_c in this material[239], meaning the spin excitations, which are thought to be responsible for the superconductivity in HTSCs[220, 221, 218], are worth careful investigation.

In this work, based on a density functional LDA+U method and linear–response theory[270], we perform detailed studies of exchange interactions for both parent and doped $NdNiO_2$. The method does not rely on a total energy analysis, and instead directly computes the exchange constant for a given wave vector $\mathbf{q}$ based on the result of the magnetic force theorem [271]. Our results show that although the Fermi surface of undoped $NdNiO_2$ is quite three–dimensional, its magnetic exchange interaction J has a clear two–dimensional feature with large in–plane $J_1 = 82$ meV and much smaller out–of–plane J_{z1}. However, the Ni–$3d_{3z^2-r^2}$ band close to the Fermi level is quite flat, therefore within the LDA+U method for a reasonable range of the values of Hubbard U above 4 eV, holes introduced by doping preferentially occupy the Ni–$3d_{3z^2-r^2}$ orbitals while Ni–t_{2g} states remain remarkably inert. The in–plane J_1 remains largely unaffected by doping, but the magnetic moment of the Ni–$3d_{3z^2-r^2}$ orbital and the out–of–plane J_{z1} both grow significantly in accord with recent findings[254] Our calculation using a constrained–orbital–hybridization method [272] unambiguously demonstrates that while Nd–$5d$ makes an important contribution to the Fermi surface, it has almost no effect on the magnetic exchange interaction. It is expectable result, since it is known that Nd-5d orbitals have negligible hybridization with Ni orbitals [239, 273]. This means the magnetic excitations in hole–doped $NdNiO_2$ can be described by an effective model including Ni–$3d_{x^2-y^2}$/Ni–$3d_{3z^2-r^2}$ orbitals whose role has been emphasized in many recent works [236, 237, 238, 239, 240, 241, 242, 243, 244, 245, 246, 247, 248, 249, 250, 251, 252, 253, 254, 255, 256, 257, 258, 259, 260, 261, 262, 263].

To gain additional insight, we discuss the solutions of such two–band model on the basis of Dynamical Mean Field Theory using the parameters deduced from our band structure calculations. In contrast to the static mean field description, such as LDA+U, where holes occupying Ni–$3d_{3z^2-r^2}$ states promote interorbital triplets, whether S=0 or S=1 state emerges from our DMFT simulation depends on a precise value of the intraatomic Hund's coupling J_H in the vicinity of its commonly accepted range of values 0.5–1 eV. This leads to very different quasiparticle band structures. We thus propose that trends upon doping in magnetic

exchange interactions and quasiparticle density of states can be a way to probe Ni $3d^8$ configuration.

5.2 Calculations of exchange interactions in doped $NdNiO_2$

We perform our density functional based electronic structure calculations within the full potential linear–muffin–tin–orbital (LMTO) method[61]. To take into account the effect of on–site electron–electron interactions between Ni–$3d$ orbitals we add a correction due to Hubbard U using the so–called LDA+U approach[274]. Although, the experimental situation on magnetism in nickelates is still unclear, hinted by the cuprate physics, an assumption of the AFM ordered state in the parent compound should be a good starting point for a theoretical modeling. Ultimately, if AFM spin fluctuations in the doped state are responsible for superconductivity, the exchange interactions in the ordered state set the scale for those fluctuations, which justifies this assumption and provides the basis for our static linear response calculation of J's. An alternative measure of those spin fluctuations would be a full calculation of wavevector and frequency dependent spin susceptibility directly in paramagnetic state. Although possible, in principle, it is a lot more involved and goes beyond the scope of this work.

We vary the parameter U for Ni–$3d$ between 4.0 and 8.0 eV, and find that the essential properties and our conclusions do not depend on the value of U in this range[275]. Below we report our results for exchange constants with $U = 6$ eV and Hund's $J_H = 0.95$ eV. Experimental lattice parameters have been used[232].

The magnetic exchange interactions $J(\mathbf{q})$ were evaluated assuming a rigid rotation of atomic spins, using a previously developed linear–response approach [270]. This technique has been applied successfully to evaluate exchange interactions for a series of materi-

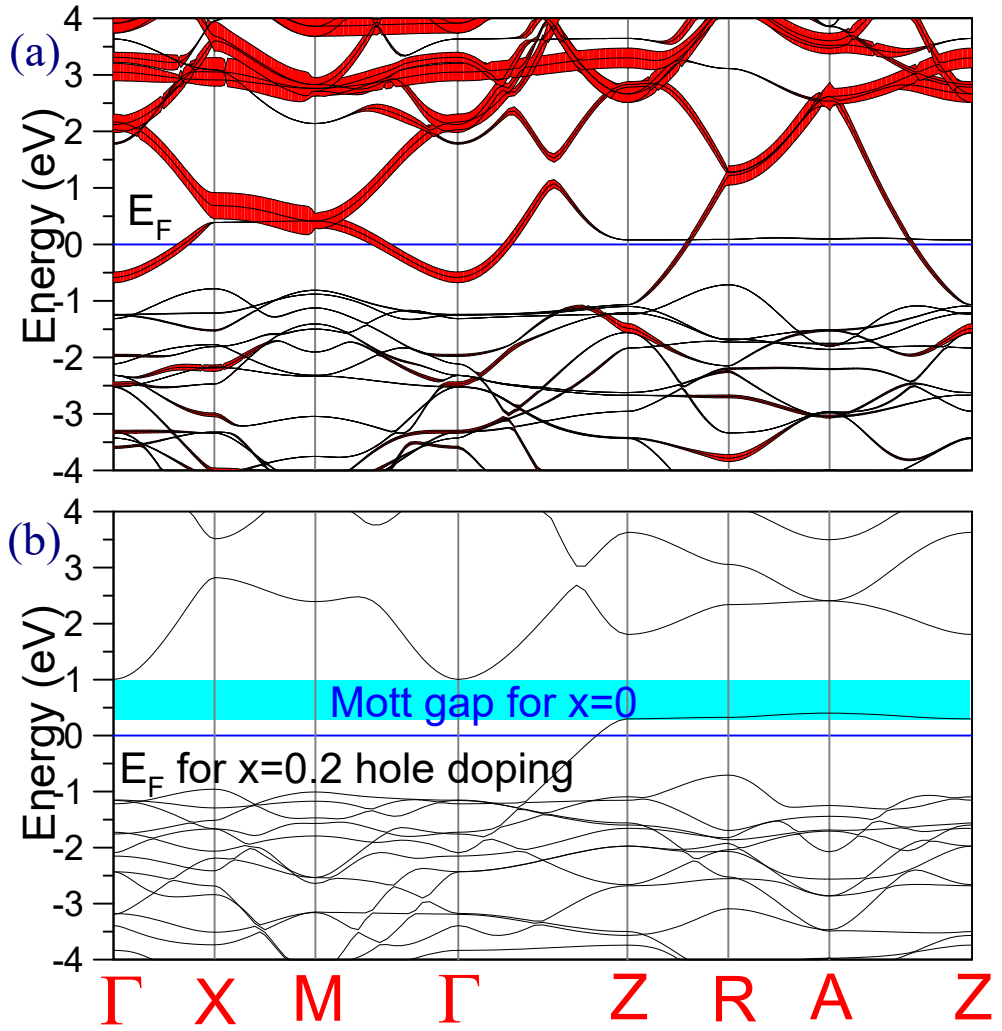

Figure 5.1: Band structure of (π,π,0) AFM ordered $NdNiO_2$ from LDA+U calculations with $U = 6.0$ eV. (a) undoped $NdNiO_2$ with Nd–5d oribtal character shown in red, (b) constrained orbital-hybridization calculation for $NdNiO_2$ with the Nd–5d band shifted up by 2 Ry. The position of the Fermi level corresponds to 0.2 hole doping.

Table 5.1: Calculated exchange interactions, J_1, J_2 (in-plane nearest, next-nearest) and J_{z1}, J_{z2} (out-of-plane nearest, next-nearest) in meV for various hole dopings x. Positive/negative sign denotes AFM/FM interaction. We also list the calculated total magnetic moment at the Ni site, M_{tot}, and magnetic moment at the Ni-$3d_{3z^2-r^2}$ orbital, $M_{3z^2-r^2}$, (in μ_B).

x	J_1	J_2	J_{z1}	J_{z2}	M_{tot}	$M_{3z^2-r^2}$
0.00	82.24	-4.84	-3.40	-23.00	0.97	0.17
0.05	71.84	-5.08	-21.40	-22.40	1.03	0.23
0.10	65.88	-5.68	-39.36	-18.48	1.07	0.27
0.15	64.60	-4.68	-59.04	-11.08	1.08	0.30
0.20	58.20	-4.16	-80.88	-5.56	1.15	0.35
0.25	57.36	-2.84	-97.36	-4.84	1.16	0.38
0.30	50.76	-2.16	-105.52	-2.88	1.23	0.44

als, including transition–metal oxides[270], HTSCs[276], Fe–based superconductors[277]; europium monochalcogenides[278], orbital–ordered noncollinear spinel MnV_2O_4[279], and Dirac magnon material Cu_3TeO_6[280]. We also use a constrained–orbital–hybridization method to provide theoretical insights into the various contributions[272] to the exchange interactions in hole doped $NdNiO_2$. To avoid the effect of the very narrow Nd–$4f$ bands, we shift the three occupied Nd–$4f$ orbitals downward while shifting the rest of the Nd–$4f$ band upward by using a constrained–orbital approach [272]. Since the obtained results do not depend on the magnitude of the shifts, we display the results with the Nd–$4f$ bands shifted by $\pm$2.0 Ry.

Similarly to previously reported band structure calculations for $LaNiO_2$[230, 239, 241, 244], there are two bands crossing the Fermi level in the LDA band structure of $NdNiO_2$, with one band primarily derived from the Ni–$3d_{x^2-y^2}$ orbital and the other consisting of predominantly Nd–$5d$ character. Just as with $LaNiO_2$[230, 239], there is a gap between Ni–$3d$ and O–$2p$ bands (around -3.5 eV). Moreover, Ni–O bond length in $NdNiO_2$ (1.96 $\AA$) is slightly larger than the Cu–O bond length in $CaCuO_2$ (1.92 $\AA$). Thus the bandwidth of the Ni–$3d_{x^2-y^2}$ band correspondingly smaller than that of the Cu–$3d_{x^2-y^2}$ band. While in both $NdNiO_2$ and $CaCuO_2$, the $3d_{3z^2-r^2}$ orbitals have very small dispersions along the $ZRAZ$ line, the dispersion of the Ni–$3d_{3z^2-r^2}$ state along ΓZ is considerably larger than that

Table 5.2: Calculated exchange interactions (in meV) for x=0.2 hole doped $NdNiO_2$, with Nd-5d shifted upward by various energies (in Ry).

Shift (Ry):	J_1	J_{z1}
0.05	64.28	-84.04
0.10	65.48	-83.76
0.50	69.68	-75.52
2.00	71.92	-78.96

of Cu–$3d_{3z^2-r^2}$. Moreover, compared to Cu–$3d_{3z^2-r^2}$, the Ni–$3d_{3z^2-r^2}$ band lies closer to the Fermi level. These two features are expected to significantly affect the magnetic behavior in the hole doped $NdNiO_2$.

We now perform the LDA+U calculation to examine magnetic exchange interactions in undoped $NdNiO_2$. Our results show that the exchange coupling is large for the nearest–neighbor J_1 within the NiO_2 plane. The sign of this term is AFM, and thus the NiO_2 layer shows a (π,π) spin ordering. There is some debate about the magnitude of the exchange interaction, with estimates ranging from much less than that of cuprates [246, 240, 267] to comparable to the value of exchange interaction in $CaCuO_2$[243, 268, 269]. Our calculated value of J_1 is 82.24 meV as referenced to the form of the Heisenberg Hamiltonian

$$H = \frac{1}{2}\sum_{ij} J_{ij}\mathbf{S}_i\mathbf{S}_j \tag{5.1}$$

with S=1/2. The estimate of J_1 =25 meV from the Raman scattering experiment of the two–magnon peak [267, 265] is significantly smaller. Recent resonance X–ray scattering experiments performed for trilayer nickelate $La_4Ni_3O_8$ report this value to be 69 meV[281]. The in–plane J_1 that we compute is only about 25% less than that found in $CaCuO_2$[276]. We attribute it to a smaller Ni–3d and O–2p hybridization and larger energy splitting between Ni–3d and O–2p as has previously been pointed out[230]. Consistent with the result of (π,π,0) spin ordering being slightly more energetically favorable than (π,π,π), our calculation produces a small out–of–plane FM exchange interaction, with nearest neighbor $J_{1z} = -3.4$

meV and second nearest neighbor $J_{2z} = -23$ meV, respectively. Our calculations reveal that the magnetic moment at the Ni site (0.97 μ_B), residing mostly in the $3d_{x^2-y^2}$ orbital, is much larger than that at Cu sites in HSTCs.

There exists a fairly flat band right at the Fermi level along the $ZRAZ$ line, in the band structure of the magnetic ground state configuration of $NdNiO_2$, as shown in Fig.5.1(a). This flat band has predominantly Ni–$3d_{3z^2-r^2}$ character, and plays an important role when hole doping is considered. The very small in–plane dispersion of the Ni–$3d_{3z^2-r^2}$ band can be understood as a consequence of the symmetry of the Ni–$3d_{3z^2-r^2}$ orbital, which can only weakly hybridize with the neighboring O–$2p$.

To examine the doping dependence we perform a series of hole–doped calculations, varying the number of holes per unit cell from 0.05 to 0.30 by using the virtual crystal approximation. These calculations show that the hole doping within this range does not significantly change the shape of the band structure apart from shifting the Fermi level downward. Regardless of the hole–doping concentration, the Ni–t_{2g} band is almost fully occupied and does not contribute to the magnetic moment. The magnetic moment of the Ni–$3d_{x^2-y^2}$ orbital is also unaffected by the hole doping. Instead, the holes preferentially occupy the flat Ni–$3d_{3z^2-r^2}$ band, and, as a result, the magnetic moment of this orbital increases with doping as shown in Table 5.1. Noting the considerable Ni–$3d_{3z^2-r^2}$ band dispersion along ΓZ, and the formation of magnetic moments in this orbital, one can expect the emergence of out–of–plane magnetic exchange interactions. This result has been confirmed by our linear response calculation. As shown in Table 5.1, hole doping significantly enhances the out–of–plane J_{z1}, while the in–plane J_1 remains mostly unaffected.

The $5d$ orbital is spatially very wide, and can have a crucial effect on the magnetic exchange interaction through $4f$–$5d$ hybridization, even though it is empty and located above the Fermi level[278]. In $NdNiO_2$, the Nd–$5d$ band appears at the Fermi level, making it important to understand the role of the Nd–$5d$ orbital in magnetic exchange interactions. We

address this issue by using a constrained–orbital–hybridization approach[272]. We perform the calculations with the Nd–5d band shifted upward by various values. Fig. 5.1(b) shows the band structure for the case where the Nd–5d band is shifted upward by 2 Ry. As one can see, the AFM insulating state emerges from this calculation for the undoped case, while hole doping vacates the Ni–3$d_{3z^2-r^2}$ band within $k_z = \pi/c$ plane.

Our calculation shows that both in–plane J_1 and out–of–plane J_{z1} exchange interactions are not sensitive to the position of the Nd–5d band as shown in Table 5.2, clearly indicating that the effect of this orbital on the magnetic exchange interactions is negligible. A similar calculation was performed for $LaNiO_2$ to further confirm these findings[275]. While the obtained values of the exchange interactions are slightly different, the key features discussed above are the same.

We illustrate the effect of increasing out–of–plane exchange interactions in doped $NdNiO_2$, using an antiferromagnetic Heisenberg model, Eq. (5.1). Its linear spin–wave dispersion is given by

$$\omega(\mathbf{q}) = S\sqrt{[J_{11}(\mathbf{q}) - J_{11}(0) + J_{12}(0)]^2 - [J_{12}(\mathbf{q})]^2}$$

where $J_{11}(\mathbf{q})/J_{12}(\mathbf{q})$ are the exchange interactions within the same/different sublattices. (A quantum correction factor $Z_c \approx 1.18$ which is sometimes used [276] in front of this formula is omitted here) We plot these dispersions in Fig. 5.2 for both undoped and 0.2 hole–doped $NdNiO_2$ in Fig. 5.2, along with those of $CaCuO_2$ for comparison[276]. We utilize our calculated exchange constants as a function of the wavevector for this purpose, and not their nearest neighbor fits shown in Table 5.1. This procedure fully accounts for the long–range effects of the interactions. Our model demonstrates some differences between the spin–wave dispersions of $NdNiO_2$ and $CaCuO_2$. Notably, the peak around $(\frac{1}{2}, 0, 0)$ is reduced in $NdNiO_2$ compared with $CaCuO_2$, as a consequence of the smaller in–plane exchange couplings, and

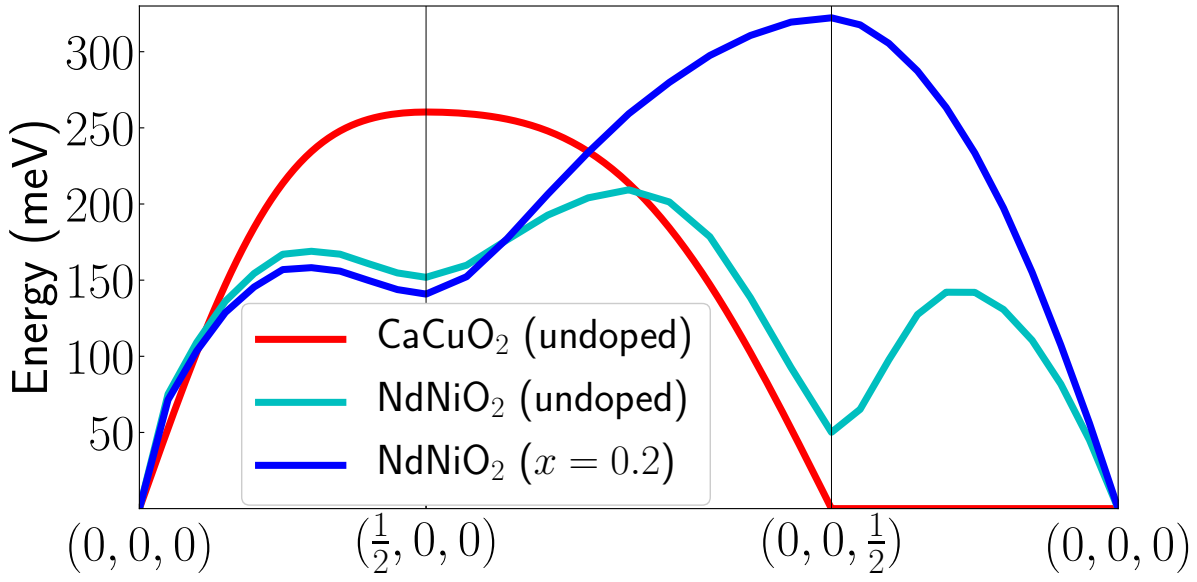

Figure 5.2: Calculated spin–wave dispersions for the undoped $NdNiO_2$ (cyan), and 0.2 hole-doped $NdNiO_2$ (blue), with U=6eV. For comparison, we also plot the results of $CaCuO_2$ (red)[276].

is largely unaffected by doping. In contrast, the out–of–plane exchange interactions strongly depend on doping, which can be seen in the changing dispersion along ΓZ. In undoped $NdNiO_2$, an out–of–plane J_{z2} dominates over the vanishing nearest neighbor J_{z1}. Doping amplifies J_{z1} while suppressing J_{z2}, resulting in the disappearance of the valley at $(0, 0, 1/2)$ in the dispersion. Thus, in contrast with HTSCs, our calculation of J's here predicts a strongly doping dependent resonance that could in principle be observed in neutron experiments.

5.3 Two–band model

A minimal model for the electronic structure of $NdNiO_2$ that emerges from the present study should involve Ni–$3d_{x^2-y^2}$ and Ni–$3d_{3z^2-r^2}$ orbitals only. Their role has already been emphasized in many recent works[236]–[263] and, as we argue here, their importance is based on sensitivity of magnetic excitations to the position of various orbitals. The parameters of the model can be obtained by tracing the orbital character of these states from the non–

magnetic LDA calculation. We show this in red for Ni–$3d_{x^2-y^2}$ and in green for Ni–$3d_{3z^2-r^2}$ in Fig. 5.3(a). The derived two–band tight–binding model is illustrated in Fig. 5.3(b). In the large U limit, such model at a quarter filling by holes (3 electron filling) is expected to exhibit a Mott insulator for $3d_{x^2-y^2}$ band, with the lower Hubbard band placed below $3d_{3z^2-r^2}$ state. Its antiferromagnetic solution in the Hartree–Fock approximation will result in the band structure very similar to the LDA+U result shown in Fig. 5.1(b), which also assumes that the t_{2g} states of Ni, although appear in the same energy range, are apparently irrelevant. According to our LDA+U calculation with $U \sim 4$ eV, doping sends the holes primarily to the $3d_{3z^2-r^2}$ state promoting interorbital triplets. This is seen in Fig. 5.1(b) where the Fermi level shifting downwards unoccupies the $3d_{3z^2-r^2}$ band in $k_z = \pi/c$ plane which explains doping dependence of the orbital occupancies shown in Table 5.1.

The described picture should however be contrasted to the genuine strong correlation effect that prompts to consider an additional hole to be injected into either Ni $x^2 - y^2$ or $3z^2 - r^2$ orbital resulting either in an intraorbital singlet or interorbital triplet. This is different from cuprates, where holes end up in low–lying O 2p band forming Zhang–Rice singlet states[223]. Here, it is not the relation of Hubbard U to the crystal field splitting Δ between $x^2 - y^2$ and $3z^2 - r^2$ levels but the competition of the Hund's rule J_H and Δ which should be examined to understand the origin of the two–hole state in the doped case[246, 247, 250, 251, 252]. To illustrate the proximity of both (S=0 and S=1) solutions, a simple diagonalization of the $3d^8$ shell with U=6 eV and our deduced from Fig. 5.1(b) crystal field splitting Δ=2.2 eV reveals that the lowest energy state is S=0 for $J_H < 0.9$ eV, and S=1 otherwise. This value is well within the range of generally assumed Hund's rule exchange energies for transition metal oxides and highlights a delicate balance in extracting the two–hole ground state configuration.

Although a number of full–fledge multiorbital LDA+DMFT calculations have been recently carried out to understand the many–body physics of doped $NdNiO_2$[247, 250, 260],

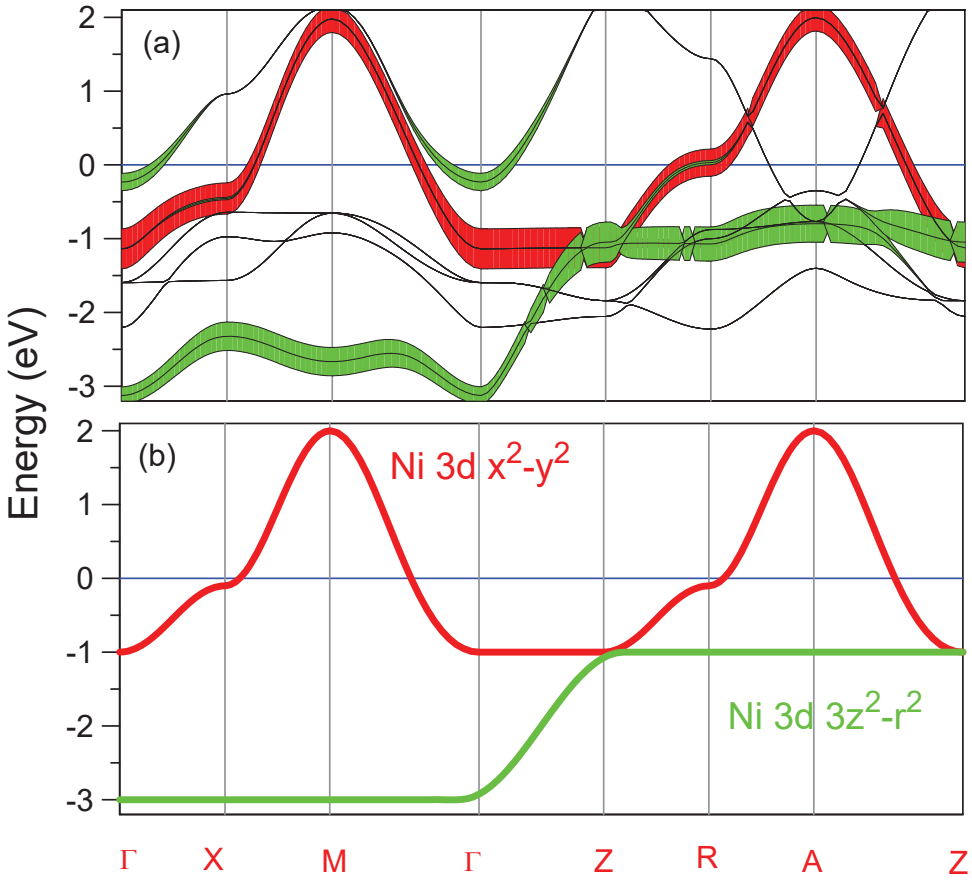

Figure 5.3: (a) Non–magnetic LDA band structure of $NdNiO_2$ with the orbital character of Ni-$3d_{x^2-y^2}$ and Ni-$3d_{3z^2-r^2}$ states shown in red and green, respectively. (b) The corresponding two-band tight–binding model[275].

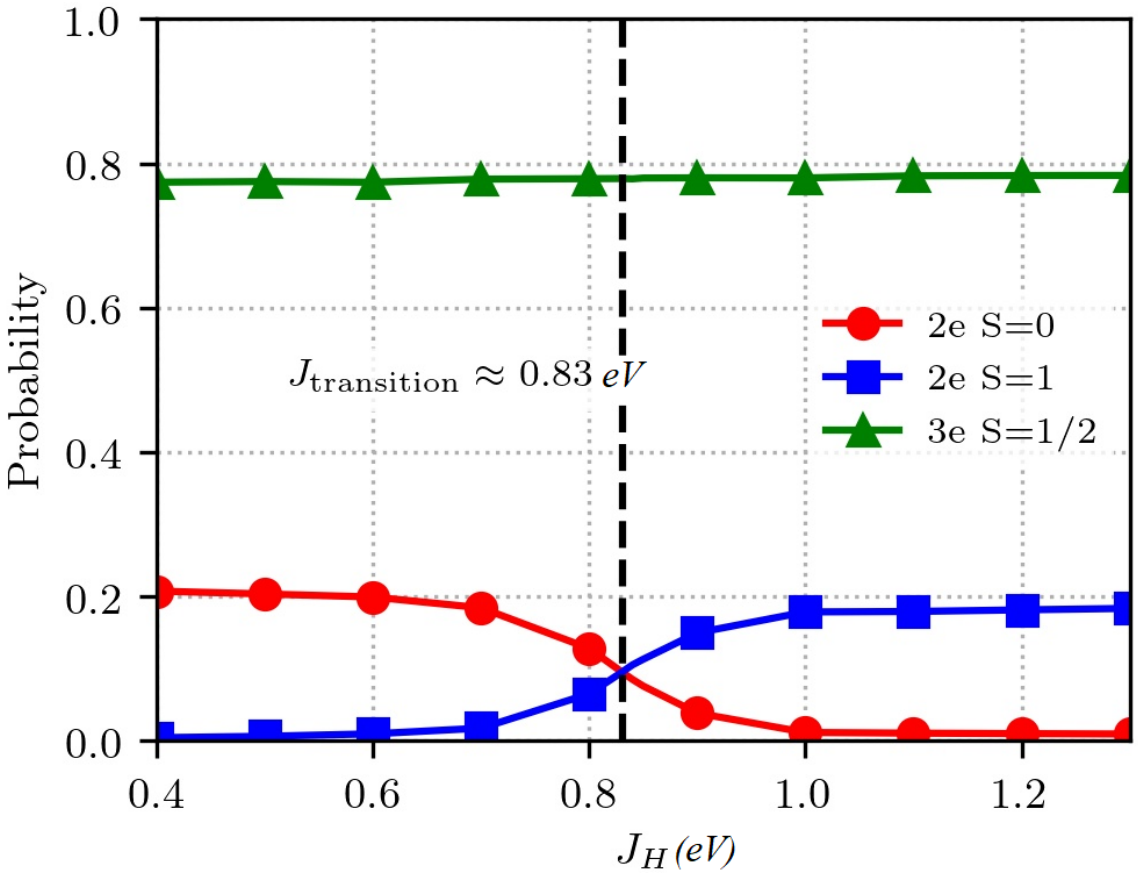

Figure 5.4: Calculated probabilites for the three electron S=1/2 and two–electron S=0 and S=1 states as a function of Hund's coupling J_H using Dynamical Mean Field Theory and Continious Time Quantum Monte Carlo Method for the two–band model of $NdNiO_2$ corresponding to doping by 0.2 holes (filling by 2.8 electrons in the model). An inverse temperature of $\beta = 40$ is used in the calculations.

a strong sensitivity of the solution to the input parameters, such as J_H, is expected. This has been already highlighted in the earlier work simulating two semicircular densities of states with the crystal field splitting as a parameter [252]. To gain a further qualitative insight, here we study our derived two–band model using Dynamical Mean Field Theory[67] and Continuous Time Quantum Monte Carlo method[282]. The parameters U=6 eV and Δ=2.2 eV are fixed while J_H is adjusted. The undoped case of Ni $3d^9$ S=1/2 state corresponds to the electronic filling equal to 3 in this model, where we easily recover a paramagnetic Mott insulating state with the gap of the order of U that opens up in the $x^2 - y^2$ band and with the $3z^2 - r^2$ states that remain completely occupied. Doping this model with 0.2 holes (filling by 2.8 electrons) results in finite probability to find either S=0 or S=1 states in addition to S=1/2 that depends on J_H. These probabilities extracted from the Quantum Monte Carlo simulation are shown in Fig. 5.4 very close to our earlier estimate of 0.9 eV.

Our results for the **k**–resolved spectral functions are summarized in Fig. 5.5, where a comparative study is presented for the two quasiparticle band structures corresponding to S=0 state (J_H is set to 0.6 eV, Fig. 5.5(a)) and to S=1 state (J_H is set to 1 eV, Fig. 5.5(b)). One can see from the calculated spectrum for J_H =0.6 eV that the $3z^2 - r^2$ state remains completely occupied while the doping primarily affects the $x^2 - y^2$ band which now shows a typical for DMFT three–peak structure with the two Hubbard bands appearing below and above the Fermi level and a renormalized quasiparticle band that crosses E_F. The k dispersion for all three features is similar to the original dispersion of the $x^2 - y^2$ band.

A different picture emerges from the calculation with $J_H = 1$ eV shown in Fig. 5.5(b). In this case, renormalized quasiparticles of the $3z^2 - r^2$ character appear at the Fermi level which illustrate the formation of the interorbital triplet states. A very strong peak in the quasiparticle density of state is expected to be present at E_F due to the non–dispersive portion of the $3z^2 - r^2$ band within the ZRA plane. At the same time, the $x^2 - y^2$ band does not develop a three–peak structure and is characterized by the two Hubbard bands as in

the undoped case. A very similar behavior has been already predicted in a recent work[251] where it was termed as the "Kondo resonance" property, carried by the Ni-$3z^2-r^2$ character.

Our previous LDA+DMFT calculations [260] performed for $J_H = 0.95$ eV are in somewhat agreement with this result although the appearance of the flat band was detected by us earlier only at a higher doping (˜0.4). The origin of this discrepancy may lie in a more complex interplay between crystal fields and double counting effects in a self–consistent multiorbital simulation or in an analytical continuation of the QMC derived spectral functions resulting in a smaller and/or more broadened spectral weight as compared to the result of the model. We have additionally checked the probabilities of various spin states within LDA+DMFT and they are mostly in line with what we observe in Fig. 5.4.

Since the Hund's coupling J_H of 0.8 to 0.9 eV is well within the range of commonly accepted values, we cannot make a definite conclusion about whether S=0 or S=1 scenario is realized for doped nickelates. However, possible future angle–resolved photoemission (ARPES) experiments may provide important insight since as illustrated by our calculations the quasiparticle band structure is very different between the two cases. Furthermore, while ARPES spectra in the hole–doped HTSCs show waterfall–like behavior[283], we do not expect waterfalls to appear here due to a lack of oxygen states at energies close to E_F and associated physics responsible for the formation of the low energy states[284].

In conclusion, using the LDA+U method, we have calculated magnetic exchange interactions for the doped $NdNiO_2$ novel superconductor. We find that the parent compound is mostly two–dimensional, with large nearest neighbor in–plane, and small out–of–plane exchange interactions. Upon doping, the out–of–plane coupling J_{z1} was found to increase dramatically, while the in–plane J_1 is almost unchanged. To clarify the origin of these trends, we analyzed the symmetry of the holes induced by doping which were found to be primarily of the $3d_{3z^2-r^2}$ character promoting the formation of interorbital triplet as Ni $3d^8$ ground state configuration. We also investigated the role of the Nd–$5d$ states, which con-

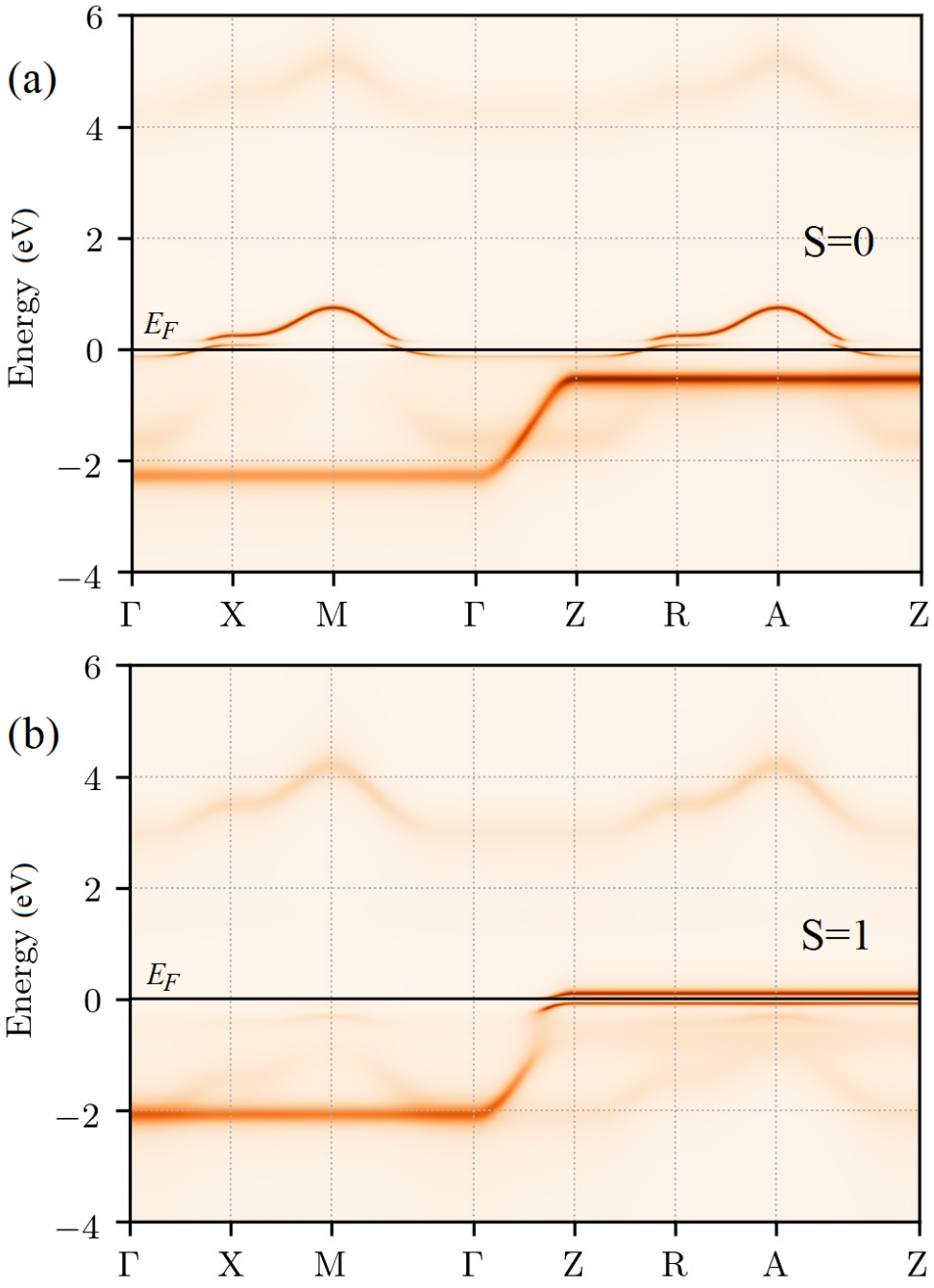

Figure 5.5: Quasiparticle band structures of the two– band model of $NdNiO_2$ obtained by Dynamical Mean Field Theory and Continious Time Quantum Monte Carlo Method for the doping level of 0.2 holes: (a) Calculation for Hund's coupling $J_H = 0.6$ eV that corresponds to S=0 two–hole state; (b) Calculation for $J_H = 1$ eV corresponding to S=1 two-hole state. An inverse temperature $\beta = 40$ is used for the calculations.

tribute substantially to the Fermi surface of $NdNiO_2$. Shifting this band upward using a constrained–orbital–hybridization method has little effect on exchange interactions, which leads us to conclude that Nd–$5d$ states have negligible effect on the spin fluctuations and the superconductivity in $NdNiO_2$. A minimal two–band model with active Ni–$3d_{x^2-y^2}$ and Ni–$3d_{3z^2-r^2}$ orbitals has been further studied with DMFT to reveal an underlying Mott insulating state which upon doping selects either S=0 and S=1 two–hole states depending on the Hund's coupling in the range of its commonly accepted values 0.8 to 0.9 eV. Should S=1 state be valid, we rely on our LDA+U result to predict that upon doping the spin susceptibility gains three dimensionality as it gets enhanced along ΓZ. This can be readily observed in neutron experiments and can be one way to probe the two–hole configuration. We also rely on our DMFT result to predict a formation of a strong quasiparticle peak at the Fermi level detectable by ARPES experiments. A small anisotropy in H_{c2} was indeed discovered very recently [285] illustrating the three–dimensional nature of $NdNiO_2$ which starkly contrasts with the two–dimensional superconductivity in HTSCs. At the same time, most recent x–ray absorption spectroscopy (XAS) and resonant inelastic x-ray scattering (RIXS) experiments are found to be consistent with a d^8 spin singlet state [286]. These results should be important in future studies of nickelate superconductors.

Bibliography

[1] M. Z. Hasan and C. L. Kane. Colloquium: Topological insulators. *Rev. Mod. Phys.*, 82:3045–3067, Nov 2010.

[2] D. J. Thouless, M. Kohmoto, M. P. Nightingale, and M. den Nijs. Quantized Hall Conductance in a Two-Dimensional Periodic Potential. *Phys. Rev. Lett.*, 49:405–408, Aug 1982.

[3] Xiao-Liang Qi, Yong-Shi Wu, and Shou-Cheng Zhang. General theorem relating the bulk topological number to edge states in two-dimensional insulators. *Phys. Rev. B*, 74:045125, Jul 2006.

[4] Liang Fu and C. L. Kane. Time reversal polarization and a Z_2 adiabatic spin pump. *Phys. Rev. B*, 74:195312, Nov 2006.

[5] C. L. Kane and E. J. Mele. Z_2 Topological Order and the Quantum Spin Hall Effect. *Phys. Rev. Lett.*, 95:146802, Sep 2005.

[6] C. L. Kane and E. J. Mele. Quantum Spin Hall Effect in Graphene. *Phys. Rev. Lett.*, 95:226801, Nov 2005.

[7] Liang Fu and C. L. Kane. Topological insulators with inversion symmetry. *Phys. Rev. B*, 76:045302, Jul 2007.

[8] F. D. M. Haldane. Berry Curvature on the Fermi Surface: Anomalous Hall Effect as a Topological Fermi-Liquid Property. *Phys. Rev. Lett.*, 93:206602, Nov 2004.

[9] Di Xiao, Ming-Che Chang, and Qian Niu. Berry phase effects on electronic properties. *Rev. Mod. Phys.*, 82:1959–2007, Jul 2010.

[10] Xiao-Liang Qi, Taylor L. Hughes, and Shou-Cheng Zhang. Topological field theory of time-reversal invariant insulators. *Phys. Rev. B*, 78:195424, Nov 2008.

[11] Naoto Nagaosa, Jairo Sinova, Shigeki Onoda, A. H. MacDonald, and N. P. Ong. Anomalous Hall effect. *Rev. Mod. Phys.*, 82:1539–1592, May 2010.

[12] B. Andrei Bernevig, Taylor L. Hughes, and Shou-Cheng Zhang. Quantum Spin Hall Effect and Topological Phase Transition in HgTe Quantum Wells. *Science*, 314(5806):1757–1761, 2006.

[13] D. N. Sheng, Z. Y. Weng, L. Sheng, and F. D. M. Haldane. Quantum spin-hall effect and topologically invariant chern numbers. *Phys. Rev. Lett.*, 97:036808, Jul 2006.

[14] N. P. Armitage, E. J. Mele, and Ashvin Vishwanath. Weyl and Dirac semimetals in three-dimensional solids. *Rev. Mod. Phys.*, 90:015001, Jan 2018.

[15] S. M. Young, S. Zaheer, J. C. Y. Teo, C. L. Kane, E. J. Mele, and A. M. Rappe. Dirac Semimetal in Three Dimensions. *Phys. Rev. Lett.*, 108:140405, Apr 2012.

[16] A. A. Burkov and Leon Balents. Weyl Semimetal in a Topological Insulator Multilayer. *Phys. Rev. Lett.*, 107:127205, Sep 2011.

[17] A. A. Zyuzin, Si Wu, and A. A. Burkov. Weyl semimetal with broken time reversal and inversion symmetries. *Phys. Rev. B*, 85:165110, Apr 2012.

[18] Gábor B. Halász and Leon Balents. Time-reversal invariant realization of the Weyl semimetal phase. *Phys. Rev. B*, 85:035103, Jan 2012.

[19] G. E. Volovik. Zeros in the fermion spectrum in superfluid systems as diabolical points. *JETP Lett.*, 46:98, 1987.

[20] A. A. Burkov, M. D. Hook, and Leon Balents. Topological nodal semimetals. *Phys. Rev. B*, 84:235126, Dec 2011.

[21] Xiangang Wan, Ari M. Turner, Ashvin Vishwanath, and Sergey Y. Savrasov. Topological semimetal and Fermi-arc surface states in the electronic structure of pyrochlore iridates. *Phys. Rev. B*, 83:205101, May 2011.

[22] Chen Fang, Hongming Weng, Xi Dai, and Zhong Fang. Topological nodal line semimetals. *Chinese Physics B*, 25(11):117106, nov 2016.

[23] Chen Fang, Yige Chen, Hae-Young Kee, and Liang Fu. Topological nodal line semimetals with and without spin-orbital coupling. *Phys. Rev. B*, 92:081201, Aug 2015.

[24] Bohm-Jung Yang, Troels Arnfred Bojesen, Takahiro Morimoto, and Akira Furusaki. Topological semimetals protected by off-centered symmetries in nonsymmorphic crystals. *Phys. Rev. B*, 95:075135, Feb 2017.

[25] Rui Yu, Hongming Weng, Zhong Fang, Xi Dai, and Xiao Hu. Topological Node-Line Semimetal and Dirac Semimetal State in Antiperovskite Cu_3PdN. *Phys. Rev. Lett.*, 115:036807, Jul 2015.

[26] Yongping Du, Feng Tang, Di Wang, Li Sheng, Er-jun Kan, Chun-Gang Duan, Sergey Y. Savrasov, and Xiangang Wan. CaTe: a new topological node-line and Dirac semimetal. *npj Quantum Materials*, 2(1):3, Jan 2017.

[27] H.B. Nielsen and Masao Ninomiya. The Adler-Bell-Jackiw anomaly and Weyl fermions in a crystal. *Physics Letters B*, 130(6):389–396, 1983.

[28] F. D. M. Haldane. Attachment of Surface "Fermi Arcs" to the Bulk Fermi Surface: "Fermi-Level Plumbing" in Topological Metals, 2014.

[29] Kai-Yu Yang, Yuan-Ming Lu, and Ying Ran. Quantum Hall effects in a Weyl semimetal: Possible application in pyrochlore iridates. *Phys. Rev. B*, 84:075129, Aug 2011.

[30] Ari M. Turner and Ashvin Vishwanath. Beyond Band Insulators: Topology of Semimetals and Interacting Phases, 2013.

[31] Pierre Delplace, Jian Li, and David Carpentier. Topological Weyl semi-metal from a lattice model. *EPL (Europhysics Letters)*, 97(6):67004, mar 2012.

[32] Giacomo Resta, Shu-Ting Pi, Xiangang Wan, and Sergey Y. Savrasov. High surface conductivity of Fermi-arc electrons in Weyl semimetals. *Phys. Rev. B*, 97:085142, Feb 2018.

[33] Timothy M. McCormick, Itamar Kimchi, and Nandini Trivedi. Minimal models for topological weyl semimetals. *Phys. Rev. B*, 95:075133, Feb 2017.

[34] A. A. Burkov. Anomalous hall effect in weyl metals. *Phys. Rev. Lett.*, 113:187202, Oct 2014.

[35] Vsevolod Ivanov and Sergey Y. Savrasov. Monopole mining method for high-throughput screening for Weyl semimetals. *Phys. Rev. B*, 99:125124, Mar 2019.

[36] Vsevolod Ivanov, Xiangang Wan, and Sergey Y. Savrasov. Renormalized quasiparticles, topological monopoles, and superconducting line nodes in heavy-fermion CeTX_3 compounds. *Phys. Rev. B*, 103:L041112, Jan 2021.

[37] Vsevolod Ivanov, Xiangang Wan, and Sergey Y. Savrasov. Topological Insulator-to-Weyl Semimetal Transition in Strongly Correlated Actinide System UNiSn. *Phys. Rev. X*, 9:041055, Dec 2019.

[38] Takahiro Fukui and Yasuhiro Hatsugai. Quantum Spin Hall Effect in Three Dimensional Materials: Lattice Computation of Z2 Topological Invariants and Its Application to Bi and Sb. *Journal of the Physical Society of Japan*, 76(5):053702, 2007.

[39] Takahiro Fukui, Yasuhiro Hatsugai, and Hiroshi Suzuki. Chern Numbers in Discretized Brillouin Zone: Efficient Method of Computing (Spin) Hall Conductances. *Journal of the Physical Society of Japan*, 74(6):1674–1677, 2005.

[40] Hsin Lin, L. Andrew Wray, Yuqi Xia, Suyang Xu, Shuang Jia, Robert J. Cava, Arun Bansil, and M. Zahid Hasan. Half-Heusler ternary compounds as new multifunctional experimental platforms for topological quantum phenomena. *Nature Materials*, 9(7):546–549, Jul 2010.

[41] Stanislav Chadov, Xiaoliang Qi, Jürgen Kübler, Gerhard H. Fecher, Claudia Felser, and Shou Cheng Zhang. Tunable multifunctional topological insulators in ternary Heusler compounds. *Nature Materials*, 9(7):541–545, Jul 2010.

[42] M. G. Vergniory, L. Elcoro, Claudia Felser, Nicolas Regnault, B. Andrei Bernevig, and Zhijun Wang. A complete catalogue of high-quality topological materials. *Nature*, 566(7745):480–485, Feb 2019.

[43] Hoi Chun Po, Ashvin Vishwanath, and Haruki Watanabe. Symmetry-based indicators of band topology in the 230 space groups. *Nature Communications*, 8(1):50, Jun 2017.

[44] Jorrit Kruthoff, Jan de Boer, Jasper van Wezel, Charles L. Kane, and Robert-Jan Slager. Topological Classification of Crystalline Insulators through Band Structure Combinatorics. *Phys. Rev. X*, 7:041069, Dec 2017.

[45] Timothy H. Hsieh, Hsin Lin, Junwei Liu, Wenhui Duan, Arun Bansil, and Liang Fu. Topological crystalline insulators in the SnTe material class. *Nature Communications*, 3(1):982, Jul 2012.

[46] Hongming Weng, Jianzhou Zhao, Zhijun Wang, Zhong Fang, and Xi Dai. Topological Crystalline Kondo Insulator in Mixed Valence Ytterbium Borides. *Phys. Rev. Lett.*, 112:016403, Jan 2014.

[47] Su-Yang Xu, Ilya Belopolski, Nasser Alidoust, Madhab Neupane, Guang Bian, Chenglong Zhang, Raman Sankar, Guoqing Chang, Zhujun Yuan, Chi-Cheng Lee, Shin-Ming Huang, Hao Zheng, Jie Ma, Daniel S. Sanchez, BaoKai Wang, Arun Bansil, Fangcheng Chou, Pavel P. Shibayev, Hsin Lin, Shuang Jia, and M. Zahid Hasan. Discovery of a Weyl fermion semimetal and topological Fermi arcs. *Science*, 349(6248):613–617, 2015.

[48] B. Q. Lv, H. M. Weng, B. B. Fu, X. P. Wang, H. Miao, J. Ma, P. Richard, X. C. Huang, L. X. Zhao, G. F. Chen, Z. Fang, X. Dai, T. Qian, and H. Ding. Experimental Discovery of Weyl Semimetal TaAs. *Phys. Rev. X*, 5:031013, Jul 2015.

[49] Su-Yang Xu, Nasser Alidoust, Guoqing Chang, Hong Lu, Bahadur Singh, Ilya Belopolski, Daniel S. Sanchez, Xiao Zhang, Guang Bian, Hao Zheng, Marious-Adrian Husanu, Yi Bian, Shin-Ming Huang, Chuang-Han Hsu, Tay-Rong Chang, Horng-Tay Jeng, Arun Bansil, Titus Neupert, Vladimir N. Strocov, Hsin Lin, Shuang Jia, and M. Zahid Hasan. Discovery of Lorentz-violating Type-II Weyl fermions in LaAlGe. *Science Advances*, 3(6), 2017.

[50] Lunan Huang, Timothy M. McCormick, Masayuki Ochi, Zhiying Zhao, Michi-To Suzuki, Ryotaro Arita, Yun Wu, Daixiang Mou, Huibo Cao, Jiaqiang Yan, Nandini Trivedi, and Adam Kaminski. Spectroscopic evidence for a Type-II Weyl semimetallic state in $MoTe_2$. *Nature Materials*, 15(11):1155–1160, Nov 2016.

[51] Guoqing Chang, Su-Yang Xu, Daniel S. Sanchez, Shin-Ming Huang, Chi-Cheng Lee, Tay-Rong Chang, Guang Bian, Hao Zheng, Ilya Belopolski, Nasser Alidoust, Horng-Tay Jeng, Arun Bansil, Hsin Lin, and M. Zahid Hasan. A strongly robust Type-II Weyl fermion semimetal state in Ta_3S_2. *Science Advances*, 2(6), 2016.

[52] Yongping Du, Er-jun Kan, Hu Xu, Sergey Y. Savrasov, and Xiangang Wan. Turning copper metal into a Weyl semimetal. *Phys. Rev. B*, 97:245104, Jun 2018.

[53] Dominik Gresch, Gabriel Autès, Oleg V. Yazyev, Matthias Troyer, David Vanderbilt, B. Andrei Bernevig, and Alexey A. Soluyanov. Z2Pack: Numerical implementation of hybrid Wannier centers for identifying topological materials. *Phys. Rev. B*, 95:075146, Feb 2017.

[54] Tiantian Zhang, Yi Jiang, Zhida Song, He Huang, Yuqing He, Zhong Fang, Hongming Weng, and Chen Fang. Catalogue of topological electronic materials. *Nature*, 566(7745):475–479, Feb 2019.

[55] Feng Tang, Hoi Chun Po, Ashvin Vishwanath, and Xiangang Wan. Comprehensive search for topological materials using symmetry indicators. *Nature*, 566(7745):486–489, Feb 2019.

[56] Zhong Fang, Naoto Nagaosa, Kei S. Takahashi, Atsushi Asamitsu, Roland Mathieu, Takeshi Ogasawara, Hiroyuki Yamada, Masashi Kawasaki, Yoshinori Tokura, and Kiyoyuki Terakura. The Anomalous Hall Effect and Magnetic Monopoles in Momentum Space. *Science*, 302(5642):92–95, 2003.

[57] Hendrik J. Monkhorst and James D. Pack. Special points for Brillouin-zone integrations. *Phys. Rev. B*, 13:5188–5192, Jun 1976.

[58] O. Jepsen and O. K. Andersen. No error in the tetrahedron integration scheme. *Phys. Rev. B*, 29:5965–5965, May 1984.

[59] S. Yu. Savrasov. Linear response calculations of lattice dynamics using muffin-tin basis sets. *Phys. Rev. Lett.*, 69:2819–2822, Nov 1992.

[60] J. E. Moore and L. Balents. Topological invariants of time-reversal-invariant band structures. *Phys. Rev. B*, 75:121306, Mar 2007.

[61] S. Y. Savrasov. Linear-response theory and lattice dynamics: A muffin-tin-orbital approach. *Phys. Rev. B*, 54:16470–16486, Dec 1996.

[62] John P. Perdew, Kieron Burke, and Matthias Ernzerhof. Generalized Gradient Approximation Made Simple. *Phys. Rev. Lett.*, 77:3865–3868, Oct 1996.

[63] Wanxiang Feng, Jun Wen, Jinjian Zhou, Di Xiao, and Yugui Yao. First-principles calculation of Z2 topological invariants within the FP-LAPW formalism. *Computer Physics Communications*, 183(9):1849–1859, 2012.

[64] P. Villars, K. Cenzual, and R. Gladyshevskii. *Handbook of Inorganic Substances*. De Gruyter, 2015.

[65] Ai Yamakage, Youichi Yamakawa, Yukio Tanaka, and Yoshihiko Okamoto. Line-Node Dirac Semimetal and Topological Insulating Phase in Noncentrosymmetric Pnictides CaAgX (X = P, As). *Journal of the Physical Society of Japan*, 85(1):013708, 2016.

[66] Yan Sun, Qing-Ze Wang, Shu-Chun Wu, Claudia Felser, Chao-Xing Liu, and Binghai Yan. Pressure-induced topological insulator in NaBaBi with right-handed surface spin texture. *Phys. Rev. B*, 93:205303, May 2016.

[67] G. Kotliar, S. Y. Savrasov, K. Haule, V. S. Oudovenko, O. Parcollet, and C. A. Marianetti. Electronic structure calculations with dynamical mean-field theory. *Rev. Mod. Phys.*, 78:865–951, Aug 2006.

[68] Ziming Zhu, Georg W. Winkler, QuanSheng Wu, Ju Li, and Alexey A. Soluyanov. Triple Point Topological Metals. *Phys. Rev. X*, 6:031003, Jul 2016.

[69] Alexey A. Soluyanov, Dominik Gresch, Zhijun Wang, QuanSheng Wu, Matthias Troyer, Xi Dai, and B. Andrei Bernevig. Type-II Weyl semimetals. *Nature*, 527(7579):495–498, Nov 2015.

[70] Rainer Kraft, Martin Valldor, Daniel Kurowski, Rolf-Dieter Hoffmann, and Rainer Pöttgen. Ternary Indides REMgIn (RE = Y, La–Nd, Sm, Gd–Tm, Lu). Synthesis, Structure and Magnetic Properties. *Zeitschrift für Naturforschung B*, 59(5):513–518, 2004.

[71] Brendan Gibson, Rainer Pöttgen, Reinhard K. Kremer, Arndt Simon, and Kurt R.A. Ziebeck. Ternary germanides LnAgGe (Ln = Y, Sm, Gd–Lu) with ordered Fe2P-type structure. *Journal of Alloys and Compounds*, 239(1):34–40, 1996.

[72] Axel Czybulka, Günter Steinberg, and Hans-Uwe Schuster. Darstellung und Struktur ternärer Silizide und Germanide des Lithiums mit den Seltenen Erden Y und Gd im Fe2P-Typ / Preparation and Crystal Structure of Ternary Silicides and Germanides of Lithium with the Rare-Earth-Metals Y and Gd in the Fe2P-Type Structure. *Zeitschrift für Naturforschung B*, 34(8):1057–1058, 1979.

[73] L.D. Gulay. Crystal structure of RAgPb (R=Y, Er, Tm, Lu) compounds. *Journal of Alloys and Compounds*, 314(1):219–223, 2001.

[74] Igor Savysyuk, Oleh Shcherban, Nataliya Semuso, Roman Gladyshevskii, and Evgen Gladyshevskii. The {Y, Pr}–Ag–Si systems: isothermal sections and crystal structures. *Chem. Met. Alloys*, 5:103–112, 2012.

[75] G. P. Meisner and H. C. Ku. The superconductivity and structure of equiatomic ternary transition metal pnictides. *Applied Physics A*, 31(4):201–212, Aug 1983.

[76] Rainer Kraft and Rainer Pöttgen. Ternary Thallides REMgTl (Re = Y, La – Nd, Sm, Gd – Tm, Lu). *Zeitschrift für Naturforschung B*, 60(3):265–270, 2005.

[77] Dirk Johrendt and Albrecht Mewis. Darstellung und kristallstrukturen der verbindungen SEPdAs (SE = La–Lu). *Journal of Alloys and Compounds*, 183:210–223, 1992.

[78] G.P. Meisner, H.C. Ku, and H. Barz. Superconducting equiatomic ternary transition metal arsenides. *Materials Research Bulletin*, 18(8):983–991, 1983.

[79] Roman Demchyna and Yurii Prots and Ulrich Schwarz. Crystal structures of titanium palladium germanium, tipdge, two polymorphic modifications. *Zeitschrift für Kristallographie - New Crystal Structures*, 222(3):173–174, 2007.

[80] Mme Roy-Montreuil, B. Deyris, A. Michel, A. Rouault, P. l'Héritier, A. Nylund, J.P. Sénateur, and R. Fruchart. Nouveaux composes ternaires MM′P et MM′As interactions metalliques et structures. *Materials Research Bulletin*, 7(8):813–826, 1972.

[81] Xiaochun Huang, Lingxiao Zhao, Yujia Long, Peipei Wang, Dong Chen, Zhanhai Yang, Hui Liang, Mianqi Xue, Hongming Weng, Zhong Fang, Xi Dai, and Genfu Chen. Observation of the Chiral-Anomaly-Induced Negative Magnetoresistance in 3D Weyl Semimetal TaAs. *Phys. Rev. X*, 5:031023, Aug 2015.

[82] R. Settai, Y. Okuda, I. Sugitani, Y. Ōnuki, T. D. Matsuda, Y. Haga, and H Harima. Non-Centrosymmetric Heavy Fermion Superconductivity In $CeCoGe_3$. *International Journal of Modern Physics B*, 21(18n19):3238–3245, 2007.

[83] N. Kimura, K. Ito, K. Saitoh, Y. Umeda, H. Aoki, and T. Terashima. Pressure-Induced Superconductivity in Noncentrosymmetric Heavy-Fermion $CeRhSi_3$. *Phys. Rev. Lett.*, 95:247004, Dec 2005.

[84] F. Honda, I. Bonalde, K. Shimizu, S. Yoshiuchi, Y. Hirose, T. Nakamura, R. Settai, and Y. Ōnuki. Pressure-induced superconductivity and large upper critical field in the noncentrosymmetric antiferromagnet $CeIrGe_3$. *Phys. Rev. B*, 81:140507, Apr 2010.

[85] Ichiro Sugitani, Yusuke Okuda, Hiroaki Shishido, Tsutomu Yamada, Arumugam Thamizhavel, Etsuji Yamamoto, Tatsuma D. Matsuda, Yoshinori Haga, Tetsuya Takeuchi, Rikio Settai, and Yoshichika Ōnuki. Pressure-Induced Heavy-Fermion Superconductivity in Antiferromagnet $CeIrSi_3$ without Inversion Symmetry. *Journal of the Physical Society of Japan*, 75(4):043703, 2006.

[86] Honghong Wang, Jing Guo, Eric D. Bauer, Vladimir A. Sidorov, Hengcan Zhao, Jiahao Zhang, Yazhou Zhou, Zhe Wang, Shu Cai, Ke Yang, Aiguo Li, Xiaodong Li, Yanchun Li, Peijie Sun, Yi-feng Yang, Qi Wu, Tao Xiang, J. D. Thompson, and Liling Sun. Superconductivity in pressurized $CeRhGe_3$ and related noncentrosymmetric compounds. *Phys. Rev. B*, 97:064514, Feb 2018.

[87] Tomoya Kawai, Miho Nakashima, Yusuke Okuda, Hiroaki Shishido, Tetsuya Shimoda, Tatsuma D. Matsuda, Yoshinori Haga, Tetsuya Takeuchi, Masato Hedo, Yoshiya Uwatoko, Rikio Settai, and Yoshichika Ōnuki. Pressure Effect of Electronic States in Antiferromagnets $CeTX_3$ (T: Transition Metal, X: Si and Ge). *Journal of the Physical Society of Japan*, 76(Suppl.A):166–167, 2007.

[88] Rikio Settai, Yuichiro Miyauchi, Tetsuya Takeuchi, Florence Lévy, Ilya Sheikin, and Yoshichika Ōnuki. Huge Upper Critical Field and Electronic Instability in Pressure-induced Superconductor $CeIrSi_3$ without Inversion Symmetry in the Crystal Structure. *Journal of the Physical Society of Japan*, 77(7):073705, 2008.

[89] N. Kimura, K. Ito, H. Aoki, S. Uji, and T. Terashima. Extremely High Upper Critical Magnetic Field of the Noncentrosymmetric Heavy Fermion Superconductor $CeRhSi_3$. *Phys. Rev. Lett.*, 98:197001, May 2007.

[90] Hsin-Hua Lai, Sarah E. Grefe, Silke Paschen, and Qimiao Si. Weyl–Kondo semimetal in heavy-fermion systems. *Proceedings of the National Academy of Sciences*, 115(1):93–97, 2018.

[91] Tomoya Kawai, Hiroshi Muranaka, Marie-Aude Measson, Tetsuya Shimoda, Yusuke Doi, Tatsuma D. Matsuda, Yoshinori Haga, Georg Knebel, Gérard Lapertot, Dai Aoki, Jacques Flouquet, Tetsuya Takeuchi, Rikio Settai, and Yoshichika Ōnuki. Magnetic and Superconducting Properties of $CeTX_3$ (T: Transition Metal and X: Si and Ge) with Non-centrosymmetric Crystal Structure. *Journal of the Physical Society of Japan*, 77(6):064716, 2008.

[92] A. D. Hillier, D. T. Adroja, P. Manuel, V. K. Anand, J. W. Taylor, K. A. McEwen, B. D. Rainford, and M. M. Koza. Muon spin relaxation and neutron scattering investigations of the noncentrosymmetric heavy-fermion antiferromagnet $CeRhGe_3$. *Phys. Rev. B*, 85:134405, Apr 2012.

[93] V. K. Pecharsky, O.-B. Hyun, and K. A. Gschneidner. Unusual magnetic properties of the heavy-fermion compound $CeCoGe_3$. *Phys. Rev. B*, 47:11839–11847, May 1993.

[94] T. Terashima, M. Kimata, S. Uji, T. Sugawara, N. Kimura, H. Aoki, and H. Harima. Fermi surface in $LaRhSi_3$ and $CeRhSi_3$. *Phys. Rev. B*, 78:205107, Nov 2008.

[95] B. T. Thole, G. van der Laan, J. C. Fuggle, G. A. Sawatzky, R. C. Karnatak, and J.-M. Esteva. 3d x-ray-absorption lines and the $3d^9 4f^{n+1}$ multiplets of the lanthanides. *Phys. Rev. B*, 32:5107–5118, Oct 1985.

[96] Ruanchen Dong, Xiangang Wan, Xi Dai, and Sergey Y. Savrasov. Orbital-dependent electronic masses in Ce heavy-fermion materials studied via Gutzwiller density-functional theory. *Phys. Rev. B*, 89:165122, Apr 2014.

[97] Y. X. Yao, C. Z. Wang, and K. M. Ho. Including many-body screening into self-consistent calculations: Tight-binding model studies with the Gutzwiller approximation. *Phys. Rev. B*, 83:245139, Jun 2011.

[98] K. M. Ho, J. Schmalian, and C. Z. Wang. Gutzwiller density functional theory for correlated electron systems. *Phys. Rev. B*, 77:073101, Feb 2008.

[99] XiaoYu Deng, Xi Dai, and Zhong Fang. LDA+Gutzwiller method for correlated electron systems. *EPL (Europhysics Letters)*, 83(3):37008, jul 2008.

[100] XiaoYu Deng, Lei Wang, Xi Dai, and Zhong Fang. Local density approximation combined with Gutzwiller method for correlated electron systems: Formalism and applications. *Phys. Rev. B*, 79:075114, Feb 2009.

[101] A. D. Hillier, D. T. Adroja, P. Manuel, V. K. Anand, J. W. Taylor, K. A. McEwen, B. D. Rainford, and M. M. Koza. Muon spin relaxation and neutron scattering investigations of the noncentrosymmetric heavy-fermion antiferromagnet $CeRhGe_3$. *Phys. Rev. B*, 85:134405, Apr 2012.

[102] Yusuke Okuda, Yuichiro Miyauchi, Yuki Ida, Yuuji Takeda, Chie Tonohiro, Yasuhiro Oduchi, Tsutomu Yamada, Nguyen Duc Dung, Tatsuma D. Matsuda, Yoshinori Haga, Tetsuya Takeuchi, Masayuki Hagiwara, Koichi Kindo, Hisatomo Harima, Kiyohiro Sugiyama, Rikio Settai, and Yoshichika Ōnuki. Magnetic and Superconducting Properties of $LaIrSi_3$ and $CeIrSi_3$ with the Non-centrosymmetric Crystal Structure. *Journal of the Physical Society of Japan*, 76(4):044708, 2007.

[103] M. Smidman, D. T. Adroja, A. D. Hillier, L. C. Chapon, J. W. Taylor, V. K. Anand, R. P. Singh, M. R. Lees, E. A. Goremychkin, M. M. Koza, V. V. Krishnamurthy, D. M. Paul, and G. Balakrishnan. Neutron scattering and muon spin relaxation measurements of the noncentrosymmetric antiferromagnet $\mathbf{CeCoGe_3}$. *Phys. Rev. B*, 88:134416, Oct 2013.

[104] V. K. Anand, A. D. Hillier, D. T. Adroja, D. D. Khalyavin, P. Manuel, G. Andre, S. Rols, and M. M. Koza. Understanding the magnetism in noncentrosymmetric $CeIrGe_3$: Muon spin relaxation and neutron scattering studies. *Phys. Rev. B*, 97:184422, May 2018.

[105] Arumugam Thamizhavel, Hiroaki Shishido, Yusuke Okuda, Hisatomo Harima, Tatsuma D. Matsuda, Yoshinori Haga, Rikio Settai, and Yoshichika Ōnuki. Fermi Surface Property of $CeCoGe_3$ and $LaCoGe_3$ without Inversion Symmetry in the Tetragonal Crystal Structure. *Journal of the Physical Society of Japan*, 75(4):044711, 2006.

[106] Y. Muro, M. Ishikawa, K. Hirota, Z. Hiroi, N. Takeda, N. Kimura, and H. Aoki. Crystalline Electric Field Effect and Magnetic Properties of $CeRhSi_3$ Single Crystal. *Journal of the Physical Society of Japan*, 76(3):033706, 2007.

[107] S. Doniach. *Phase Diagram for the Kondo Lattice*, pages 169–176. Springer US, Boston, MA, 1977.

[108] Zhijun Wang, Yan Sun, Xing-Qiu Chen, Cesare Franchini, Gang Xu, Hongming Weng, Xi Dai, and Zhong Fang. Dirac semimetal and topological phase transitions in A_3Bi ($A = $ Na, K, Rb). *Phys. Rev. B*, 85:195320, May 2012.

[109] Zhijun Wang, Hongming Weng, Quansheng Wu, Xi Dai, and Zhong Fang. Three-dimensional Dirac semimetal and quantum transport in Cd_3As_2. *Phys. Rev. B*, 88:125427, Sep 2013.

[110] Bohm-Jung Yang and Naoto Nagaosa. Classification of stable three-dimensional Dirac semimetals with nontrivial topology. *Nature Communications*, 5(1):4898, Sep 2014.

[111] Q. D. Gibson, L. M. Schoop, L. Muechler, L. S. Xie, M. Hirschberger, N. P. Ong, R. Car, and R. J. Cava. Three-dimensional Dirac semimetals: Design principles and predictions of new materials. *Phys. Rev. B*, 91:205128, May 2015.

[112] Yongping Du, Bo Wan, Di Wang, Li Sheng, Chun-Gang Duan, and Xiangang Wan. Dirac and Weyl Semimetal in XYBi (X = Ba, Eu; Y = Cu, Ag and Au). *Scientific Reports*, 5(1):14423, Sep 2015.

[113] Hongming Weng, Chen Fang, Zhong Fang, B. Andrei Bernevig, and Xi Dai. Weyl Semimetal Phase in Noncentrosymmetric Transition-Metal Monophosphides. *Phys. Rev. X*, 5:011029, Mar 2015.

[114] Shin-Ming Huang, Su-Yang Xu, Ilya Belopolski, Chi-Cheng Lee, Guoqing Chang, BaoKai Wang, Nasser Alidoust, Guang Bian, Madhab Neupane, Chenglong Zhang, Shuang Jia, Arun Bansil, Hsin Lin, and M. Zahid Hasan. A Weyl Fermion semimetal with surface Fermi arcs in the transition metal monopnictide TaAs class. *Nature Communications*, 6(1):7373, Jun 2015.

[115] Youngkuk Kim, Benjamin J. Wieder, C. L. Kane, and Andrew M. Rappe. Dirac Line Nodes in Inversion-Symmetric Crystals. *Phys. Rev. Lett.*, 115:036806, Jul 2015.

[116] E. Bauer and M. Sigrist. *Non-Centrosymmetric Superconductors*. Springer, Berlin, Heidelberg, 2012.

[117] M Smidman, M B Salamon, H Q Yuan, and D F Agterberg. Superconductivity and spin–orbit coupling in non-centrosymmetric materials: a review. *Reports on Progress in Physics*, 80(3):036501, jan 2017.

[118] Sungkit Yip. Noncentrosymmetric Superconductors. *Annual Review of Condensed Matter Physics*, 5(1):15–33, 2014.

[119] F. Kneidinger, E. Bauer, I. Zeiringer, P. Rogl, C. Blaas-Schenner, D. Reith, and R. Podloucky. Superconductivity in non-centrosymmetric materials. *Physica C: Superconductivity and its Applications*, 514:388 – 398, 2015. Superconducting Materials: Conventional, Unconventional and Undetermined.

[120] P. A. Frigeri, D. F. Agterberg, A. Koga, and M. Sigrist. Superconductivity without Inversion Symmetry: MnSi versus $CePt_3Si$. *Phys. Rev. Lett.*, 92:097001, Mar 2004.

[121] K. V. Samokhin and V. P. Mineev. Gap structure in noncentrosymmetric superconductors. *Phys. Rev. B*, 77:104520, Mar 2008.

[122] Yasuhiro Tada, Norio Kawakami, and Satoshi Fujimoto. Microscopic Mechanism and Pairing Symmetry of Superconductivity in the Noncentrosymmetric Heavy Fermion Systems CeRhSI3 and CeIrSi3. *Journal of the Physical Society of Japan*, 77(5):054707, 2008.

[123] Y. Tada, N. Kawakami, and S. Fujimoto. Spin fluctuations and superconductivity in noncentrosymmetric heavy fermion systems $CeRhSi_3$ and $CeIrSi_3$. *Phys. Rev. B*, 81:104506, Mar 2010.

[124] Akito Daido and Youichi Yanase. Paramagnetically induced gapful topological superconductors. *Phys. Rev. B*, 94:054519, Aug 2016.

[125] Tomohiro Yoshida and Youichi Yanase. Topological $D + p$-wave superconductivity in Rashba systems. *Phys. Rev. B*, 93:054504, Feb 2016.

[126] Zhicheng Zhong, Anna Tóth, and Karsten Held. Theory of spin-orbit coupling at $LaAlO_3/SrTiO_3$ interfaces and $SrTiO_3$ surfaces. *Phys. Rev. B*, 87:161102, Apr 2013.

[127] D. Yu. Usachov, I. A. Nechaev, G. Poelchen, M. Güttler, E. E. Krasovskii, S. Schulz, A. Generalov, K. Kliemt, A. Kraiker, C. Krellner, K. Kummer, S. Danzenbächer, C. Laubschat, A. P. Weber, J. Sánchez-Barriga, E. V. Chulkov, A. F. Santander-Syro, T. Imai, K. Miyamoto, T. Okuda, and D. V. Vyalikh. Cubic Rashba Effect in the Surface Spin Structure of Rare-Earth Ternary Materials. *Phys. Rev. Lett.*, 124:237202, Jun 2020.

[128] Rai Moriya, Kentarou Sawano, Yusuke Hoshi, Satoru Masubuchi, Yasuhiro Shiraki, Andreas Wild, Christian Neumann, Gerhard Abstreiter, Dominique Bougeard, Takaaki Koga, and Tomoki Machida. Cubic Rashba Spin-Orbit Interaction of a Two-Dimensional Hole Gas in a Strained-Ge/SiGe Quantum Well. *Phys. Rev. Lett.*, 113:086601, Aug 2014.

[129] Youichi Yanase and Manfred Sigrist. Superconductivity and Magnetism in Noncentrosymmetric System: Application to CePt3Si. *Journal of the Physical Society of Japan*, 77(12):124711, 2008.

[130] H. Mukuda, T. Fujii, T. Ohara, A. Harada, M. Yashima, Y. Kitaoka, Y. Okuda, R. Settai, and Y. Onuki. Enhancement of Superconducting Transition Temperature due to the Strong Antiferromagnetic Spin Fluctuations in the Noncentrosymmetric Heavy-Fermion Superconductor $CeIrSi_3$: A ^{29}Si NMR Study under Pressure. *Phys. Rev. Lett.*, 100:107003, Mar 2008.

[131] H. Mukuda, T. Ohara, M. Yashima, Y. Kitaoka, R. Settai, Y. Ōnuki, K. M. Itoh, and E. E. Haller. Spin Susceptibility of Noncentrosymmetric Heavy-Fermion Superconductor $CeIrSi_3$ under Pressure: ^{29}Si Knight-Shift Study on Single Crystal. *Phys. Rev. Lett.*, 104:017002, Jan 2010.

[132] J. F. Landaeta, D. Subero, D. Catalá, S. V. Taylor, N. Kimura, R. Settai, Y. Ōnuki, M. Sigrist, and I. Bonalde. Unconventional superconductivity and quantum criticality in the heavy fermions $CeIrSi_3$ and $CeRhSi_3$. *Phys. Rev. B*, 97:104513, Mar 2018.

[133] Yoshinori Tokura. *Colossal Magnetoresistive Oxides*. Gordon and Breach Science Publishers, Amsterdam, The Netherlands, 2000.

[134] J. Georg Bednorz and K. Alex Müller. Perovskite-type oxides—The new approach to high-T_c superconductivity. *Rev. Mod. Phys.*, 60:585–600, Jul 1988.

[135] G. R. Stewart. Superconductivity in iron compounds. *Rev. Mod. Phys.*, 83:1589–1652, Dec 2011.

[136] David C. Koskenmaki and Karl A. Gschneidner. Chapter 4 Cerium. In *Metals*, volume 1 of *Handbook on the Physics and Chemistry of Rare Earths*, pages 337–377. Elsevier, 1978.

[137] Angus Lawson. Plutonium Magic. *Los Alamos Science*, 30:90–95, 2006.

[138] Qimiao Si and Frank Steglich. Heavy Fermions and Quantum Phase Transitions. *Science*, 329(5996):1161–1166, 2010.

[139] Maxim Dzero, Jing Xia, Victor Galitski, and Piers Coleman. Topological Kondo Insulators. *Annual Review of Condensed Matter Physics*, 7(1):249–280, 2016.

[140] Feng Lu, JianZhou Zhao, Hongming Weng, Zhong Fang, and Xi Dai. Correlated Topological Insulators with Mixed Valence. *Phys. Rev. Lett.*, 110:096401, Feb 2013.

[141] Binghai Yan, Lukas Müchler, Xiao-Liang Qi, Shou-Cheng Zhang, and Claudia Felser. Topological insulators in filled skutterudites. *Phys. Rev. B*, 85:165125, Apr 2012.

[142] Xiao Zhang, Haijun Zhang, Jing Wang, Claudia Felser, and Shou-Cheng Zhang. Actinide Topological Insulator Materials with Strong Interaction. *Science*, 335(6075):1464–1466, 2012.

[143] Masatoshi Imada, Atsushi Fujimori, and Yoshinori Tokura. Metal-insulator transitions. *Rev. Mod. Phys.*, 70:1039–1263, Oct 1998.

[144] Antoine Georges, Gabriel Kotliar, Werner Krauth, and Marcelo J. Rozenberg. Dynamical mean-field theory of strongly correlated fermion systems and the limit of infinite dimensions. *Rev. Mod. Phys.*, 68:13–125, Jan 1996.

[145] Stig Lundqvist and Norman H. March. *Theory of the Inhomogeneous Electron Gas*. Springer US, New York, 1983.

[146] Sung-Sik Lee and Shinsei Ryu. Many-Body Generalization of the Z_2 Topological Invariant for the Quantum Spin Hall Effect. *Phys. Rev. Lett.*, 100:186807, May 2008.

[147] Zhong Wang, Xiao-Liang Qi, and Shou-Cheng Zhang. Topological Order Parameters for Interacting Topological Insulators. *Phys. Rev. Lett.*, 105:256803, Dec 2010.

[148] S. Raghu, Xiao-Liang Qi, C. Honerkamp, and Shou-Cheng Zhang. Topological Mott Insulators. *Phys. Rev. Lett.*, 100:156401, Apr 2008.

[149] Dmytro Pesin and Leon Balents. Mott physics and band topology in materials with strong spin–orbit interaction. *Nature Physics*, 6(5):376–381, May 2010.

[150] Shun-Li Yu, X. C. Xie, and Jian-Xin Li. Mott Physics and Topological Phase Transition in Correlated Dirac Fermions. *Phys. Rev. Lett.*, 107:010401, Jun 2011.

[151] Teruhiko Akazawa, Takashi Suzuki, Fumihiko Nakamura, Toshizo Fujita, Toshiro Takabatake, and Hironobu Fujii. Anomalous Magnetic Transition in UNiSn. *Journal of the Physical Society of Japan*, 65(11):3661–3665, 1996.

[152] Peter S. Riseborough. Heavy fermion semiconductors. *Advances in Physics*, 49(3):257–320, 2000.

[153] Y. Aoki, T. Suzuki, T. Fujita, H. Kawanaka, T. Takabatake, and H. Fujii. Specific heat and magnetic susceptibility of $U_{1-x}Th_xNiSn$. *Phys. Rev. B*, 47:15060–15067, Jun 1993.

[154] K.R. Lea, M.J.M. Leask, and W.P. Wolf. The raising of angular momentum degeneracy of f-Electron terms by cubic crystal fields. *Journal of Physics and Chemistry of Solids*, 23(10):1381–1405, 1962.

[155] J.-S. Kang, J.-G. Park, K. A. McEwen, C. G. Olson, S. K. Kwon, and B. I. Min. Temperature-dependent valence-band photoemission study of UNiSn. *Phys. Rev. B*, 64:085101, Jul 2001.

[156] P. M. Oppeneer, A. N. Yaresko, A. Ya. Perlov, V. N. Antonov, and H. Eschrig. Theory of the anomalous magnetic phase transition in UNiSn. *Phys. Rev. B*, 54:R3706–R3709, Aug 1996.

[157] Vladimir I. Anisimov. *Strong Coulomb Correlations in Electronic Structure Calculations*. CRC Press, London, 2000.

[158] Cheng Zhang, Zhuoliang Ni, Jinglei Zhang, Xiang Yuan, Yanwen Liu, Yichao Zou, Zhiming Liao, Yongping Du, Awadhesh Narayan, Hongming Zhang, Tiancheng Gu, Xuesong Zhu, Li Pi, Stefano Sanvito, Xiaodong Han, Jin Zou, Yi Shi, Xiangang Wan, Sergey Y. Savrasov, and Faxian Xiu. Ultrahigh conductivity in Weyl semimetal NbAs nanobelts. *Nature Materials*, 18(5):482–488, May 2019.

[159] C. H. Li, O. M. J. van 't Erve, J. T. Robinson, Y. Liu, L. Li, and B. T. Jonker. Electrical detection of charge-current-induced spin polarization due to spin-momentum locking in Bi2Se3. *Nature Nanotechnology*, 9(3):218–224, Mar 2014.

[160] Xingyue Peng, Yiming Yang, Rajiv R.P. Singh, Sergey Y. Savrasov, and Dong Yu. Spin generation via bulk spin current in three-dimensional topological insulators. *Nature Communications*, 7(1):10878, Mar 2016.

[161] Sergey Y. Savrasov, Giacomo Resta, and Xiangang Wan. Local self-energies for V and Pd emergent from a nonlocal LDA+FLEX implementation. *Phys. Rev. B*, 97:155128, Apr 2018.

[162] Emanuel Gull, Andrew J. Millis, Alexander I. Lichtenstein, Alexey N. Rubtsov, Matthias Troyer, and Philipp Werner. Continuous-time Monte Carlo methods for quantum impurity models. *Rev. Mod. Phys.*, 83:349–404, May 2011.

[163] Sergej Y. Savrasov, Kristjan Haule, and Gabriel Kotliar. Many-Body Electronic Structure of Americium Metal. *Phys. Rev. Lett.*, 96:036404, Jan 2006.

[164] Lei Wang, Hua Jiang, Xi Dai, and X. C. Xie. Pole expansion of self-energy and interaction effect for topological insulators. *Phys. Rev. B*, 85:235135, Jun 2012.

[165] S. Y. Savrasov, G. Kotliar, and E. Abrahams. Correlated electrons in δ-plutonium within a dynamical mean-field picture. *Nature*, 410(6830):793–795, Apr 2001.

[166] Xiangang Wan, Jian Zhou, and Jinming Dong. The electronic structures and magnetic properties of perovskite ruthenates from constrained orbital-hybridization calculations. *EPL (Europhysics Letters)*, 92(5):57007, dec 2010.

[167] O. K. Andersen and O. Jepsen. Explicit, First-Principles Tight-Binding Theory. *Phys. Rev. Lett.*, 53:2571–2574, Dec 1984.

[168] Imseok Yang, Sergej Y. Savrasov, and Gabriel Kotliar. Importance of Correlation Effects on Magnetic Anisotropy in Fe and Ni. *Phys. Rev. Lett.*, 87:216405, Nov 2001.

[169] T.T.M. Palstra, G.J. Nieuwenhuys, R.F.M. Vlastuin, J. van den Berg, J.A. Mydosh, and K.H.J. Buschow. Magnetic and electrical properties of several equiatomic ternary U-compounds. *Journal of Magnetism and Magnetic Materials*, 67(3):331–342, 1987.

[170] J. Diehl, H. Fischer, R. Köhler, C. Geibel, F. Steglich, Y. Maeda, T. Takabatake, and H. Fujii. Hall effect and magnetoresistance in UNiSn. *Physica B: Condensed Matter*, 186-188:708–710, 1993.

[171] A. Otop, S. Süllow, E. W. Scheidt, and J. A. Mydosh. Critical reexamination of non-Fermi-liquid characteristics of moderately disordered UCu_4Pd. *Phys. Rev. B*, 77:045121, Jan 2008.

[172] M A López de la Torre, M A Arranz, M Ellerby, and K A McEwen. The Kondo contribution to the electrical resistivity in UCu5 xNixand the non-Fermi liquid behaviour of UCu4Ni. *Journal of Physics: Condensed Matter*, 15(17):2599–2606, apr 2003.

[173] S.G. Thomas, W.W. Kim, M. Lenkewitz, and G.R. Stewart. Formation of the heavy fermion ground state in UPt4M1, M = Au, Ag, Cu. *Physica B: Condensed Matter*, 199-200:88–90, 1994.

[174] Ming-Che Chang and Qian Niu. Berry phase, hyperorbits, and the Hofstadter spectrum: Semiclassical dynamics in magnetic Bloch bands. *Phys. Rev. B*, 53:7010–7023, Mar 1996.

[175] Ganesh Sundaram and Qian Niu. Wave-packet dynamics in slowly perturbed crystals: Gradient corrections and Berry-phase effects. *Phys. Rev. B*, 59:14915–14925, Jun 1999.

[176] Shuichi Murakami, Naoto Nagaosa, and Shou-Cheng Zhang. Dissipationless Quantum Spin Current at Room Temperature. *Science*, 301(5638):1348–1351, 2003.

[177] Jairo Sinova, Dimitrie Culcer, Q. Niu, N. A. Sinitsyn, T. Jungwirth, and A. H. MacDonald. Universal Intrinsic Spin Hall Effect. *Phys. Rev. Lett.*, 92:126603, Mar 2004.

[178] R. D. King-Smith and David Vanderbilt. Theory of polarization of crystalline solids. *Phys. Rev. B*, 47:1651–1654, Jan 1993.

[179] Raffaele Resta. Macroscopic polarization in crystalline dielectrics: the geometric phase approach. *Rev. Mod. Phys.*, 66:899–915, Jul 1994.

[180] T. Jungwirth, Qian Niu, and A. H. MacDonald. Anomalous Hall Effect in Ferromagnetic Semiconductors. *Phys. Rev. Lett.*, 88:207208, May 2002.

[181] Yugui Yao, Leonard Kleinman, A. H. MacDonald, Jairo Sinova, T. Jungwirth, Dingsheng Wang, Enge Wang, and Qian Niu. First Principles Calculation of Anomalous Hall Conductivity in Ferromagnetic bcc Fe. *Phys. Rev. Lett.*, 92:037204, Jan 2004.

[182] Di Xiao, Yugui Yao, Zhong Fang, and Qian Niu. Berry-Phase Effect in Anomalous Thermoelectric Transport. *Phys. Rev. Lett.*, 97:026603, Jul 2006.

[183] T. Asaba, V. Ivanov, S. M. Thomas, S. Y. Savrasov, J. D. Thompson, E. D. Bauer, and F. Ronning. Colossal anomalous Nernst effect in a correlated noncentrosymmetric kagome ferromagnet. *Science Advances*, 7(13), 2021.

[184] P Streda. Theory of quantised Hall conductivity in two dimensions. *Journal of Physics C: Solid State Physics*, 15(22):L717–L721, aug 1982.

[185] Michael P. Marder. *Dynamics of Bloch Electrons*, chapter 16, pages 453–481. John Wiley & Sons, Ltd, 2010.

[186] Yayu Wang, Z. A. Xu, T. Kakeshita, S. Uchida, S. Ono, Yoichi Ando, and N. P. Ong. Onset of the vortexlike Nernst signal above T_c in $La_{2-x}Sr_xCuO_4$ and $Bi_2Sr_{2-y}La_yCuO_6$. *Phys. Rev. B*, 64:224519, Nov 2001.

[187] Akito Sakai, Yo Pierre Mizuta, Agustinus Agung Nugroho, Rombang Sihombing, Takashi Koretsune, Michi-To Suzuki, Nayuta Takemori, Rieko Ishii, Daisuke Nishio-Hamane, Pallab Arita, Ryotaroand Goswami, and Satoru Nakatsuji. Giant anomalous Nernst effect and quantum-critical scaling in a ferromagnetic semimetal. *Nature Physics*, 14(11):1119–1124, Nov 2018.

[188] A. A. Zyuzin and R. P. Tiwari. Intrinsic anomalous Hall effect in Type-II Weyl semimetals. *JETP Letters*, 103(11):717–722, Jun 2016.

[189] See supplementary information for Nature Physics **14**, 1119 (2018). which can be found at https://doi.org/10.1038/s41567-018-0225-6.

[190] Enke Liu, Yan Sun, Nitesh Kumar, Lukas Muechler, Aili Sun, Lin Jiao, Shuo-Ying Yang, Defa Liu, Aiji Liang, Qiunan Xu, Johannes Kroder, Vicky Süß, Horst Borrmann, Chandra Shekhar, Zhaosheng Wang, Chuanying Xi, Wenhong Wang, Walter Schnelle, Steffen Wirth, Yulin Chen, Sebastian T. B. Goennenwein, and Claudia Felser. Giant anomalous Hall effect in a ferromagnetic kagome-lattice semimetal. *Nature Physics*, 14(11):1125–1131, Nov 2018.

[191] T Kida, L A Fenner, A A Dee, I Terasaki, M Hagiwara, and A S Wills. The giant anomalous Hall effect in the ferromagnet Fe3Sn2—a frustrated kagome metal. *Journal of Physics: Condensed Matter*, 23(11):112205, mar 2011.

[192] Linda Ye, Mingu Kang, Junwei Liu, Felix von Cube, Christina R. Wicker, Takehito Suzuki, Chris Jozwiak, Aaron Bostwick, Eli Rotenberg, David C. Bell, Liang Fu, Riccardo Comin, and Joseph G. Checkelsky. Massive Dirac fermions in a ferromagnetic kagome metal. *Nature*, 555(7698):638–642, Mar 2018.

[193] Gang Xu, Biao Lian, and Shou-Cheng Zhang. Intrinsic Quantum Anomalous Hall Effect in the Kagome Lattice $Cs_2LiMn_3F_{12}$. *Phys. Rev. Lett.*, 115:186802, Oct 2015.

[194] Satoru Nakatsuji, Naoki Kiyohara, and Tomoya Higo. Large anomalous Hall effect in a non-collinear antiferromagnet at room temperature. *Nature*, 527(7577):212–215, Nov 2015.

[195] A. V. Andreev, L. Havela, V. Sechovsk, M. I. Bartashevich, J. ŠEbek, R. V. Dremov, and I. K. Kozlovskaya. Ferromagnetism in the UCo1-xRuxAl quasiternary intermetallics. *Philosophical Magazine B*, 75(6):827–844, 1997.

[196] Jiří Pospíšil, Petr Opletal, Michal Vališka, Yo Tokunaga, Anne Stunault, Yoshinori Haga, Naoyuki Tateiwa, Béatrice Gillon, Fuminori Honda, Tomoo Yamamura, Vojtěch Nižňanský, Etsuji Yamamoto, and Dai Aoki. Properties and Collapse of the Ferromagnetism in $UCo_{1-x}Ru_xAl$ Studied in Single Crystals. *Journal of the Physical Society of Japan*, 85(3):034710, 2016.

[197] P. A. Veenhuizen, F. R. de Boer, A. A. Menovsky, V. Sechovsky, and L. Havela. Magnetic Properties of URuAl AND URhAl Single Crystals. *J. Phys. Colloques*, 49(C8):C8–485–C8–486, 1988.

[198] T. D. Matsuda, H. Sugawara, Y. Aoki, H. Sato, A. V. Andreev, Y. Shiokawa, V. Sechovsky, and L. Havela. Transport properties of the anisotropic itinerant-electron metamagnet UCoAl. *Phys. Rev. B*, 62:13852–13855, Dec 2000.

[199] V. N. Antonov, B. N. Harmon, O. V. Andryushchenko, L. V. Bekenev, and A. N. Yaresko. Electronic structure and x-ray magnetic circular dichroism in uranium compounds. II. UTAl (T = Co, Rh, and Pt) intermetallics. *Phys. Rev. B*, 68:214425, Dec 2003.

[200] Shin-ichi Fujimori, Yukiharu Takeda, Tetsuo Okane, Yuji Saitoh, Atsushi Fujimori, Hiroshi Yamagami, Yoshinori Haga, Etsuji Yamamoto, and Yoshichika Ōnuki. Electronic Structures of Uranium Compounds Studied by Soft X-ray Photoelectron Spectroscopy. *Journal of the Physical Society of Japan*, 85(6):062001, 2016.

[201] Liangcai Xu, Xiaokang Li, Linchao Ding, Taishi Chen, Akito Sakai, Benoît Fauqué, Satoru Nakatsuji, Zengwei Zhu, and Kamran Behnia. Anomalous transverse response of Co_2MnGa and universality of the room-temperature $\alpha_{ij}^A/\sigma_{ij}^A$ ratio across topological magnets. *Phys. Rev. B*, 101:180404, May 2020.

[202] T. Gasche, S. Auluck, M.S.S. Brooks, and B. Johansson. Theory of the magnetism of ternary uranium compounds. *Journal of Magnetism and Magnetic Materials*, 104-107:37 – 38, 1992.

[203] T Gasche, M S S Brooks, and B Johansson. Ground-state properties of ternary uranium compounds: II. Magnetic properties. *Journal of Physics: Condensed Matter*, 7(49):9511–9519, dec 1995.

[204] T Gasche, M S S Brooks, and B Johansson. Ground-state properties of ternary uranium compounds: I. Hybridization effects. *Journal of Physics: Condensed Matter*, 7(49):9499–9510, dec 1995.

[205] S Chang, H Nakotte, A.J Schultz, H.N Bordallo, M.S Torikachvili, V Sechovsky, and A.V Andreev. Crystallographic order and magnetism in UCo1/3T2/3Al compounds (T=Ru, Rh, Pt). *Physica B: Condensed Matter*, 276-278:634 – 635, 2000.

[206] S. Chang, H. Nakotte, A. V. Andreev, H. N. Bordallo, L. Havela, V. Sechovsky, and M. S. Torikachvili. Magnetism in some UCo1/3T2/3Al solid solutions (T=transition metal). *Journal of Applied Physics*, 87(9):6812–6814, 2000.

[207] M. Kučera, J. Kuneš, A. Kolomiets, M. Diviš, A. V. Andreev, V. Sechovský, J.-P. Kappler, and A. Rogalev. X-ray magnetic circular dichroism studies of $5f$ magnetism in UCoAl and UPtAl. *Phys. Rev. B*, 66:144405, Oct 2002.

[208] A. V. Andreev, V. Sechovsky, L. Havela, J. Šebek, M. I. Bartashevich, T. Goto, K. Kamishima, D. A. Andreev, V. S. Gaviko, R. V. Dremov, and I. K. Kozlovskaya. Onset of ferromagnetism between the paramagnets UCoAl and URuAl. *Czechoslovak Journal of Physics*, 46(6):3385–3386, Jun 1996.

[209] J. G. Bednorz and K. A. Müller. Possible highTc superconductivity in the Ba–La–Cu–O system. *Zeitschrift für Physik B Condensed Matter*, 64(2):189–193, Jun 1986.

[210] P.W. Anderson. Resonating valence bonds: A new kind of insulator? *Materials Research Bulletin*, 8(2):153–160, 1973.

[211] P. W. ANDERSON. The Resonating Valence Bond State in La2CuO4 and Superconductivity. *Science*, 235(4793):1196–1198, 1987.

[212] Steven A. Kivelson, Daniel S. Rokhsar, and James P. Sethna. Topology of the resonating valence-bond state: Solitons and high-T_c superconductivity. *Phys. Rev. B*, 35:8865–8868, Jun 1987.

[213] Daniel S. Rokhsar and Steven A. Kivelson. Superconductivity and the Quantum Hard-Core Dimer Gas. *Phys. Rev. Lett.*, 61:2376–2379, Nov 1988.

[214] X. G. Wen. Vacuum degeneracy of chiral spin states in compactified space. *Phys. Rev. B*, 40:7387–7390, Oct 1989.

[215] Yi Zhou, Kazushi Kanoda, and Tai-Kai Ng. Quantum spin liquid states. *Rev. Mod. Phys.*, 89:025003, Apr 2017.

[216] Lucile Savary and Leon Balents. Quantum spin liquids: a review. *Reports on Progress in Physics*, 80(1):016502, nov 2016.

[217] Leon Balents. Spin liquids in frustrated magnets. *Nature*, 464(7286):199–208, Mar 2010.

[218] Patrick A. Lee, Naoto Nagaosa, and Xiao-Gang Wen. Doping a Mott insulator: Physics of high-temperature superconductivity. *Rev. Mod. Phys.*, 78:17–85, Jan 2006.

[219] Xiangang Wan, Vsevolod Ivanov, Giacomo Resta, Ivan Leonov, and Sergey Y. Savrasov. Exchange interactions and sensitivity of the Ni two-hole spin state to Hund's coupling in doped $NdNiO_2$. *Phys. Rev. B*, 103:075123, Feb 2021.

[220] C. C. Tsuei and J. R. Kirtley. Pairing symmetry in cuprate superconductors. *Rev. Mod. Phys.*, 72:969–1016, Oct 2000.

[221] D. J. Scalapino. A common thread: The pairing interaction for unconventional superconductors. *Rev. Mod. Phys.*, 84:1383–1417, Oct 2012.

[222] J. Zaanen, G. A. Sawatzky, and J. W. Allen. Band gaps and electronic structure of transition-metal compounds. *Phys. Rev. Lett.*, 55:418–421, Jul 1985.

[223] F. C. Zhang and T. M. Rice. Effective Hamiltonian for the superconducting Cu oxides. *Phys. Rev. B*, 37:3759–3761, Mar 1988.

[224] E. Pavarini, I. Dasgupta, T. Saha-Dasgupta, O. Jepsen, and O. K. Andersen. Band-Structure Trend in Hole-Doped Cuprates and Correlation with $T_{c\max}$. *Phys. Rev. Lett.*, 87:047003, Jul 2001.

[225] Hirofumi Sakakibara, Hidetomo Usui, Kazuhiko Kuroki, Ryotaro Arita, and Hideo Aoki. Two-Orbital Model Explains the Higher Transition Temperature of the Single-Layer Hg-Cuprate Superconductor Compared to That of the La-Cuprate Superconductor. *Phys. Rev. Lett.*, 105:057003, Jul 2010.

[226] J. Choisnet, R.A. Evarestov, I.I. Tupitsyn, and V.A. Veryazov. Investigation of the chemical bonding in nickel mixed oxides from electronic structure calculations. *Journal of Physics and Chemistry of Solids*, 57(12):1839–1850, 1996.

[227] M.J Martínez-Lope, M.T Casais, and J.A Alonso. Stabilization of Ni+ in defect perovskites $La(Ni_{1-x}Al_x)O_2$+x with 'infinite-layer' structure. *Journal of Alloys and Compounds*, 275-277:109–112, 1998.

[228] M. A. Hayward, M. A. Green, M. J. Rosseinsky, and J. Sloan. Sodium Hydride as a Powerful Reducing Agent for Topotactic Oxide Deintercalation: Synthesis and Characterization of the Nickel(I) Oxide LaNiO2. *Journal of the American Chemical Society*, 121(38):8843–8854, Sep 1999.

[229] Ai Ikeda, Takaaki Manabe, and Michio Naito. Improved conductivity of infinite-layer LaNiO2 thin films by metal organic decomposition. *Physica C: Superconductivity*, 495:134–140, 2013.

[230] K.-W. Lee and W. E. Pickett. Infinite-layer $LaNiO_2$: Ni^{1+} is not Cu^{2+}. *Phys. Rev. B*, 70:165109, Oct 2004.

[231] V. I. Anisimov, D. Bukhvalov, and T. M. Rice. Electronic structure of possible nickelate analogs to the cuprates. *Phys. Rev. B*, 59:7901–7906, Mar 1999.

[232] Danfeng Li, Kyuho Lee, Bai Yang Wang, Motoki Osada, Samuel Crossley, Hye Ryoung Lee, Yi Cui, Yasuyuki Hikita, and Harold Y. Hwang. Superconductivity in an infinite-layer nickelate. *Nature*, 572(7771):624–627, Aug 2019.

[233] Danfeng Li, Bai Yang Wang, Kyuho Lee, Shannon P. Harvey, Motoki Osada, Berit H. Goodge, Lena F. Kourkoutis, and Harold Y. Hwang. Superconducting Dome in $Nd_{1-x}Sr_xNiO_2$ Infinite Layer Films. *Phys. Rev. Lett.*, 125:027001, Jul 2020.

[234] Shengwei Zeng, Chi Sin Tang, Xinmao Yin, Changjian Li, Mengsha Li, Zhen Huang, Junxiong Hu, Wei Liu, Ganesh Ji Omar, Hariom Jani, Zhi Shiuh Lim, Kun Han, Dongyang Wan, Ping Yang, Stephen John Pennycook, Andrew T. S. Wee, and Ariando Ariando. Phase Diagram and Superconducting Dome of Infinite-Layer $Nd_{1-x}Sr_xNiO_2$ Thin Films. *Phys. Rev. Lett.*, 125:147003, Oct 2020.

[235] Motoki Osada, Bai Yang Wang, Berit H. Goodge, Kyuho Lee, Hyeok Yoon, Keita Sakuma, Danfeng Li, Masashi Miura, Lena F. Kourkoutis, and Harold Y. Hwang. A Superconducting Praseodymium Nickelate with Infinite Layer Structure. *Nano Letters*, 20(8):5735–5740, Aug 2020.

[236] A. S. Botana and M. R. Norman. Similarities and Differences between $LaNiO_2$ and $CaCuO_2$ and Implications for Superconductivity. *Phys. Rev. X*, 10:011024, Feb 2020.

[237] Mi-Young Choi, Kwan-Woo Lee, and Warren E. Pickett. Role of $4f$ states in infinite-layer $NdNiO_2$. *Phys. Rev. B*, 101:020503, Jan 2020.

[238] Valerio Olevano, Fabio Bernardini, Xavier Blase, and Andrés Cano. Ab initio many-body *GW* correlations in the electronic structure of $LaNiO_2$. *Phys. Rev. B*, 101:161102, Apr 2020.

[239] Yusuke Nomura, Motoaki Hirayama, Terumasa Tadano, Yoshihide Yoshimoto, Kazuma Nakamura, and Ryotaro Arita. Formation of a two-dimensional single-component correlated electron system and band engineering in the nickelate superconductor $NdNiO_2$. *Phys. Rev. B*, 100:205138, Nov 2019.

[240] Zhao Liu, Zhi Ren, Wei Zhu, Zhengfei Wang, and Jinlong Yang. Electronic and magnetic structure of infinite-layer NdNiO2: trace of antiferromagnetic metal. *npj Quantum Materials*, 5(1):31, May 2020.

[241] Jiacheng Gao, Shiyu Peng, Zhijun Wang, Chen Fang, and Hongming Weng. Electronic structures and topological properties in nickelates Lnn + 1NinO2n + 2. *National Science Review*, 09 2020. nwaa218.

[242] M. Hepting, D. Li, C. J. Jia, H. Lu, E. Paris, Y. Tseng, X. Feng, M. Osada, E. Been, Y. Hikita, Y.-D. Chuang, Z. Hussain, K. J. Zhou, A. Nag, M. Garcia-Fernandez, M. Rossi, H. Y. Huang, D. J. Huang, Z. X. Shen, T. Schmitt, H. Y. Hwang, B. Moritz, J. Zaanen, T. P. Devereaux, and W. S. Lee. Electronic structure of the parent compound of superconducting infinite-layer nickelates. *Nature Materials*, 19(4):381–385, Apr 2020.

[243] Emily Been, Wei-Sheng Lee, Harold Y. Hwang, Yi Cui, Jan Zaanen, Thomas Devereaux, Brian Moritz, and Chunjing Jia. Electronic Structure Trends Across the Rare-Earth Series in Superconducting Infinite-Layer Nickelates. *Phys. Rev. X*, 11:011050, Mar 2021.

[244] Yuhao Gu, Sichen Zhu, Xiaoxuan Wang, Jiangping Hu, and Hanghui Chen. A substantial hybridization between correlated Ni-d orbital and itinerant electrons in infinite-layer nickelates. *Communications Physics*, 3(1):84, May 2020.

[245] Liang Si, Wen Xiao, Josef Kaufmann, Jan M. Tomczak, Yi Lu, Zhicheng Zhong, and Karsten Held. Topotactic Hydrogen in Nickelate Superconductors and Akin Infinite-Layer Oxides ABO_2. *Phys. Rev. Lett.*, 124:166402, Apr 2020.

[246] Mi Jiang, Mona Berciu, and George A. Sawatzky. Critical Nature of the Ni Spin State in Doped $NdNiO_2$. *Phys. Rev. Lett.*, 124:207004, May 2020.

[247] Frank Lechermann. Late transition metal oxides with infinite-layer structure: Nickelates versus cuprates. *Phys. Rev. B*, 101:081110, Feb 2020.

[248] Lun-Hui Hu and Congjun Wu. Two-band model for magnetism and superconductivity in nickelates. *Phys. Rev. Research*, 1:032046, Dec 2019.

[249] Ya-Hui Zhang and Ashvin Vishwanath. Type-II $t-J$ model in superconducting nickelate $Nd_{1-x}Sr_xNiO_2$. *Phys. Rev. Research*, 2:023112, May 2020.

[250] Jonathan Karp, Antia S. Botana, Michael R. Norman, Hyowon Park, Manuel Zingl, and Andrew Millis. Many-Body Electronic Structure of $NdNiO_2$ and $CaCuO_2$. *Phys. Rev. X*, 10:021061, Jun 2020.

[251] Frank Lechermann. Multiorbital Processes Rule the $Nd_{1-x}Sr_xNiO_2$ Normal State. *Phys. Rev. X*, 10:041002, Oct 2020.

[252] Philipp Werner and Shintaro Hoshino. Nickelate superconductors: Multiorbital nature and spin freezing. *Phys. Rev. B*, 101:041104, Jan 2020.

[253] Francesco Petocchi, Viktor Christiansson, Fredrik Nilsson, Ferdi Aryasetiawan, and Philipp Werner. Normal State of $Nd_{1-x}Sr_xNiO_2$ from Self-Consistent GW + EDMFT. *Phys. Rev. X*, 10:041047, Dec 2020.

[254] Mi-Young Choi, Warren E. Pickett, and Kwan-Woo Lee. Fluctuation-frustrated flat band instabilities in $NdNiO_2$. *Phys. Rev. Research*, 2:033445, Sep 2020.

[255] Xianxin Wu, Domenico Di Sante, Tilman Schwemmer, Werner Hanke, Harold Y. Hwang, Srinivas Raghu, and Ronny Thomale. Robust $d_{x^2-y^2}$-wave superconductivity of infinite-layer nickelates. *Phys. Rev. B*, 101:060504, Feb 2020.

[256] Hirofumi Sakakibara, Hidetomo Usui, Katsuhiro Suzuki, Takao Kotani, Hideo Aoki, and Kazuhiko Kuroki. Model Construction and a Possibility of Cupratelike Pairing in a New d^9 Nickelate Superconductor $(\mathrm{Nd},\mathrm{Sr})\mathrm{NiO}_2$. *Phys. Rev. Lett.*, 125:077003, Aug 2020.

[257] Byungkyun Kang, Corey Melnick, Patrick Semon, Siheon Ryee, Myung Joon Han, Gabriel Kotliar, and Sangkook Choi. Infinite-layer nickelates as Ni-eg Hund's metals, 2020.

[258] Zi-Jian Lang, Ruoshi Jiang, and Wei Ku. Where do the hole carriers reside in the new superconducting nickelates?, 2020.

[259] Motoharu Kitatani, Liang Si, Oleg Janson, Ryotaro Arita, Zhicheng Zhong, and Karsten Held. Nickelate superconductors—a renaissance of the one-band Hubbard model. *npj Quantum Materials*, 5(1):59, Aug 2020.

[260] I. Leonov, S. L. Skornyakov, and S. Y. Savrasov. Lifshitz transition and frustration of magnetic moments in infinite-layer NdNiO_2 upon hole doping. *Phys. Rev. B*, 101:241108, Jun 2020.

[261] Guang-Ming Zhang, Yi-feng Yang, and Fu-Chun Zhang. Self-doped Mott insulator for parent compounds of nickelate superconductors. *Phys. Rev. B*, 101:020501, Jan 2020.

[262] Emilian M. Nica, Jyoti Krishna, Rong Yu, Qimiao Si, Antia S. Botana, and Onur Erten. Theoretical investigation of superconductivity in trilayer square-planar nickelates. *Phys. Rev. B*, 102:020504, Jul 2020.

[263] Tao Zhou, Yi Gao, and ZiDan Wang. Spin excitations in nickelate superconductors. *Science China Physics, Mechanics & Astronomy*, 63(8):287412, Jun 2020.

[264] Changjiang Liu, Vincent F. C. Humbert, Terence M. Bretz-Sullivan, Gensheng Wang, Deshun Hong, Friederike Wrobel, Jianjie Zhang, Jason D. Hoffman, John E. Pearson, J. Samuel Jiang, Clarence Chang, Alexey Suslov, Nadya Mason, M. R. Norman, and Anand Bhattacharya. Observation of an antiferromagnetic quantum critical point in high-purity LaNiO3. *Nature Communications*, 11(1):1402, Mar 2020.

[265] Ying Fu, Le Wang, Hu Cheng, Shenghai Pei, Xuefeng Zhou, Jian Chen, Shaoheng Wang, Ran Zhao, Wenrui Jiang, Cai Liu, Mingyuan Huang, XinWei Wang, Yusheng Zhao, Dapeng Yu, Fei Ye, Shanmin Wang, and Jia-Wei Mei. Core-level x-ray photoemission and Raman spectroscopy studies on electronic structures in Mott-Hubbard type nickelate oxide NdNiO_2, 2019.

[266] Yi Cui, C. Li, Q. Li, Xiyu Zhu, Z. Hu, Yi feng Yang, J. S. Zhang, Rong Yu, Hai-Hu Wen, and Weiqiang Yu. NMR Evidence of Antiferromagnetism in $\mathrm{Nd}_{0.85}\mathrm{Sr}_{0.15}\mathrm{NiO}_2$, 2020.

[267] Hu Zhang, Lipeng Jin, Shanmin Wang, Bin Xi, Xingqiang Shi, Fei Ye, and Jia-Wei Mei. Effective Hamiltonian for nickelate oxides $Nd_{1-x}Sr_xNiO_2$. *Phys. Rev. Research*, 2:013214, Feb 2020.

[268] Siheon Ryee, Hongkee Yoon, Taek Jung Kim, Min Yong Jeong, and Myung Joon Han. Induced magnetic two-dimensionality by hole doping in the superconducting infinite-layer nickelate $Nd_{1-x}Sr_xNiO_2$. *Phys. Rev. B*, 101:064513, Feb 2020.

[269] Yusuke Nomura, Takuya Nomoto, Motoaki Hirayama, and Ryotaro Arita. Magnetic exchange coupling in cuprate-analog d^9 nickelates. *Phys. Rev. Research*, 2:043144, Oct 2020.

[270] Xiangang Wan, Quan Yin, and Sergej Y. Savrasov. Calculation of Magnetic Exchange Interactions in Mott-Hubbard Systems. *Phys. Rev. Lett.*, 97:266403, Dec 2006.

[271] A.I. Liechtenstein, M.I. Katsnelson, V.P. Antropov, and V.A. Gubanov. Local spin density functional approach to the theory of exchange interactions in ferromagnetic metals and alloys. *Journal of Magnetism and Magnetic Materials*, 67(1):65–74, 1987.

[272] Yongping Du, Hang-Chen Ding, Li Sheng, Sergey Y Savrasov, Xiangang Wan, and Chun-Gang Duan. Microscopic origin of stereochemically active lone pair formation from orbital selective external potential calculations. *Journal of Physics: Condensed Matter*, 26(2):025503, dec 2013.

[273] Peiheng Jiang, Liang Si, Zhaoliang Liao, and Zhicheng Zhong. Electronic structure of rare-earth infinite-layer $R\mathrm{NiO}_2(R = \mathrm{La}, \mathrm{Nd})$. *Phys. Rev. B*, 100:201106, Nov 2019.

[274] Vladimir I Anisimov, F Aryasetiawan, and A I Lichtenstein. First-principles calculations of the electronic structure and spectra of strongly correlated systems: the LDA+U method. *Journal of Physics: Condensed Matter*, 9(4):767–808, jan 1997.

[275] See Supplemental Material at http://link.aps.org/supplemental/ 10.1103/PhysRevB.103.075123 for additional results, supporting our conclusions.

[276] Xiangang Wan, Thomas A. Maier, and Sergej Y. Savrasov. Calculated magnetic exchange interactions in high-temperature superconductors. *Phys. Rev. B*, 79:155114, Apr 2009.

[277] Myung Joon Han, Quan Yin, Warren E. Pickett, and Sergey Y. Savrasov. Anisotropy, Itineracy, and Magnetic Frustration in High-T_C Iron Pnictides. *Phys. Rev. Lett.*, 102:107003, Mar 2009.

[278] Xiangang Wan, Jinming Dong, and Sergej Y. Savrasov. Mechanism of magnetic exchange interactions in europium monochalcogenides. *Phys. Rev. B*, 83:205201, May 2011.

[279] R. Nanguneri and S. Y. Savrasov. Exchange constants and spin waves of the orbital-ordered noncollinear spinel MnV_2O_4. *Phys. Rev. B*, 86:085138, Aug 2012.

[280] Di Wang, Xiangyan Bo, Feng Tang, and Xiangang Wan. Calculated magnetic exchange interactions in the Dirac magnon material Cu_3TeO_6. *Phys. Rev. B*, 99:035160, Jan 2019.

[281] J. Q. Lin, P. Villar Arribi, G. Fabbris, A. S. Botana, D. Meyers, H. Miao, Y. Shen, D. G. Mazzone, J. Feng, S. G. Chiuzbăian, A. Nag, A. C. Walters, M. García-Fernández, Ke-Jin Zhou, J. Pelliciari, I. Jarrige, J. W. Freeland, Junjie Zhang, J. F. Mitchell, V. Bisogni, X. Liu, M. R. Norman, and M. P. M. Dean. Strong Superexchange in a $d^{9-\delta}$ Nickelate Revealed by Resonant Inelastic X-Ray Scattering. *Phys. Rev. Lett.*, 126:087001, Feb 2021.

[282] Kristjan Haule. Quantum Monte Carlo impurity solver for cluster dynamical mean-field theory and electronic structure calculations with adjustable cluster base. *Phys. Rev. B*, 75:155113, Apr 2007.

[283] D. S. Inosov, J. Fink, A. A. Kordyuk, S. V. Borisenko, V. B. Zabolotnyy, R. Schuster, M. Knupfer, B. Büchner, R. Follath, H. A. Dürr, W. Eberhardt, V. Hinkov, B. Keimer, and H. Berger. Momentum and Energy Dependence of the Anomalous High-Energy Dispersion in the Electronic Structure of High Temperature Superconductors. *Phys. Rev. Lett.*, 99:237002, Dec 2007.

[284] Quan Yin, Alexey Gordienko, Xiangang Wan, and Sergey Y. Savrasov. Calculated Momentum Dependence of Zhang-Rice States in Transition Metal Oxides. *Phys. Rev. Lett.*, 100:066406, Feb 2008.

[285] Ying Xiang, Qing Li, Yueying Li, Huan Yang, Yuefeng Nie, and Hai-Hu Wen. Physical properties revealed by transport measurements on superconducting $Nd_{0.8}Sr_{0.2}NiO_2$ thin films, 2020.

[286] M. Rossi, H. Lu, A. Nag, D. Li, M. Osada, K. Lee, B. Y. Wang, S. Agrestini, M. Garcia-Fernandez, Y. D. Chuang, Z. X. Shen, H. Y. Hwang, B. Moritz, Ke-Jin Zhou, T. P. Devereaux, and W. S. Lee. Orbital and Spin Character of Doped Carriers in Infinite-Layer Nickelates, 2020.

[287] Luis Elcoro, Barry Bradlyn, Zhijun Wang, Maia G. Vergniory, Jennifer Cano, Claudia Felser, B. Andrei Bernevig, Danel Orobengoa, Gemma de la Flor, and Mois I. Aroyo. Double crystallographic groups and their representations on the Bilbao Crystallographic Server. *Journal of Applied Crystallography*, 50(5):1457–1477, Oct 2017.

[288] S. Yu. Savrasov and D. Yu. Savrasov. Full-potential linear-muffin-tin-orbital method for calculating total energies and forces. *Phys. Rev. B*, 46:12181–12195, Nov 1992.

Appendix A

Additional details of topological features in compounds with the ZrNiAl–type structure

Figures 1–13 provide complete data for for the topological materials predicted in this work: the band structures near the Fermi level, energy panels used for defining non–Abelian Berry connection, positions of low–energy topological nodal points in the Brillouin Zone as well as energy band dispersions in the vicinity of the nodal points.

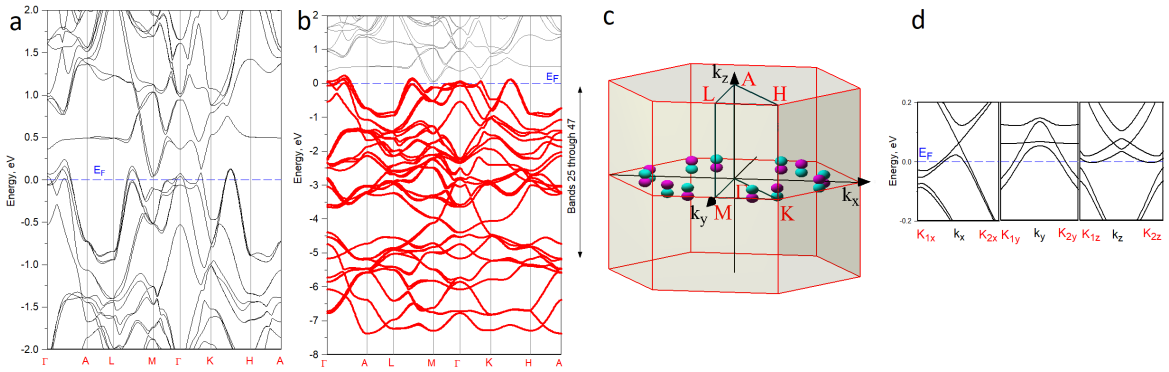

Figure A.1: Results for HfPRu: a. band structure near the Fermi level; b. energy panel used for defining non-Abelian Berry connection; c. positions of low-energy Weyl points as well as d. energy band dispersions in the vicinity of the Weyl point $k_{wp} = (0.46280, 0.06931, 0.02210)$. Point notations are as follows: $K_{1x} = (0.36280, 0.069310, 0.022100), K_{2x} = (0.56280, 0.069310, 0.022100), K_{1y} = (0.46280, -0.17328, 0.02210), K_{2y} = (0.46280, 0.17328, 0.022100), K_{1z} = (0.46280, 0.06931, -0.11050), K_{2z} = (0.46280, 0.06931, 0.11050)$ in units $2\pi/a, 2\pi/a, 2\pi/c$. Lattice parameters used: a=12.1207 a.u., c/a=0.58513 [75].

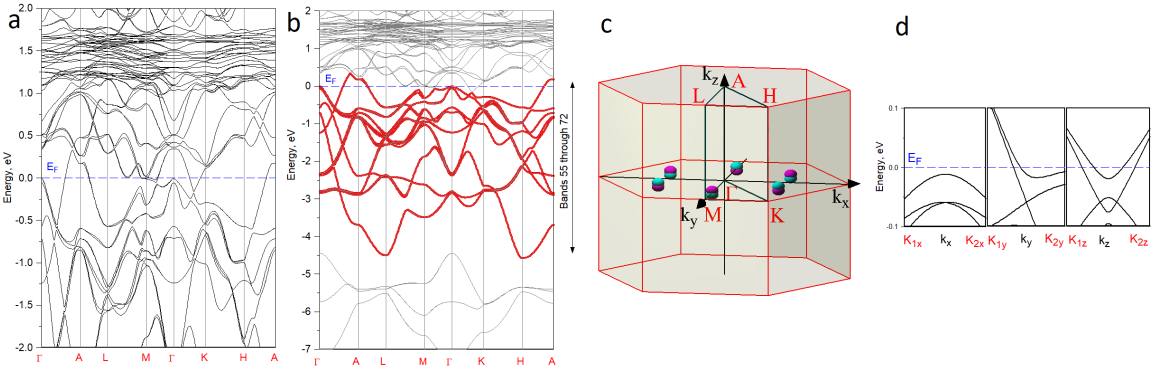

Figure A.2: Results for LaInMg: a. band structure near the Fermi level; b. energy panel used for defining non-Abelian Berry connection; c. positions of low-energy Weyl points as well as d. energy band dispersions in the vicinity of the Weyl point $k_{wp} = (0.00000, 0.36868, 0.01123)$. Point notations are as follows: $K_{1x} = (-0.10000, 0.36868, 0.01123), K_{2x} = (0.10000, 0.36868, 0.01123), K_{1y} = (0.0000, 0.26868, 0.01123), K_{2y} = (0.0000, 0.46868, 0.011230), K_{1z} = (0.0000, 0.36868, -0.056150), K_{2z} = (0.0000, 0.36868, 0.056150)$ in units $2\pi/a, 2\pi/a, 2\pi/c$. Lattice parameters used: a=14.789 a.u., c/a=0.61472 [70].

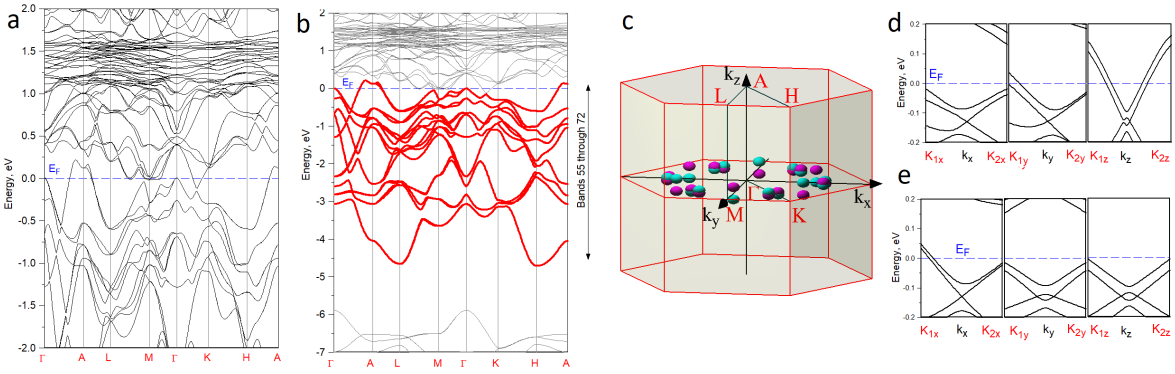

Figure A.3: Results for LaTlMg: a. band structure near the Fermi level; b. energy panel used for defining non-Abelian Berry connection; c. positions of low-energy Weyl points; d. energy band dispersions in the vicinity of the Weyl point $k_{wp} = (0.00000, 0.38916, 0.03236)$. Points notations are as follows: $K_{1x} = (-0.10000, 0.38916, 0.032360), K_{2x} = (0.10000, 0.38916, 0.032360), K_{1y} = (0.0000, 0.28916, 0.03236), K_{2y} = (0.0000, 0.48916, 0.03236), K_{1z} = (0.0000, 0.38916, -0.16180), K_{2z} = (0.0000, 0.38916, 0.16180)$ in units $2\pi/a, 2\pi/a, 2\pi/c$ as well as e. energy band dispersions in the vicinity of the Weyl point $k_{wp} = (0.41450, 0.02567, 0.00724)$. Point notations are as follows: $K_{1x} = (0.3145, 0, 0.02567, 0.00724), K_{2x} = (0.51450, 0.02567, 0.00724), K_{1y} = (0.41450, -0.12835, 0.00724), K_{2y} = (0.41450, 0.12835, 0.00724), K_{1z} = (0.41450, 0.02567, -0.0362), K_{2z} = (0.41450, 0.02567, 0.0362)$ in units $2\pi/a, 2\pi/a, 2\pi/c$. Lattice parameters used: a=14.7644 a.u., c/a=0.61160 [76].

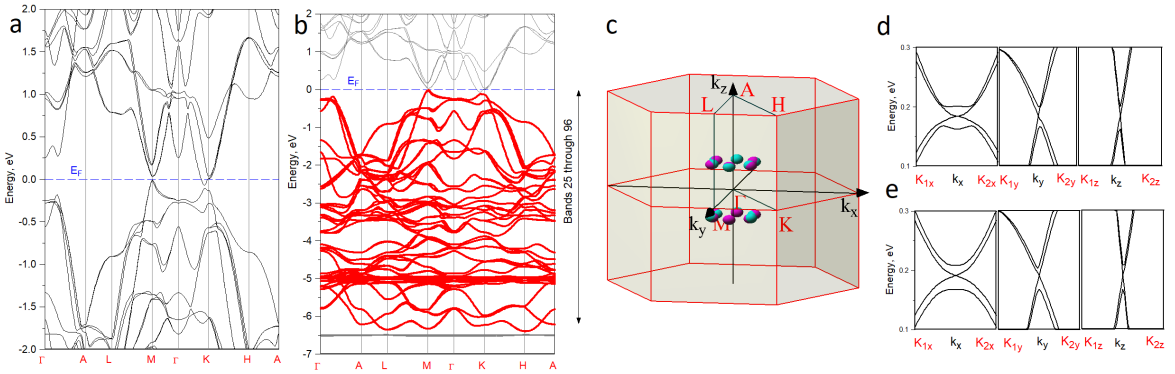

Figure A.4: Results for LuAsPd: a. band structure near the Fermi level; b. energy panel used for defining non-Abelian Berry connection; c. positions of low-energy Weyl points as well as d. energy band dispersions in the vicinity of the Weyl point $k_{wp} = (0.00000, 0.11481, 0.14140)$. Point notations are as follows: $K_{1x} = (-0.10000, 0.11481, 0.14140), K_{2x} = (0.10000, 0.11481, 0.14140), K_{1y} = (0.0000, 0.01481, 0.14140), K_{2y} = (0.0000, 0.21481, 0.14140), K_{1z} = (0.0000, 0.11481, 0.0414), K_{2z} = (0.0000, 0.11481, 0.24140)$ in units $2\pi/a, 2\pi/a, 2\pi/c$. Lattice parameters used: a=13.1733 a.u., c/a=0.55817 [77].

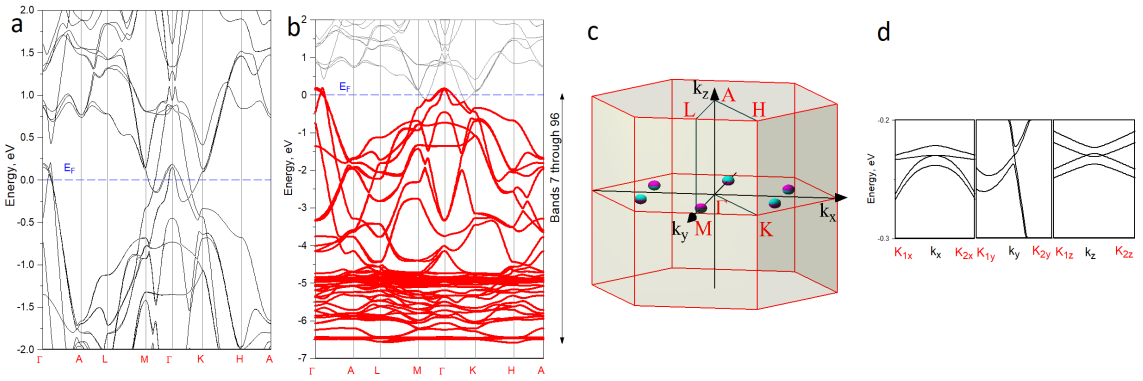

Figure A.5: Results for LuGeAg: a. band structure near the Fermi level; b. energy panel used for defining non-Abelian Berry connection; c. positions of low-energy Weyl points as well as d. energy band dispersions in the vicinity of the Weyl point $k_{wp} = (0.00000, 0.42190, 0.00098)$. Point notations are as follows: $K_{1x} = (-0.10000, 0.42190, 0.00098), K_{2x} = (0.10000, 0.42190, 0.00098), K_{1y} = (0.0000, 0.32190, 0.00098), K_{2y} = (0.0000, 0.52190, 0.00098), K_{1z} = (0.0000, 0.42190, -0.0049), K_{2z} = (0.0000, 0.42190, 0.0049)$ in units $2\pi/a, 2\pi/a, 2\pi/c$. Lattice parameters used: a=13.2517 a.u., c/a=0.58948 [71].

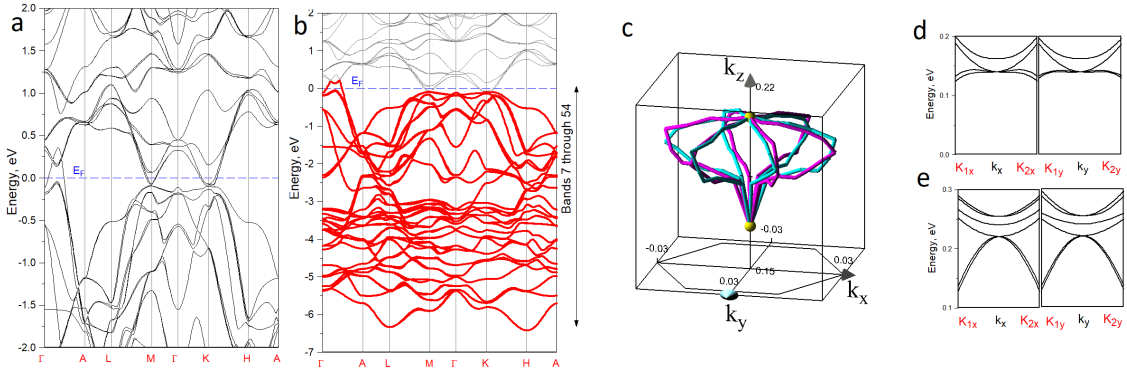

Figure A.6: Results for TiGePd: a. band structure near the Fermi level; b. energy panel used for defining non-Abelian Berry connection; c. nodal lines and positions of triple degenerate points. The zoomed area of the BZ is bounded by $0.15 \leq 2\pi k_z/c \leq 0.22$ and $-0.03 \leq 2\pi k_{x,y}/a \leq +0.03$; d. energy band dispersions in the vicinity of the triple point $k_{tp} = (0.00000, 0.00000, 0.16495)$. Points notations are as follows: $K_{1x} = (-0.10000, 0.0000, 0.16495), K_{2x} = (0.10000, 0.0000, 0.16495), K_{1y} = (0.0000, -0.10000, 0.16495), K_{2y} = (0.0000, 0.10000, 0.16495)$ in units $2\pi/a, 2\pi/a, 2\pi/c$; e. energy band dispersions in the vicinity of the triple point $k_{tp} = (0.00000, 0.00000, 0.20775)$. Point notations are as follows: $K_{1x} = (-0.10000, 0.0000, 0.20775), K_{2x} = (0.10000, 0.0000, 0.20775), K_{1y} = (0.0000, -0.10000, 0.20775)$ in units $2\pi/a, 2\pi/a, 2\pi/c$. Lattice parameters used: a=12.4779 a.u., c/a=0.56032 [79].

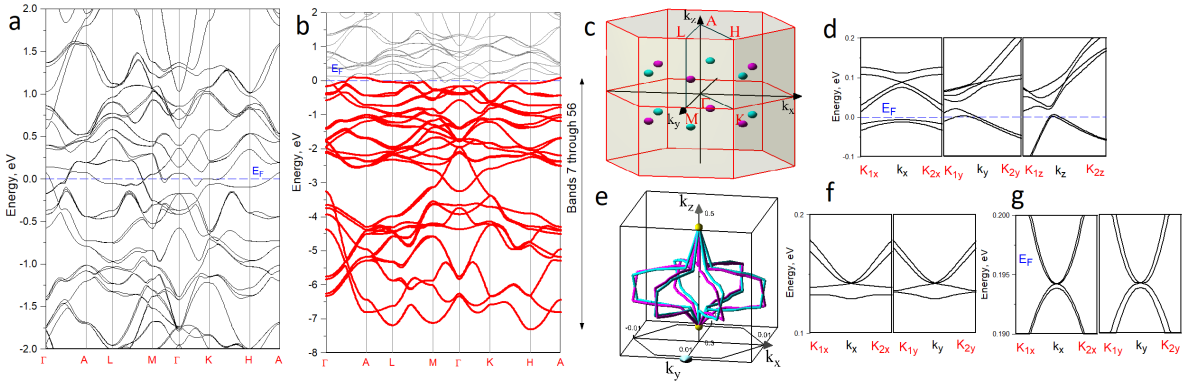

Figure A.7: Results for VAsFe: a. band structure near the Fermi level; b. energy panel used for defining non-Abelian Berry connection; c. positions of low-energy Weyl points; d. energy band dispersions in the vicinity of the Weyl point $k_{wp} = (0.00000, 0.38339, 0.17269)$. Points notations are as follows: $K_{1x} = (-0.10000, 0.38339, 0.17269), K_{2x} = (0.10000, 0.38339, 0.17269), K_{1y} = (0.0000, 0.28339, 0.17269), K_{2y} = (0.0000, 0.48339, 0.17269), K_{1z} = (0.0000, 0.38339, 0.07269), K_{2z} = (0.0000, 0.38339, 0.27269)$ in units $2\pi/a, 2\pi/a, 2\pi/c$.; e. nodal lines with triple degenerate points. The zoomed area of the BZ is bounded by $0.3 \leq 2\pi k_z/c \leq 0.5$ and $-0.01 \leq 2\pi k_{x,y}/a \leq +0.01$.; f. energy band dispersions in the vicinity of the triple point $k_{tp} = (0.00000, 0.00000, 0.32279)$. Points notations are as follows: $K_{1x} = (-0.10000, 0.0000, 0.32279), K_{2x} = (0.10000, 0.0000, 0.32279), K_{1y} = (0.0000, -0.1000, 0.32279), K_{2y} = (0.00000, 0.1000, 0.32279)$. in units $2\pi/a, 2\pi/a, 2\pi/c$; g. energy band dispersions in the vicinity of the triple point $k_{tp} = (0.00000, 0.00000, 0.47625)$. Point notations are as follows: $K_{1x} = (-0.10000, 0.0000, 0.47625), K_{2x} = (0.10000, 0.0000, 0.47625), K_{1y} = (0.0000, -0.1000, 0.47625), K_{2y} = (0.00000, 0.1000, 0.47625)$. in units $2\pi/a, 2\pi/a, 2\pi/c$. Lattice parameters used: a=11.7352 a.u., c/a=0.56892 [80].

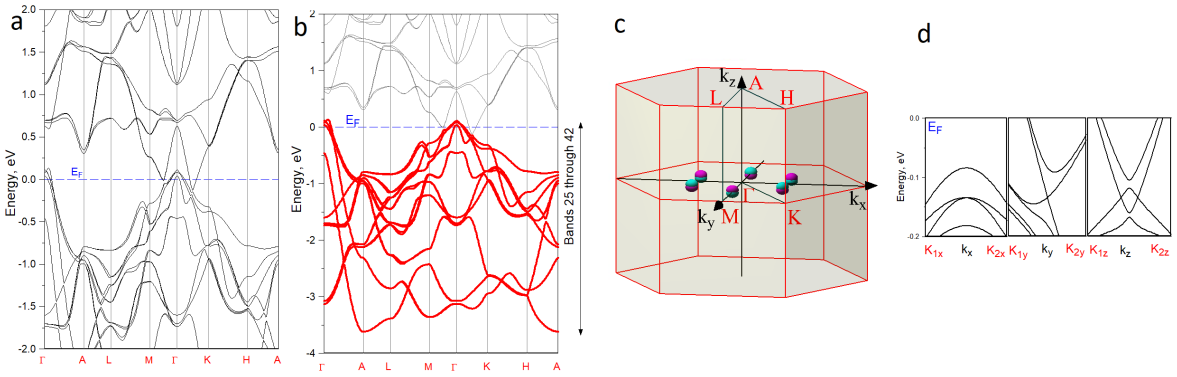

Figure A.8: Results for YGeLi: a. band structure near the Fermi level; b. energy panel used for defining non-Abelian Berry connection; c. positions of low-energy Weyl points as well as d. energy band dispersions in the vicinity of the Weyl point $k_{wp} = (0.00000, 0.27793, 0.00817)$. Point notations are as follows: $K_{1x} = (-0.10000, 0.27793, 0.00817), K_{2x} = (0.10000, 0.27793, 0.00817), K_{1y} = (0.0000, 0.17793, 0.00817), K_{2y} = (0.0000, 0.37793, 0.00817), K_{1z} = (0.0000, 0.27793, -0.040850), K_{2z} = (0.0000, 0.27793, 0.04085)$ in units $2\pi/a, 2\pi/a, 2\pi/c$. Lattice parameters used: a=13.3509 a.u., c/a=0.59915 [72].

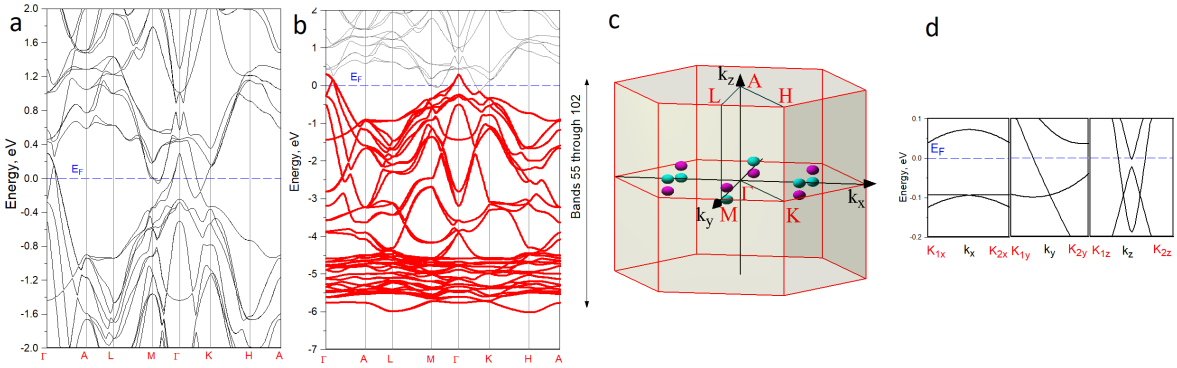

Figure A.9: Results for YPbAg: a. band structure near the Fermi level; b. energy panel used for defining non-Abelian Berry connection; c. positions of low-energy Weyl points as well as d. energy band dispersions in the vicinity of the Weyl point $k_{wp} = (0.00000, 0.40335, 0.03142)$. Point notations are as follows: $K_{1x} = (-0.10000, 0.40335, 0.03142), K_{2x} = (0.10000, 0.40335, 0.03142), K_{1y} = (0.0000, 0.30335, 0.03142), K_{2y} = (0.0000, 0.50335, 0.03142), K_{1z} = (0.0000, 0.40335, -0.15710), K_{2z} = (0.0000, 0.40335, 0.15710)$ in units $2\pi/a, 2\pi/a, 2\pi/c$. Lattice parameters used: a=14.140 a.u., c/a=0.59133 [73].

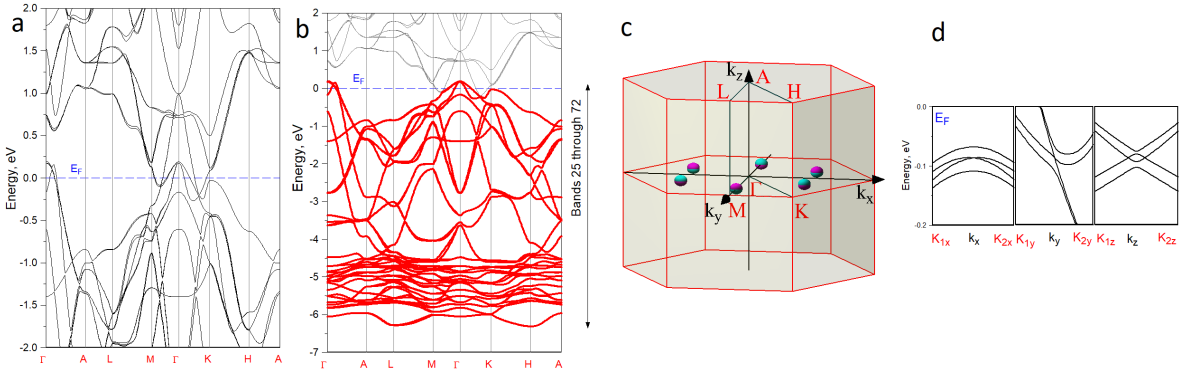

Figure A.10: Results for YSiAg: a. band structure near the Fermi level; b. energy panel used for defining non-Abelian Berry connection; c. positions of low-energy Weyl points as well as d. energy band dispersions in the vicinity of the Weyl point $k_{wp} = (0.00000, 0.37866, 0.00385)$. Point notations are as follows: $K_{1x} = (-0.10000, 0.37864, 0.00385)$, $K_{2x} = (0.10000, 0.37864, 0.00385)$, $K_{1y} = (0.0000, 0.27864, 0.00385)$, $K_{2y} = (0.0000, 0.47864, 0.00385)$, $K_{1z} = (0.0000, 0.37864, -0.0192)$, $K_{2z} = (0.0000, 0.37864, 0.0192)$ in units $2\pi/a, 2\pi/a, 2\pi/c$. Lattice parameters used: a=13.2623 a.u., c/a=0.59364 [74].

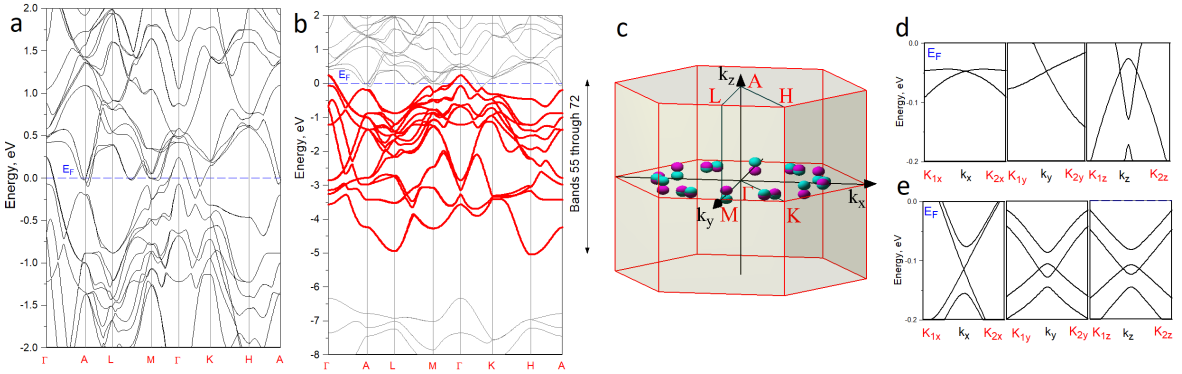

Figure A.11: Results for YTlMg: a. band structure near the Fermi level; b. energy panel used for defining non-Abelian Berry connection; c. positions of low-energy Weyl points; d. energy band dispersions in the vicinity of the Weyl point $k_{wp} = (0.00000, 0.43303, 0.02319)$. Points notations are as follows: $K_{1x} = (-0.10000, 0.43303, 0.02319)$, $K_{2x} = (0.10000, 0.43303, 0.02319)$, $K_{1y} = (0.0000, 0.33303, 0.02319)$, $K_{2y} = (0.0000, 0.53303, 0.02319)$, $K_{1z} = (0.0000, 0.43303, -0.11595)$, $K_{2z} = (0.0000, 0.43303, 0.11595)$ in units $2\pi/a, 2\pi/a, 2\pi/c$. e. energy band dispersions in the vicinity of the Weyl point $k_{wp} = (0.44076, 0.02908, 0.00441)$. Point notations are as follows: $K_{1x} = (0.34076, 0.02908, 0.00441)$, $K_{2x} = (0.54076, 0.02908, 0.00441)$, $K_{1y} = (0.44076, -0.14540, 0.00441)$, $K_{2y} = (0.44076, 0.14540, 0.00441)$, $K_{1z} = (0.44076, 0.02908, -0.02205)$, $K_{2z} = (0.44076, 0.02908, 0.02205)$ in units $2\pi/a, 2\pi/a, 2\pi/c$. Lattice parameters used: a=14.1824 a.u., c/a=0.61272 [76].

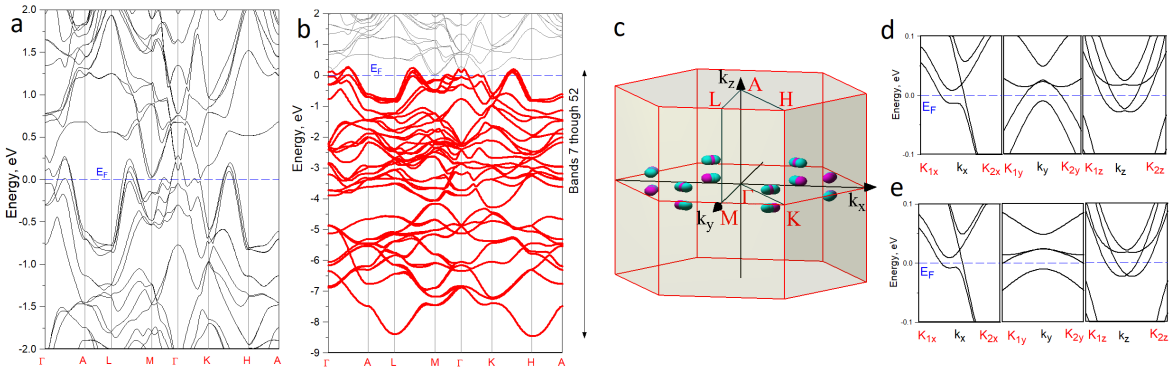

Figure A.12: Results for ZrAsOs: a. band structure near the Fermi level; b. energy panel used for defining non-Abelian Berry connection; c. positions of low-energy Weyl points; d. energy band dispersions in the vicinity of the Weyl point $k_{wp} = (0.47365, 0.02591, 0.04792)$. Points notations are as follows: $K_{1x} = (0.37365, 0.02591, 0.04792), K_{2x} = (0.57365, 0.02591, 0.04792), K_{1y} = (0.47365, -0.12955, 0.04792), K_{2y} = (0.47365, 0.12955, 0.04792), K_{1z} = (0.47365, 0.02591, -0.11980), K_{2z} = (0.47365, 0.02591, 0.11980)$ in units $2\pi/a, 2\pi/a, 2\pi/c$; e. energy band dispersions in the vicinity of the Weyl point $k_{wp} = (0.474060.012150.047890)$. Point notations are as follows: $K_{1x} = (0.37406, -0.01215, 0.04789), K_{2x} = (0.57406, -0.01215, 0.04789), K_{1y} = (0.47406, -0.06075, 0.04789), K_{2y} = (0.47406, 0.06075, 0.04789), K_{1z} = (0.47406, 0.01215, -0.11973), K_{2z} = (0.47406, 0.01215, 0.11973)$ in units $2\pi/a, 2\pi/a, 2\pi/c$. Lattice parameters used: a=12.476 a.u., c/a=0.57467 [78].

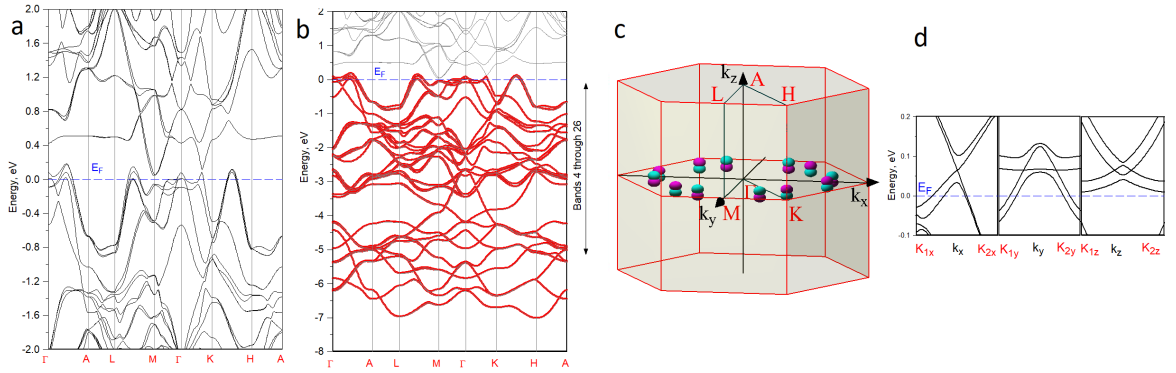

Figure A.13: Results for ZrPRu: a. band structure near the Fermi level; b. energy panel used for defining non-Abelian Berry connection; c. positions of low-energy Weyl points as well as d. energy band dispersions in the vicinity of the Weyl point $k_{wp} = (0.45982, 0.07532, 0.01698)$. Point notations are as follows: $K_{1x} = (0.35982, 0.07532, 0.01698), K_{2x} = (0.55982, 0.07532, 0.01698), K_{1y} = (0.45982, -0.18830, 0.01698), K_{2y} = (0.45982, 0.18830, 0.01698), K_{1z} = (0.45982, 0.07532, -0.0849), K_{2z} = (0.45982, 0.07532, 0.0849)$ in units $2\pi/a, 2\pi/a, 2\pi/c$. Lattice parameters used: a=12.2057 a.u., c/a=0.58492 [75].

Appendix B

Computational details and topological features of $CeTX_3$ superconductors

B.1 LDA+Gutzwiller Method and Double Counting Scheme

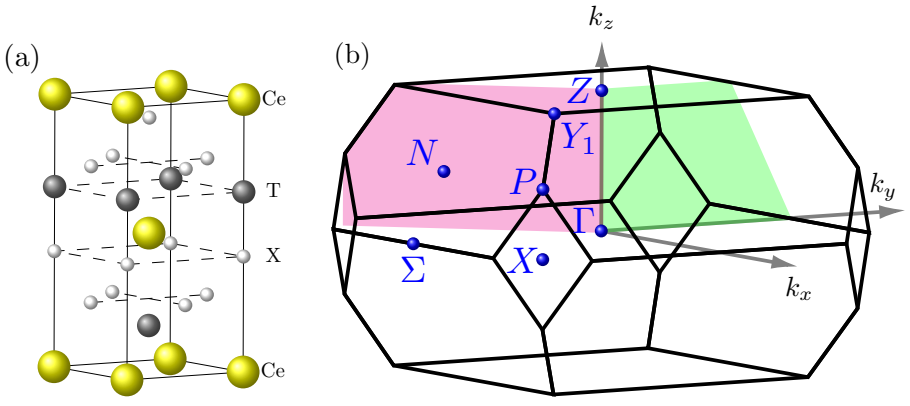

Figure B.1: (a) The crystal structure of the $CeTX_3$ compounds. (b) The bulk BZ, with the σ_v (green) and σ_d (magenta) planes highlighted.

Here we provide a brief description of the LDA+Gutzwiller method; a more detailed

can be found in Refs. [99, 100, 98, 97]. In the Gutzwiller method, the non-interacting wavefunction $|\Psi_0\rangle$ is projected onto the Gutzwiller wavefunction $|\Psi_G\rangle$ using a local projector:

$$|\Psi_G\rangle = \hat{\mathcal{P}}\,|\Psi_0\rangle = \prod_i \left(\sum_\Gamma \lambda_{i\Gamma}\hat{m}_{i\Gamma}\right)|\Psi_0\rangle \tag{B.1}$$

where the operators $\hat{m}_{i\Gamma} = |i\Gamma\rangle\langle i\Gamma|$ project the state onto a particular configuration $|\Gamma\rangle$ at site i, and the variational parameters $0 \leq \lambda_{i\Gamma} \leq 1$ adjust the weight of each many-body configuration. Any operator $\hat{A}$ acting on $|\Psi_G\rangle$, can mapped onto a corresponding Gutzwiller operator $\hat{A}^G = \hat{\mathcal{P}}\hat{A}\hat{\mathcal{P}}$ acting on $|\Psi_0\rangle$. For a single particle operator such as $\hat{A} = \sum_{ij,\alpha\beta}\langle i\alpha|\,\hat{A}\,|j\beta\rangle\, c^\dagger_{i\alpha}c_{j\beta}$, the corresponding Gutzwiller operator is

$$\begin{aligned}\hat{A}^G = &\sum_{ij,\alpha\beta}\sqrt{z_{i\alpha}}\,\langle i\alpha|\,\hat{A}\,|j\beta\rangle\,\sqrt{z_{j\beta}}c^\dagger_{i\alpha}c_{j\beta}\\ &+\sum_{i,\alpha}\langle i\alpha|\,\hat{A}\,|i\alpha\rangle\,(1-z_{i\alpha})c^\dagger_{i\alpha}c_{i\alpha}\end{aligned} \tag{B.2}$$

where the $z_{i\alpha}$ are the orbital-dependent quasiparticle residues:

$$z_{i\alpha} = \sum_{\Gamma\Gamma'}\frac{\sqrt{m_{i\Gamma}m_{i\Gamma'}}\left|\langle i\Gamma'|\,c^\dagger_{i\alpha}\,|i\Gamma\rangle\right|}{\sqrt{n_{i\alpha}(1-n_{i\alpha})}} \tag{B.3}$$

where $m_{i\Gamma} = \langle\Psi_G|\,\hat{m}_{i\Gamma}\,|\Psi_G\rangle$ and $n_{i\alpha}$ are the orbital occupation numbers.

In the same spirit as LDA+U and LDA+DMFT, we can write the Hamiltonian as

$$H = H_{\text{LDA}} + H_{\text{int}} - H_{\text{DC}} \tag{B.4}$$

where the on-on-site interaction term H_{int} for the set of correlated Ce$-4f$ orbitals, is layered on top of the tight-binding Hamiltonian H_{LDA} extracted from the LDA calculation. Since the mean-field Coulomb interaction has already been included within the LDA calculation,

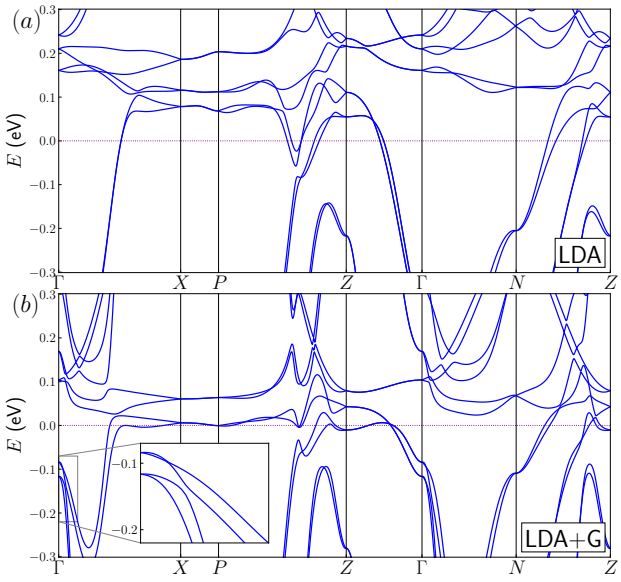

Figure B.2: Band structure of $CeCoGe_3$ calculated with (a) LDA and (b) LDA+G. The two lowest doublets, $\Gamma_7^{(1)}$ and Γ_6 are renormalized by correlations. Inset shows band crossings leading to nodal lines near Γ.

we need to subtract the double counting term H_{DC}.

We compute the electronic structure for the $CeTX_3$ (T = Co, Rh, Ir, X = Si, Ge) series with the $BaNiSn_3$-type structure (Fig. B.1a). In order to best match the experimentally determined Fermi surfaces for these compounds, we use a hybrid double counting scheme

$$V_{DC,\beta} = \Sigma_\beta(0) \tag{B.5}$$

$$V_{DC,\alpha} = 0.1\mathrm{Ry} + \frac{1}{N}\sum_{\alpha\neq\beta}^{N}\Sigma_\alpha(0), \quad \text{for all other states } \alpha \neq \beta \tag{B.6}$$

which treats the lowest energy doublets $\beta = \Gamma_7^{(1)}, \Gamma_6$, independently from the remaining bands. The band structure results for the LDA+G calculation are shown in Figure B.2, where the renormalization of the Cerium 4f band by correlations can be clearly seen.

We compare the spin structure extracted from our simulations (See Fig B.3) with a

tight binding model which is commonly used for theoretical studies of the $CeTX_3$ family:

$$H = \sum_k \epsilon_k c_k^\dagger c_k + \alpha \sum_k c_k^\dagger \boldsymbol{\gamma}(\mathbf{k}) \cdot \tilde{\boldsymbol{\sigma}} c_k \tag{B.7}$$

$$\begin{aligned}\epsilon_k = &-2t_1(\cos k_x + \cos k_y) + 4t_2(\cos k_x \cos k_y) \\ &- 8t_3 \cos(k_x/2)\cos(k_y/2)\cos(k_z)\end{aligned} \tag{B.8}$$

where $\boldsymbol{\gamma}(\mathbf{k}) = \alpha(\sin(k_y), -\sin(k_x), 0)$ is a Rashba-like spin-orbit coupling. We use the parameters $(t_1, t_2, t_3, \alpha) = (1.0, 0.475, 0.3, 0.4)$, which have been shown to reproduce the principal features of the LDA FS[122].

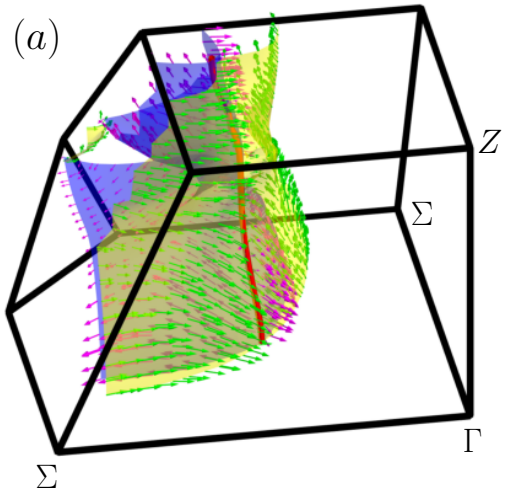

Figure B.3: The two bands forming NL-5 (red) in LDA, with the surface contours taken at the energy of the NL at each k_z. Arrows indicate the direction of the spins on the surfaces, showing the spin inversion at the nodal line.

To verify the choice of the empirical 0.1Ry parameter, we additionally perform LDA+G simulations with a shift of 1.0Ry. As seen in Figure B.4 below, the band structure near the Fermi energy is mostly unaffected. There is a slight change in the quasiparticle residues z_α, with the residues corresponding to the $\Gamma_6/\Gamma_7^{(1)}$ doublets decreasing slightly, and the residue for the $\Gamma_7^{(2)}$ doublet approaching 1, which is expected since the upwardly shifted bands hybridize less with the ground state doublets, and become unoccupied. The exact z_α values for this new shift are shown in Table B.1.

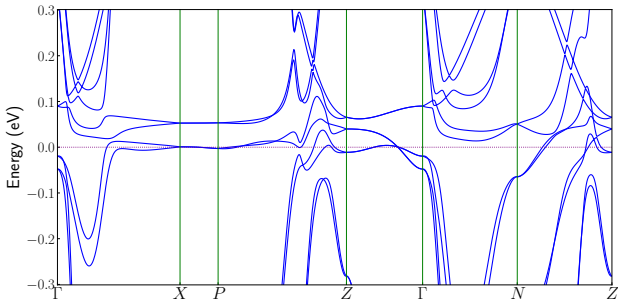

Figure B.4: Band structure plot for $CeCoGe_3$, computed with the $\Gamma_7^{(2)}$ doublet and J=7/2 manifold shifted upward by 1.0Ry, in the hybrid double counting scheme.

Table B.1: Quasiparticle residues z_α for the lowest energy doublets for the members of the $CeTX_3$ series, computed with a shift of 1.0 Ry.

	$z_{\mathrm{LDA+G}}$ (U=5 eV)		
	$\Gamma_7^{(1)}$	Γ_6	$\Gamma_7^{(2)}$
$CeCoSi_3$	0.48	0.46	1.00
$CeRhSi_3$	0.28	0.26	1.00
$CeIrSi_3$	0.29	0.28	1.00
$CeCoGe_3$	0.27	0.25	1.00
$CeRhGe_3$	0.18	0.10	1.00
$CeIrGe_3$	0.17	0.12	1.00

B.2 Determination of Mirror Eigenvalues and Irreducible Representation Characters for Bands Forming Nodal Lines

When spin-orbit coupling is considered, the symmetries of the $CeTX_3$ compounds can be described by irreducible representations of the C_{4v} double point group. For points in the BZ lying within the σ_v (green) or σ_d (magenta) mirror planes (Fig. B.1b), the states belong to irreducible representations of the mirror symmetry little group, C_S. The point group tables[287] are given below for C_{4v}, describing points along the $\Gamma - Z$ line, $\Lambda(0,0,u)$, and for C_S, describing points within the σ_v ($\Sigma(u,0,0)$) and σ_d ($\Delta(u,u,0)$) planes.

In particular, the compatibility relations for points along the $\Gamma - X$, $\Gamma - \Sigma$, and $\Gamma - Z$ axes (Δ, Σ, and Λ respectively) are

For convenience, we will also use the Δ and Σ to label the bands at points away from the $k_z = 0$ lines, since all points within the mirror planes will have C_S character. In the $CeTX_3$ compounds, the spinful bands at points in the mirror planes must belong to either Σ_3/Δ_3 or Σ_4/Δ_4 irreducible representations. When two bands belonging to different irreducible representations intersect, they will form Weyl nodal lines which are protected by the mirror symmetry [22].

The representation to which a band belongs to can be determined from the eigenvalue of the mirror symmetry operator $\sigma = \sigma_d$ or σ_v acting on the eigenvector at that point. Within the FP-LMTO formalism, the eigenvectors are constructed from the $\chi^{\boldsymbol{k}}_{\kappa Rlm}(\boldsymbol{r}_{R'})$ LMTO basis states, where $\boldsymbol{R}$ denotes the atom positions, lm are the angular momentum quantum numbers, and κ is a subscript corresponding to the choice of tail energies[288, 61, 96]. Within this eigenbasis, the mirror symmetries can be written:

$$\begin{aligned}\sigma_v \chi^{\boldsymbol{k}}_{\kappa Rlm} &= (-1)^m(-i\sigma_2)\chi^{\boldsymbol{k}}_{\kappa Rl-m} \\ \sigma_d \chi^{\boldsymbol{k}}_{\kappa Rlm} &= (i)^m \frac{i}{\sqrt{2}}(\sigma_1 - \sigma_2)\chi^{\boldsymbol{k}}_{\kappa Rl-m}\end{aligned} \tag{B.9}$$

where $\sigma_1, \sigma_2, \sigma_3$ are the Pauli matrices acting on the spin basis. The eigenvalues of these operators distinguish between the two possible irreducible representations, with $-i$ corresponding to Σ_3/Δ_3, and $+i$ to Σ_4/Δ_4.

Special care must be taken when computing the eigenvalues for the σ_d mirror symmetry,

C_{4v}	E	C_2	$2C_4(z)$	$2\sigma_v$	$2\sigma_d$	$\bar{E}$	$\bar{E} \otimes C_4(z)$
$\Gamma_1/\Lambda_1(A_1)$	1	1	1	1	1	1	1
$\Gamma_2/\Lambda_2(B_1)$	1	1	-1	1	-1	1	-1
$\Gamma_3/\Lambda_3(B_2)$	1	1	-1	-1	1	1	-1
$\Gamma_4/\Lambda_4(A_2)$	1	1	1	-1	-1	1	1
$\Gamma_5/\Lambda_5(E)$	2	-2	0	0	0	2	0
Γ_6/Λ_6	2	0	$-\sqrt{2}$	0	0	-2	$\sqrt{2}$
Γ_7/Λ_7	2	0	$\sqrt{2}$	0	0	-2	$-\sqrt{2}$

C_S	E	σ	$\bar{E}$	$\bar{E} \otimes \sigma$
$\Sigma_1/\Delta_1(A')$	1	1	1	1
$\Sigma_2/\Delta_2(A'')$	1	-1	1	-1
Σ_3/Δ_3	1	-i	-1	i
Σ_4/Δ_4	1	i	-1	-i

since it interchanges the $X(2)$ and $X(3)$ atoms within the $CeTX_3$ structure, located at $(0, \frac{1}{2}, z)$ and $(\frac{1}{2}, 0, z)$ respectively. Therefore the basis states centered around these atoms must be switched as well.

Figures B.6 and B.7 below show the nodal lines for $CeCoGe_3$ in the LDA and LDA+G regimes. In both cases, the nodal lines within the σ_v $(Z - \Gamma - \Sigma)$ and σ_d $(Z - \Gamma - X)$ planes are shown in the top plot, and the remaining plots show the bands along the k_z slices indicated in the figure. These representative band plots demonstrate that each nodal line in fact arises from the intersection of bands belonging to different irreducible representations, and are therefore protected by mirror symmetry and robust against perturbations.

Besides the nodal lines, some other interesting features can be seen in the plots. Firstly, the central axis in the band plots corresponds to points along the $\Gamma - Z$ axis. The two pairs of bands are therefore Kramers degenerate at these points, and must belong to either the Λ_6 or Λ_7 irreducible representation. In both LDA and LDA+G, Λ_7 starts below Λ_6 at the Γ point, and the order is switched at Z due to the Dirac point along the $\Gamma - Z$ axis. While

Compatibility Relations
$\Gamma_6(2) \rightarrow \Delta_3(1) \oplus \Delta_4(1)$
$\Gamma_7(2) \rightarrow \Delta_3(1) \oplus \Delta_4(1)$
$\Gamma_6(2) \rightarrow \Sigma_3(1) \oplus \Sigma_4(1)$
$\Gamma_7(2) \rightarrow \Sigma_3(1) \oplus \Sigma_4(1)$
$\Gamma_6(2) \rightarrow \Lambda_6(2)$
$\Gamma_7(2) \rightarrow \Lambda_7(2)$

Table B.2: Compatibility relations between Γ and points along the $\Delta(u, u, 0)$, $\Sigma(u, 0, 0)$, and $\Lambda(0, 0, u)$ high symmetry lines. The subscript denotes the irreducible representation in the respective point group, and the number in parentheses-the dimension of the irreducible representation.

away from the $\Gamma - Z$ both irreducible representations split into $\Sigma_3 \oplus \Sigma_4$ (or $\Delta_3 \oplus \Delta_4$), they can in fact be distinguished by the parity at the Γ point: for Λ_7 the two irreducible representations cross at the $\Gamma - Z$ axis, while for Λ_6 they touch without crossing.

Second, the plots at $k_z = 0.4712\pi/c$ for LDA, and $k_z = 0.9352\pi/c$ for LDA+G, highlight the band structure near cusp-like features in some of the nodal lines. These cusps appear to arise due to an accidental simultaneous crossing of three bands, as indicated by red circles in Figures B.6 and B.7 below. However, such a crossing would require the bands to belong to three different irreducible representations, and within the mirror planes, single electron bands can only belong to one of two possible irreducible representations: Σ_3/Δ_3 or Σ_4/Δ_4. Such a scenario is not ruled if multi-electron bands are considered. Careful inspection of the bands at these momentum points reveals that there is indeed a small energy gap between the bands, as expected.

B.3 Details of Topological Features in $CeCoGe_3$

For our choice of orbitals, the isoelectronic $CeTX_3$ compounds have 31 electrons, and the bands crossing the Fermi energy are numbered 29-32. These four bands have a number of topological degeneracies found by our monopole mining method. In the following discussion, we refer to each Weyl point and nodal line by the number of the lower band of the two forming the topological feature.

The full list of Weyl points formed by the lowest lying Γ_6 and Γ_7 doublets (bands 29-32) in LDA and LDA+G for the representative compound CeCoGe3 are shown below in Table B.3. For this compound we find seven (eight) non-equivalent Weyl points for the LDA (LDA+G) simulation.

There are two classes of Weyl points that are expected from the C_{4v} point group symmetry. The first is confined to the $k_z = 0$ ($k_z = 2\pi/c$) plane, and appears in sets of

Table B.3: The locations of non-equivalent Weyl points in the BZ of $CeCoGe_3$, given in units of $(2\pi/a, 2\pi/a, 2\pi/c)$. The Fermi energy is set to 0 eV. The band number (B) refers to the band forming the lower half of the Weyl cone, and C is the topological charge.

$CeCoGe_3$ LDA				
B	Location	C	#	E (meV)
29	(0.33860 , 0.39343 , 0.72781)	+1	16	-831.80
	(0.09700 , 0.18704 , 1.00000)	+1	8	-109.28
	(0.43351 , 0.22853 , 0.00000)	+1	8	-976.38
30	(0.11761 , 0.15192 , 0.55611)	-1	16	-140.22
	(0.16536 , 0.20827 , 0.71579)	+1	16	-105.69
31	-	-	-	-
32	(0.23461 , 0.27132 , 0.67584)	+1	16	+78.247
	(0.05697 , 0.28530 , 0.99636)	-1	16	+117.57

$CeCoGe_3$ LDA+G				
B	Location	C	#	E (meV)
29	(0.16695 , 0.11984 , 0.89380)	-1	16	-57.63
	(0.16138 , 0.13255 , 1.00000)	+1	8	-49.08
30	(0.13129 , 0.16831 , 0.58602)	-1	16	-110.14
31	(0.07098 , 0.17299 , 0.78441)	-1	16	+54.06
	(0.35171 , 0.19625 , 0.00000)	-1	8	+1.23
32	(0.17352 , 0.52586 , 0.00000)	+1	8	+26.92
	(0.16677 , 0.23615 , 0.52961)	+1	16	+32.71
	(0.08304 , 0.22061 , 0.61719)	-1	16	+36.76

eight. The effect of the σ_v and σ_d mirror planes is to flip the charge of the WPs, so that WPs located at $(k_x, k_y, 0)$, $(-k_x, -k_y, 0)$, $(k_y, -k_x, 0)$, and $(-k_y, k_x, 0)$ have the same charge, while those found at $(-k_x, k_y, 0)$, $(k_x, -k_y, 0)$, $(k_y, k_x, 0)$, and $(-k_y, -k_x, 0)$ have opposite charge. The second class of WPs comes in sets of 16, which respect the same symmetries about σ_v and σ_d, and are additionally separated in the k_z direction, with Weyls located at $(k_x, k_y, \pm k_z)$ having the same chirality.

Most of the Weyl points are strongly tilted Type-II, as they tend to occur at points in momentum space where the bands have strong Co-3d character, and are more strongly dispersing.

We identify a total of 15 nodal lines in the LDA case, labeled NL-A through NL-O, and

12 nodal lines in LDA+G, labeled NL-A through NL-L. The nodal lines and their charges are shown in Figure B.5. Just as with the WPs, we reference each NL by the lower band number of the pair of bands forming the NL.

We will now describe the nodal line features in $CeCoGe_3$ and how they are affected

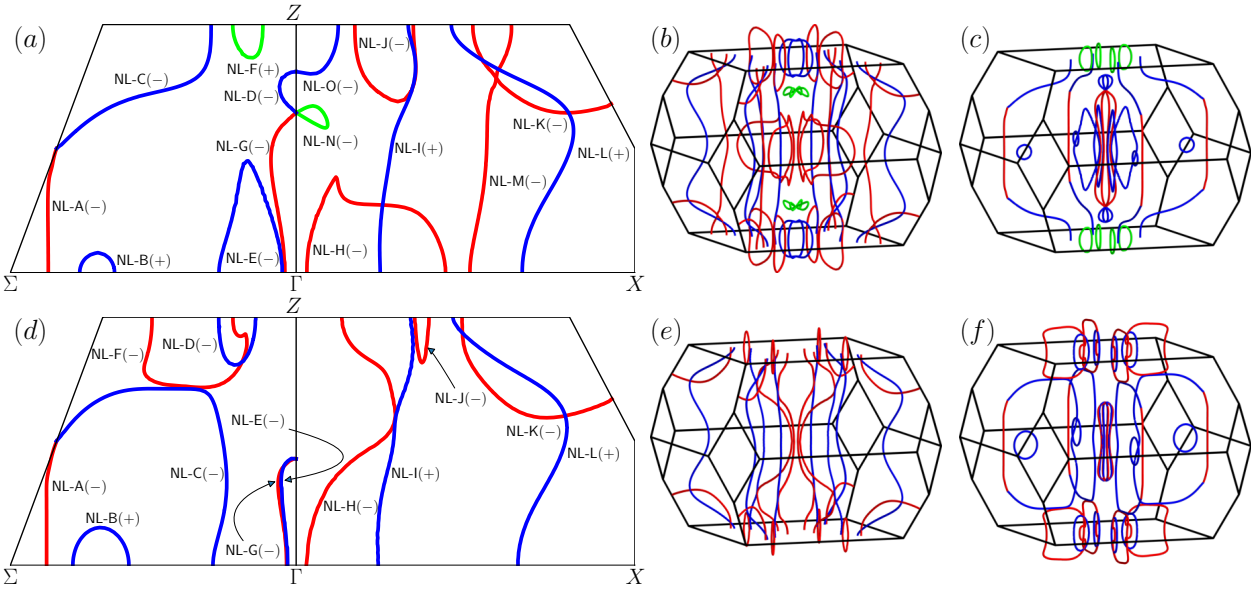

Figure B.5: Nodal lines in $CeCoGe_3$ from the touching of bands 29/30 (blue), bands 30/31 (green), and bands 31/32 (red), in the σ_v and σ_d mirror planes are plotted for LDA (a-c) and LDA+G (d-f). Labeled two dimensional projections of the nodal lines in LDA (a) and LDA+G (d) are provided for clarity, with the topological charge of each nodal line is indicated in parentheses. Three dimensional plots of LDA nodal lines A-G in the σ_v plane (b) and LDA nodal lines H-O in the σ_d plane (c). (e) shows the LDA+G nodal lines A-G in the σ_v plane while (f) shows the LDA+G nodal lines H-L in the σ_d plane.

by band renormalizations. In LDA, three nodal lines emerge from the Dirac point, labeled NL-D, NL-G, and NL-N. NL-D loops back within the $Z-\Gamma-\Sigma$ (σ_v) plane, reemerging in the $Z-\Gamma-X$ (σ_d) plane as NL-O, which connects with itself through the top surface of the BZ as shown in Fig B.5(b). NL-G instead curves downward, connecting with itself across the xy-plane.

The remaining NLs are either loops or extended lines spanning the entire BZ. The features lying close to the Fermi level are distorted dramatically by renormalization, while those that are lower in energy remain largely unchanged. Within the σ_v plane, three band 29

nodal lines, NL-C, NL-D, and NL-E, merge and permute their connections in LDA+G. For instance, NL-C in LDA+G, which connects across $\Gamma - \Sigma$ and loops around to exit the BZ around the N point, is created from a merging of NL-C and NL-E found in LDA. A similar merging of NLs takes place in the σ_d plane, where th NL-J loop merges with the left side of the NL-H loop in LDA to form NL-H in LDA+G which spans the entire BZ. The introduction of correlations completely destroys some features, such as NL-F of band 30 and NL-M, but also creates the new NL-F loop in band 31 in LDA+G. Despite having predominantly Ce-4f character and lying close to the Fermi energy, NL-A and NL-K are surprisingly robust to renormalization. The remaining features, including the NL-B loop, NL-I, and NL-L remain mostly unchanged as Ce correlations are turned on, since they are lower in energy and have predominantly Co-3d character.

NOTE: The NL letter labels used here are different from the numbered NL labels used in the Main Text. For clarity: NL-1 corresponds to NL-K, NL-2 to NL-G, NL-4 to NL-N, and NL-5 to NL-M. NL-3 corresponds to NL-D in LDA, and NL-E in LDA+G, which is a result of the shuffling of the connections between NL-C, NL-D, and NL-E.

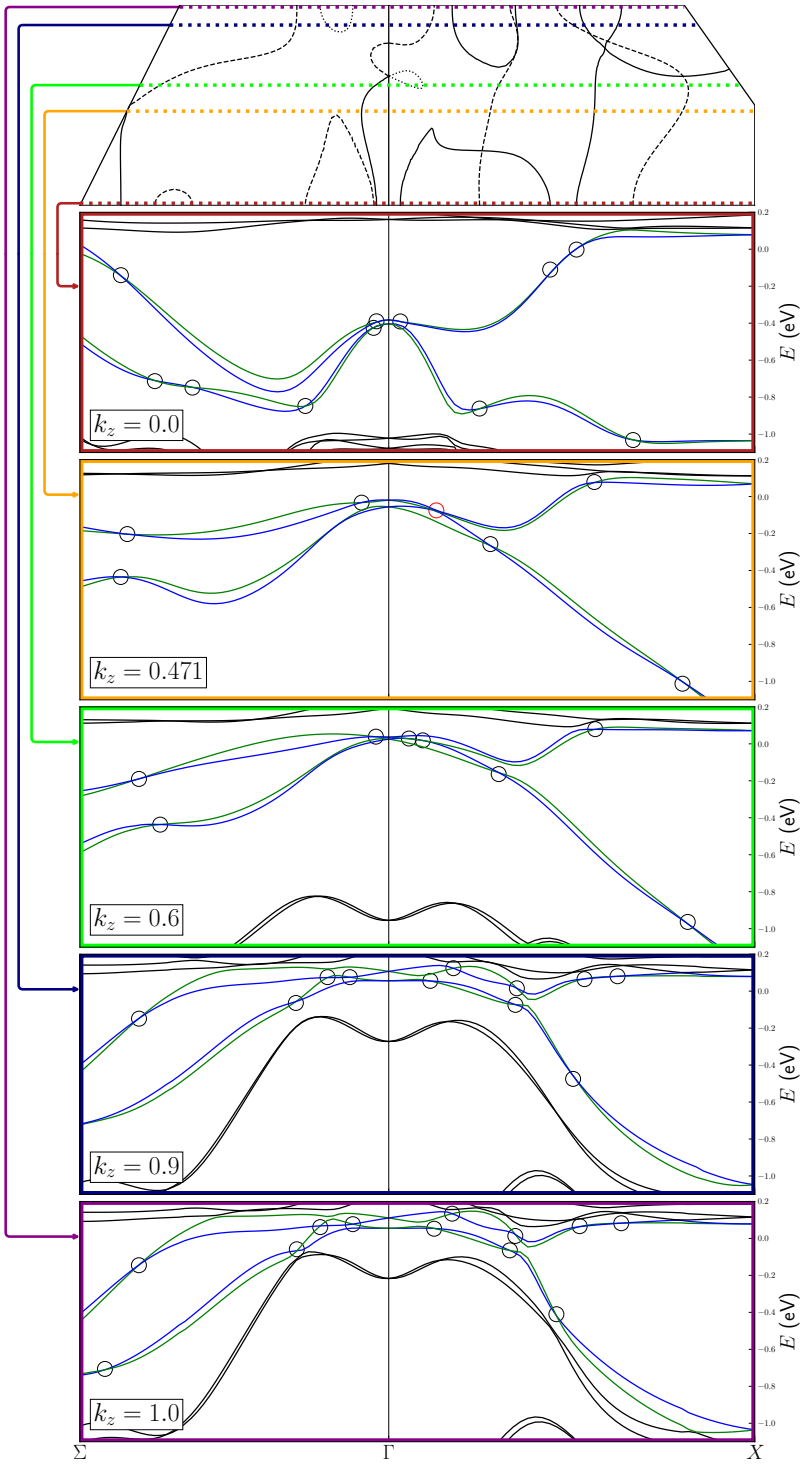

Figure B.6: Weyl nodal lines in LDA. Top plot shows the nodal lines for band 29 (dashed), band 30 (dotted), and band 31 (solid). Remaining plots show bands plotted for the various k_z slices indicated by dashed colored lines in the nodal line plot, with bands 29-32 highlighted. The color of each band denotes its irreducible representation: Σ_3/Δ_3 - blue and Σ_4/Δ_4 - green. Black circles indicate mirror symmetry protected nodal line crossings, and the red circle highlights a point where three bands approach closely but do not cross. k_z coordinates are given in units of $2\pi/c$.

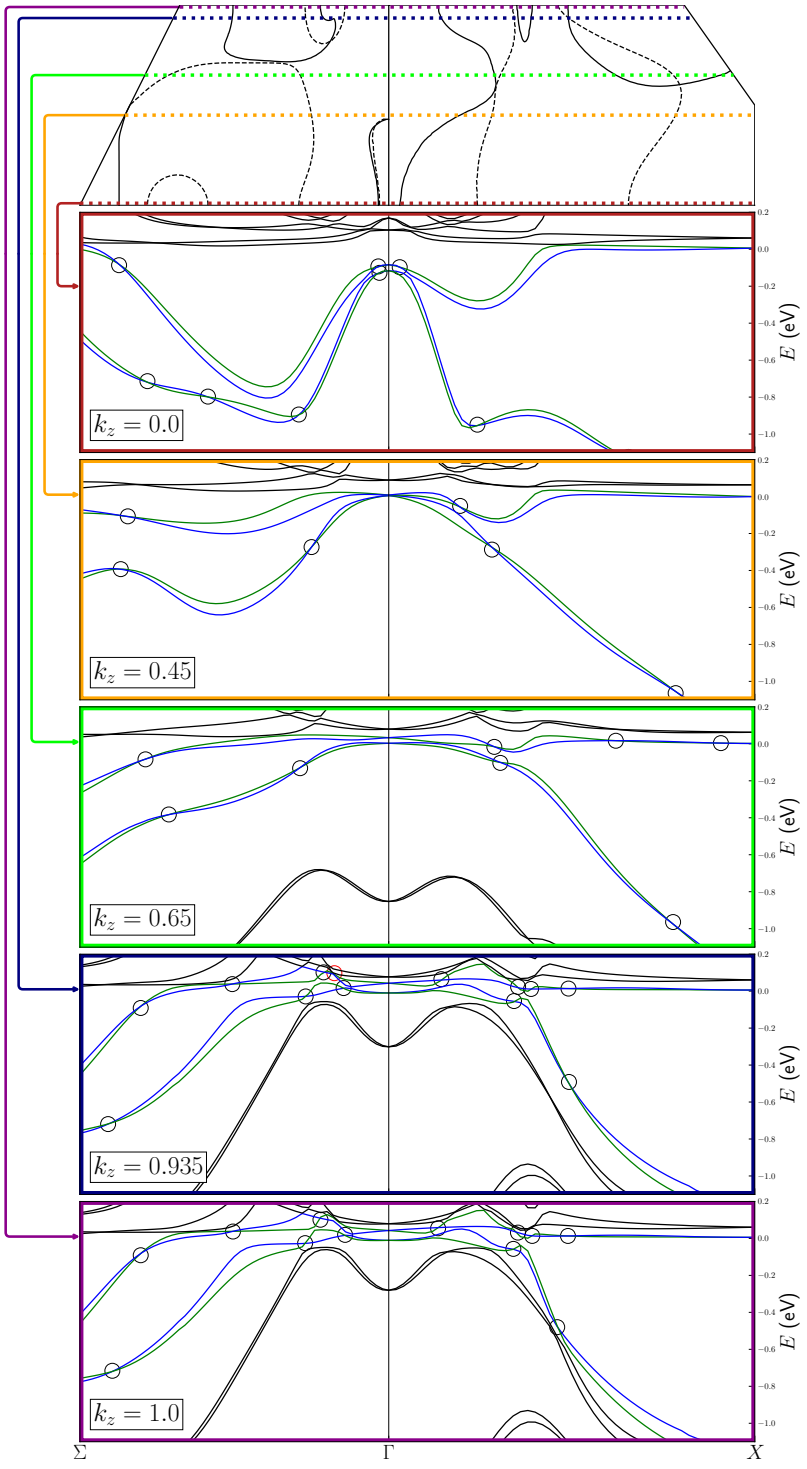

Figure B.7: Weyl nodal lines in LDA+G. Top plot shows the nodal lines for band 29 (dashed), and band 31 (solid). Remaining plots show bands plotted for the various k_z slices indicated by dashed colored lines in the nodal line plot, with bands 29-32 highlighted. The color of each band denotes its irreducible representation: Σ_3/Δ_3 - blue and Σ_4/Δ_4 - green. Black circles indicate mirror symmetry protected nodal line crossings, and the red circle highlights a point where three bands approach closely but do not cross. k_z coordinates are given in units of $2\pi/c$.

Appendix C

Details of LDA+DMFT calculation for UNiSn

Schematically, the LDA+DMFT method requires a self–consistent solution of the Dyson equation

$$[\omega 1 - H_0(\mathbf{k}) - \Sigma(\omega)]G(\mathbf{k},\omega) = 1 \tag{C.1}$$

for the one–electron Green function $G(\mathbf{k},\omega)$. The poles of its momentum integrated function $G_{loc}(\omega)$ contain information about the true local spectrum of excitations[67]. Here $H_0(\mathbf{k})$ is the effective single–particle Hamiltonian while $\Sigma(\omega)$ is a local self–energy operator. To improve the speed of the calculation we earlier proposed a representation of the self–energy in terms of the Laurent series [163]

$$\Sigma(\omega) = \Sigma(\infty) + \sum_i V_i^+(\omega - P_i)^{-1}V_i \tag{C.2}$$

where weights V_i^+, V_i and poles P_i are generally matrices. Such a form of the self–energy allows us to replace the non–linear (over energy) Dyson equation by a linear Schroedinger–like equation in extended subset of "pole states". This is clear due to a mathematical identity

$$\begin{pmatrix} \omega - H_0(\mathbf{k}) - \Sigma(\infty) & V^+ \\ V & \omega - P \end{pmatrix}^{-1} = \begin{pmatrix} [\omega - H_0(\mathbf{k}) - \Sigma(\infty) - V^+(\omega - P)^{-1}V]^{-1} & \dots \\ \vdots & \ddots \end{pmatrix} \tag{C.3}$$

which relates our original matrix inversion required to find $G(\mathbf{k}, \omega)$ (first element in the matrix from the right) to the matrix inversion in the extended "pole space".

For the problem of UNiSn, we first exactly diagonalize the interacting Hamiltonian for the atomic 5f electrons in the f^1, f^2 and f^3 configurations using the set of Slater integrals and the positions of the f levels described in the main text. Second, the f–electron self–energy is extracted via the calculation of the atomic 5f Green function describing the one–electron addition ($f^2 \rightarrow f^3$) and removal ($f^2 \rightarrow f^1$) processes to and from the Γ_3 f^2 ground state. Third, the expansion (C.2) for the self–energy is utilized and the poles of the Green function matrix, (C.3), are found by diagonalization. Fourth, the Fermi level is adjusted, the charge density is calculated and the entire procedure is made self–consistent. Finally, the poles of the self–consistent LDA+DMFT Green function, (C.3), are plotted in Figs. 3.9, 3.11, 3.12.

To study topological invariants, we take advantage of a recent proof [164] that utilizing a pole representation (C.2) makes the topological indices Z_2 of the interacting system [right part of (C.3)], and the non–interacting one, [left part of (C.3)], equivalent. The corresponding eigenstates of (C.3) behave as effective quasiparticles described by the Bloch waves $|\mathbf{k}j\rangle$ and can be used for Berry phase calculations as described in Chapter 3[35].